Retaining the square

Pb-to-Cd ion exchange in square PbSe superlattices

Master thesis

Utrecht University

Author: Jeroen de Boer
Date: May 18, 2020

Supervisor: Prof. dr. Daniël Vanmaekelbergh
Daily supervisor: Maaike van der Sluijs

Abstract

A novel class of two-dimensional semiconducting materials can be prepared by oriented attachment of colloidal nanocrystals (NCs). In the process of oriented attachment, a monolayer of NCs are epitaxially connected into ordered superstructures called "superlattices". Novel band structures that depend on the geometry and the chemical composition of the lattice are predicted for these superlattices. A rich electronic structure is predicted for the honeycomb zincblende CdSe superlattice in particular. However, the oriented attachment of NCs into superlattices has only been demonstrated for PbSe NCs and cation exchange is required to obtain superlattices of other chemical compositions. The Pb-to-Cd cation exchange reaction of PbSe superlattices has been reported in previous work. However, the CdSe crystal structure that is obtained after cation exchange and the exact mechanism of the exchange reaction remain unclear. Studying cation exchanged honeycomb superlattices is hindered by the buckled geometry of the silicene-type lattice. In the present work, cation exchange is investigated in square superlattices, as the NCs in superlattices with a square geometry only occupy one bonding plane. Nevertheless, for the square superlattices retention of large domain sizes after transformation into CdSe has not yet been reported. Here we show that nearly full retention of the square superlattice structure is achieved by reducing the cation exchange reaction temperature down to 100 °C. Moreover, we show that annealing of the superlattice before cation exchange negatively impacts retention of the long-range order of the superlattice. The cation exchanged square superlattices obtained by the optimized exchange methods can be used to further study the obtained CdSe crystal structure and the exchange reaction mechanism in superlattices.

Contents

1 Introduction

Colloidal semiconductor nanocrystals (NCs) have received much attention over the last decades due to their size and shape dependent electronic properties. Advances in the colloidal chemistry of NCs has made it possible to construct ordered, two-dimensional lattices consisting of NCs that are attached by atomic bonds[1]. These one NC monolayer thick "superlattices" have a bandstructure that depends on the geometry and chemical composition of the lattice[2, 3]. Tight-binding calculations have shown the presence of non-trivial flat bands, topological states and multiple Dirac-cones in the band structure of zincblende CdSe superlattices with a honeycomb nano-geometry[3]. In addition, high charge carrier mobilities were measured for square PbSe superlattices[4]. Hence, oriented attachment of NCs is an attractive method to construct a novel type of semiconducting material with possible applications in the field of topological insulators and opto-electronic devices.

These superlattices have so far only been fabricated from Pb chalcogenide NCs and cation exchange reactions are required to obtain superlattices of other chemical compositions[1, 5]. Previously, the presence of both zincblende and wurtzite CdSe was observed after Pb-to-Cd cation exchange of the honeycomb PbSe lattice[6]. Since this honeycomb superlattice has a buckled geometry[7], investigation of the different crystal structures in this lattice was difficult. Furthermore, not much is known about where the exchange reaction is initiated, *i.e.* if the Pb-to-Cd exchange is initiated at the necks, the NC cores or everywhere at once. Both the presence of different CdSe crystal structures and the place at which the exchange reaction is initiated could be investigated more easily in the square lattice, where the NCs occupy only one plane. The Pb-to-Cd cation exchange reaction of square PbSe superlattices with retention of the overall geometry has been reported in literature[1]. Nevertheless, these square CdSe superlattices showed an increase in the amount of defects and molten structures and a reduction in the square ordering in the lattice[1].

In the present work, different annealing procedures are performed on square PbSe superlattices in an attempt to increase the stability of the lattice during cation exchange. Subsequently, cation exchange is performed on as-prepared and annealed square PbSe superlattices. The cation exchange reaction is optimized to improve the retention of the square order and two optimized methods are described to prepare fully and partially Pb-to-Cd exchanged square superlattices. Next, we attempt to determine the crystal structure of the fully transformed square CdSe superlattice. Finally, we attempt elemental mapping of the partially exchanged lattice to gain insight into the location of onset of the exchange reaction in the square superlattices.

This work is organized as follows: first, the key concepts in this work are explained. The focus will be on the electronic properties of the NCs and the superlattices, the fabrication and annealing of the square superlattices and the Pb-to-Cd cation exchange reaction of these structures. Subsequently,

the experimental methods are explained. In the next chapter, the results of the experimental work is presented. This chapter is separated into two parts, where in the first part the production of the PbSe NCs and the square superlattices is described. In the second part, the results of the cation exchange reactions with different reaction conditions are presented. In the final chapter, the conclusions are summarized and an outlook is given.

2 Theory

In this chapter, theoretical background is given of the most important concepts in this work. First, the electronic properties of NCs and superlattices are outlined. This section is followed by several sections on the preparation of square superlattices. In these sections, first the synthesis and properties of PbSe NCs, the building blocks of the superlattices, are treated. In the next section, the self-assembly and oriented attachment of the NC building blocks into two-dimensional square superlattices is described. This section is followed by a section on annealing of the as-prepared superlattices to induce stronger electronic coupling. Finally, cation exchange of the PbSe superlattices with retention of the lattice geometry is explained.

2.1 Electronic properties of NCs and superlattices

Semiconductor nanocrystals are crystalline particles of a semiconducting material with dimensions of one up to several tens of nanometers. Owing to their small size, NCs have a size dependent band gap and well defined energy levels at the edge of the energy bands[8]. These properties make NCs interesting, tunable building blocks for the superlattices that are considered in this work. This section explains the origin of these electronic properties. To this end, the effect of quantum confinement on the Bloch wave of an electron in a crystal is described. Next, the resulting change of the electronic structure of the NC is explained. Finally, the electronic properties of two-dimensional superlattices that can be constructed from the NC building blocks are briefly outlined.

According to Bloch's theorem, the wavefunction of an electron in a bulk crystal can be expressed as a Bloch wave of the form[8–10]:

$$\psi_{Bloch}(\mathbf{r}) = e^{i\mathbf{kr}} u_{\mathbf{k}}(\mathbf{r}) \tag{2.1}$$

where $\mathbf{k}$ is the wave vector, with $|\mathbf{k}| = \frac{2\pi}{\lambda}$ where λ is the wavelength of the electron, $\mathbf{r}$ is the position of the electron and $u_{\mathbf{k}}(\mathbf{r})$ is a periodic function with the periodicity of the crystal lattice. As the size of the NCs decreases below that of twice the exciton Bohr radius, charge carriers and excitons in the NCs become confined. This exciton Bohr radius is the most probable distance between the electron and hole in an exciton and can be expressed as[8]:

$$r_B = \frac{\hbar^2 \epsilon}{e^2} \left(\frac{1}{m_e^*} + \frac{1}{m_h^*} \right) \tag{2.2}$$

with $\hbar$ the reduced Planck constant, ϵ the dielectric constant of the NC material, e the electron charge and m_e and m_h the effective masses of the electron and the hole, respectively. Hence, the exciton Bohr radius depends on the dielectric constant and the effective masses of the electrons and holes in the NC material. Consequently, the NC diameter at which charge carriers in the NCs experience quantum confinement depends on the chemical composition of the NC. For PbSe and CdSe, which are considered in this work, the exciton Bohr radius corresponds to 46 and 4.9 nm, respectively[8]. Therefore, as the NC diameter decreases to values below 92 or 9.8 nm for PbSe or CdSe, respectively, the charge carriers and excitons in the NCs become quantum confined. As a result, the Bloch wave functions of the charge carriers in the bulk material are modulated by an envelope function[8]:

$$\Psi(\mathbf{r}) = \psi_{Bloch}(\mathbf{r}) * \phi_{env}(\mathbf{r}) \tag{2.3}$$

By approximating the shape of the NC as perfectly spherical, the envelope function can be expressed as the product of spherical harmonics ($Y_l^m(\theta, \phi)$) and a radial Bessel function (R(r))[8]:

$$\phi_{env}(\mathbf{r}) = Y_l^m(\theta, \phi)R(r) \tag{2.4}$$

The confinement energy can be found by solving the Schrödinger equation for this envelope function, which yields the discrete energy levels of the confined charge carrier[8]:

$$E_{n,l}^{conf}(D) = \frac{2\hbar^2\chi_{n,l}^2}{m^*D^2} \tag{2.5}$$

where $\chi_{n,l}$ are the roots of the Bessel function, which depend on the quantum numbers n and l[11], m^* is the effective mass of the hole or the electron and where D is the diameter of the spherical NC. Beside the fundamental band gap of the semi-conductor material of the NC (E_{gap}), this confinement energy must also be overcome for an electron to be excited from the valence to the conduction band. For NCs in the strong confinement regime, *i.e.* for NCs with a diameter below the Bohr exciton radius, the total band gap of the NC becomes[8]:

$$E_{gap}^{total}(D) = E_{gap} + E_{n,l}^{conf}(D) = E_{gap} + \frac{2\hbar^2\chi_{n,l}^2}{m_e^*D^2} + \frac{2\hbar^2\chi_{n,l}^2}{m_h^*D^2} \tag{2.6}$$

Since the confinement energy is inversely proportional to the diameter of the NC squared, it follows that the band gap of a quantum confined NC increases as the diameter of the NC decreases.

The envelope function $\phi_{env}(\mathbf{r})$ shows a strong resemblance to the hydrogen wavefunction[11]. Consequently, the wavefunctions of the lowest lying energy states show the same symmetries as those of the hydrogen orbitals[8]. These atomic-like electronic states have also been demonstrated experimentally[12]. Due to these atomic-like states, spherical, quantum confined NCs are also referred to as 'artificial atoms'.

Analogous to atoms, artificial diatomic molecules can be constructed with NCs as well[13, 14]. These structures show hybridization of the NC wavefunctions, with the formation of bonding and anti-bonding states, similar to those formed in the hydrogen molecule[13, 14]. Apart from these diatomic molecules, large one or two-dimensional crystals made of colloidal lead chalcogenide NCs can be fabricated as well[1, 5, 15]. In these crystals, the NCs are attached by atomic bonds between specific facets of the NCs, causing strong electronic coupling between the individual NCs[1, 2]. For these two-dimensional so-called superstructures or superlattices, both a square and a honeycomb geometry have been reported[1]. In a course approximation, the individual NCs in these superlattices can be seen as artificial atoms in an atomic lattice[2, 16]. Hence, these superlattices show electronic properties which depend not only on the chemical composition of the NCs, but also on the geometry of the superlattice[2, 3]. Calculations of the electronic structure of the square superlattices have predicted that these superlattices show a dimensionality below two, with band-like transport of electrons and holes[2]. In addition, the zincblende CdSe honeycomb superlattice is predicted to exhibit multiple Dirac cones, non-trivial flat bands, and topological insulating gaps[3]. Hence, these superlattices show very interesting electronic properties, making them a promising class of semiconductor nanostructures.

The following sections will discuss how these two-dimensional superlattices with different chemical compositions are prepared. To start, the synthesis and geometry of PbSe NCs, which are most commonly used to produce two-dimensional superlattices[1, 7, 15, 17–19], is outlined in the next section.

2.2 Colloidal PbSe NCs

In this work, colloidal PbSe NCs are used as the building blocks of the superlattices. This section outlines the commonly used procedure to synthesize these NCs. Subsequently, the most important geometric properties of these NCs for the preparation of the superlattices are reviewed.

Colloidal PbSe NCs are typically synthesized by introducing a source of selenium into a preheated lead oleate solution[20–22]. The proposed mechanism behind this synthesis is the decomposition of the selenium and lead precursors to form PbSe monomers, stabilized by ligands in the reaction mixture[20, 21, 23]. Due to the rapid combination of the precursors, these monomers form a supersaturation in the solution from which NCs nucleate and grow[20, 21]. The PbSe NCs that are synthesized in this way are capped and stabilized by oleate ligands from the original lead oleate precursor[20, 24, 25].

A three-dimensional model of the oleate ligand stabilized PbSe NC with its different facets is shown in Figure 2.1a. In this model, the ligands have been omitted for clarity. PbSe has a rock-salt crystal structure. Therefore, the {100} facet of the PbSe NC, shown in Figure 2.1b, is the most stable, as the Pb and Se atoms are square packed on this facet[25, 26]. Apart from the {100} facet, the NCs also contain a {110} facet, in which the Pb and Se atoms form lines, as shown in Figure 2.1c. In the absence of any ligands, this facet shows a theoretical surface energy 73% higher than the {100} facet[26]. This increase in the surface energy is even more pronounced in the polar {111} facet, shown in Figure 2.1d,

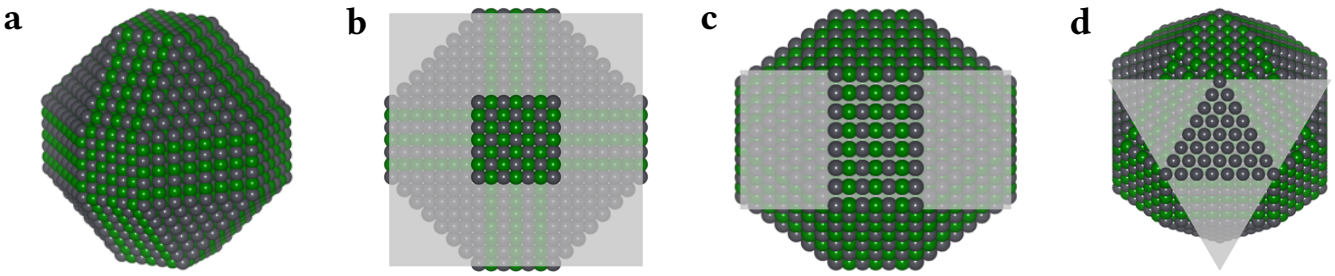

Figure 2.1: (a) Three quarter view of a PbSe NC, with Pb in black and Se in green and with the ligands omitted for clarity. The NC shows different facets due to stabilization of less stable facets by the ligands, with **(b)** the {100} facet of the NC, which is the most stable, **(c)** the {110} facet of the NC and **(d)** the least stable Pb terminated {111} facet.

which consists of exclusively Pb or Se atoms. This facet has a theoretical surface energy 78% higher than the {100} facet[26]. As a result, the ligand-free PbSe NCs would show a cubic structure. However, in the dispersion the {110} and {111} facets are stabilized by the oleate ligands, so that the truncated cuboctahedral shape of the NCs shown in Figure 2.1a is obtained[25, 26]. The extent of this stabilization of the {110} and {111} facets can be tuned by varying the ligand density on the surface of the NCs[25, 26]. Hence, apart from stabilizing the PbSe NCs in the dispersion, the oleate ligands on the PbSe NC surfaces also play an important role in determining the shape of the NCs[25].

The shape and the capping of the PbSe NCs with the oleate ligands are of importance for the fabrication of the superlattices, as will be explained in the upcoming section. In this next section, the preparation of the square superlattices through the processes of self-assembly and subsequent oriented attachment of the NCs are reviewed.

2.3 Two-dimensional square superlattices

As was mentioned in Section 2.1, the colloidal PbSe NCs reviewed in the previous section can form two-dimensional superlattices with different geometries[1]. These superlattices form through self-assembly and subsequent oriented attachment of the PbSe NC building blocks[17]. This way, covalent bonds form between the NCs, as a result of which the NCs are coupled electronically. This electronic coupling gives rise to the interesting electronic properties of these nanostructures discussed in Section 2.1[2, 3]. The mechanisms behind the self-assembly and oriented attachment of the PbSe NCs are explained in this section. Here, the focus will be on the square lattices that are studied in this work.

In the dispersion, the colloidal stability of the NCs is ensured by the oleate capping ligands. Two repulsive interactions are behind the stabilisation of the NCs. One of these interactions is the formation of an osmotic pressure if ligand shells of different NCs start to overlap. Since solvent is excluded in this overlapping region, an osmotic pressure is formed that drives the NCs apart[27]. The second repulsive

NC-NC interaction is the elastic repulsion of the hydrocarbon chains of the ligands. This repulsive interaction arises as the distance between the NCs decreases to below twice the width of the ligand shells[28]. Together, these two interactions prevent the aggregation of the NCs in the dispersion.

Two-dimensional square PbSe superlattices are typically produced from this stable dispersion by dropcasting of the dispersion on an ethylene glycol liquid substrate[1]. The NCs are immiscible with the polar ethylene glycol substrate on account of the long aliphatic chains of the oleate ligands of the NCs. As a result, the NCs adsorb to the two-dimensional liquid/gas interface as the toluene evaporates, leading to the confinement of the NCs at this two-dimensional interface[17]. A schematic representation of this adsorption of the NCs is given in Figure 2.2a. By using a small volume of a dilute NC dispersion, only enough NCs are present to form a monolayer of NCs at this interface.

The next step of the square lattice formation process commences after further evaporation of the toluene solvent. As the solvent evaporates, the osmotic stabilization of the NC dispersion is reduced while the concentration of NCs is increased. This causes gentle destabilization of the dispersion. Due to this gentle destabilization of the dispersion, the PbSe NCs form ordered structures predominantly due to entropic factors, but also on account of van der Waals attractions[29–31]. This formation of an ordered structure by entropic factors can seem counter-intuitive. However, this is explained by the maximization of the free volume of each NC by forming an ordered rather than a jammed structure. Therefore, the loss of entropy due to the ordering of NCs is opposed by the increase in translational and rotational entropy of the NCs in the ordered structure[32]. This process in which the individual NCs organize themselves into an ordered structure is called "self-assembly". In the case of the PbSe NCs, where entropy maximization is the most dominant cause of the ordering of NCs[29], a structure is formed that allows the most dense packing of NCs[31]. Hence, in the case of the NCs confined at the liquid/gas interface, a hexagonal monolayer is formed[17, 31]. In this hexagonal monolayer, the NCs have bond angles of 60°, as shown in Figure 2.2b[17].

After this self-assembly process of the NCs, presumably oleate ligands are stripped off the {100} facets[17, 33]. This causes the alignment of a <100> direction in each of the NCs perpendicular to the liquid/gas interface[17]. At the same time, the presumed reduction of ligands on the {100} facets of the NCs causes electrostatic and van der Waals attractions between the neighbouring {100} facets of the NCs[17]. As a result of this attraction, the distances between the NCs decreases while the hexagonal ordering is distorted into a pseudo-hexagonal structure with bond angles of 55°/70°[17]. This distorted, pseudo-hexagonal structure is depicted schematically in Figure 2.2c.

In the final step of the formation of the square superlattice, oriented attachment takes place between the ligand stripped {100} facets of the NCs[1, 7, 33, 34]. This process was shown to occur as the NC-NC distances become small, which results in significant deformation of the NCs. This deformation was attributed to dipole-dipole interactions between the NCs enabled by the oleate ligand removal[33, 34]. Finally, epitaxial connections, called 'necks', are formed between the {100} facets of neighbouring NCs on account of this deformation[17, 33, 34]. As shown in Figure 2.2d, this final step results in the formation of the square superlattice with NCs linked together by necks at bond angles of 90°. Compared

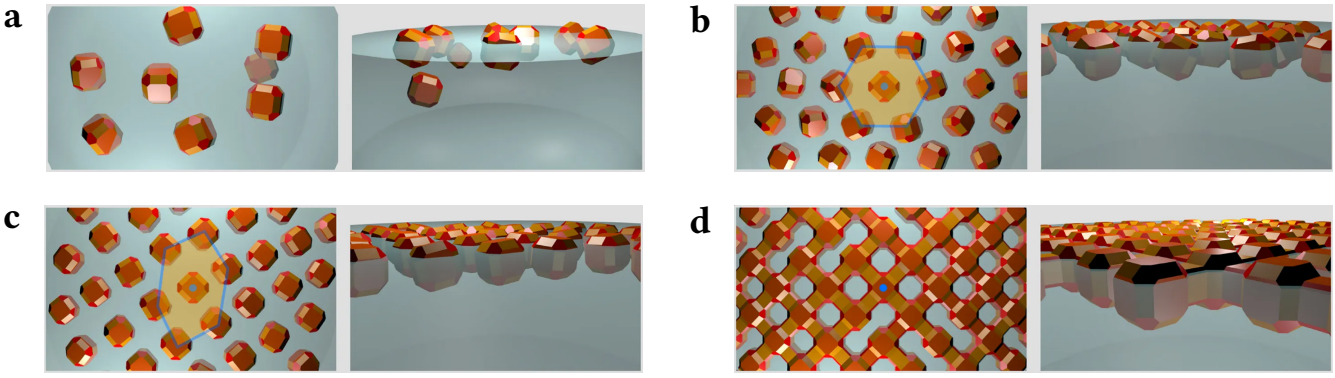

Figure 2.2: Schematic representation of the self-assembly and subsequent oriented attachment of PbSe NCs into a two-dimensional square superlattice. **(a)** After dropcasting of the PbSe NC dispersion, the NCs adsorb to the liquid/gas interface. **(b)** As the NC dispersion is destabilized due to the evaporation of the toluene solvent, the NCs self-assemble in a hexagonal monolayer. **(c)** Attractions between the {100} facets of neighbouring NCs causes a distortion of the hexagonal lattice to a pseudo-hexagonal ordering. In addition, these attractions cause the distances between the NCs to decrease. **(d)** Finally, electrostatic attractions between the {100} facets causes the formation of epitaxial connections, called 'necks'. Figure adapted from [17].

to the NCs in a dispersion, this as-prepared square superlattice shows a red-shift and broadening of the first exciton peak in the absorption spectrum[4, 18, 35]. These effects are caused by polarization of the dielectric environment of the NCs[36] and electronic coupling between the NCs[37]. After the formation of the two-dimensional square superlattice, the lattice can be scooped or stamped on a solid substrate. This way, the square superlattices can be characterized by *e.g.* absorption spectroscopy, electron microscopy or scanning tunneling microscopy[1, 7, 18, 35]. Moreover, post-synthetic treatments such as cation exchange can be performed on the superlattice transferred to a solid substrate[1, 7].

It should be noted that another, slightly different method exists to produce the square superlattices. In this method, a base, *i.e.* aniline, is added to a self-assembled PbSe NC monolayer at the liquid/gas interface[15, 35]. The addition of this base causes more aggressive stripping of the oleate ligands from the {100} facets, inducing neck formation at an earlier stage[15]. Nevertheless, the square superlattices produced with this method show smaller domain sizes and more defects compared to square lattices produced by the previously outlined procedure[1, 15, 17, 18]. Therefore, this method of adding a base to the self-assembled NC monolayer was not employed in this work.

After the formation of the two-dimensional square superlattices as outlined in this section, the thickness of the necks can be increased by annealing of the as-prepared superlattices. In the next section the different methods to anneal square superlattices and the effect of annealing on the lattice are described.

2.4 Annealing of superlattices

Annealing of the as-prepared square superlattices is commonly performed to increase the thickness of the necks between the NC cores in the superlattice[4, 18, 35]. The different annealing methods that have been reported in literature and the implications of the increased neck thickness are described in this section.

Gentle annealing of the square superlattice is usually performed by heating of the ethylene glycol substrate to up to 80 °C at the end of the superlattice preparation outlined in the previous section[1, 4, 18]. By varying the duration and the temperature at which the annealing is performed, the neck thickness can be increased to the point that the neck thickness approaches the NC core diameter[4].

Apart from the annealing of the square lattice on the ethylene glycol substrate, Walravens *et al.* presented an alternative approach to the annealing of the square superlattice[35]. In their work, superlattices were transferred to a TEM grid or quartz glass after preparation, after which the lattices were annealed in a nitrogen filled oven[35]. In the work by Walravens *et al.*, only the relative neck thickness was reported, which is calculated by normalizing the neck thickness to the NC diameter in the lattice. The authors demonstrated that the relative neck thickness increased from 0.58 ± 0.04 up to 0.70 ± 0.02 by annealing at temperatures of 75 - 150 °C for 1 hour[35]. Apart from increasing the relative neck thickness, annealing of square superlattices was shown to reduce the amount of edge dislocations and point defects in the necks between the NCs as well[35]. An important note is that in the experiments of Walravens *et al.* the alternative approach of superlattice preparation was used, in which aniline was added to a self-assembled monolayer of PbSe NCs to induce epitaxial growth of necks[15, 35]. Hence, it is possible that the superlattices produced in this way show different behaviour during annealing, *e.g.* due to a difference in ligand density on the superlattice surface.

As a result of the reduced number of defects in the neck and the increase in the neck thickness, annealed square superlattices show a larger red-shift and increased broadening of the first exciton peak compared to as-prepared square superlattices[4, 35]. In addition, annealed superlattices show an enhanced charge carrier mobility, which is ultimately limited by the lack of long-range order in the lattice[4, 18, 35]. Hence, the electronic coupling between NCs in a square superlattice can be increased by annealing. This is important since strong coupling is required to realize the promising electronic properties of these structures[2].

The outlined preparation and annealing of square superlattices has so far only been demonstrated for PbSe, PbS and PbTe superlattices[1, 5, 15]. Consequently, cation exchange of the square PbSe superlattices is required to produce two-dimensional square superlattices of other semiconducting compounds[1, 7]. In the next section this cation exchange of the square PbSe superlattices is explained in further detail.

2.5 Cation exchange of PbSe superlattices

As mentioned in Section 2.1, the band structure of superlattices of epitaxially connected NCs depends on both the geometry and the chemical composition of the lattice[2, 3]. Hence, control over the chemical composition is required to tune the electronic properties of the superlattices. In previous research, oriented attachment of CdSe NCs into dimers[38] or quantum wires[39] or of ZnS NCs into rods[40] has been demonstrated. However, so far no epitaxially connected superlattices have been constructed with NCs other than PbS, PbSe and PbTe[1, 5]. The prepared PbS, PbSe or PbTe superlattices must therefore be cation exchanged to prepare superlattices of other semiconductor compounds[1, 7]. In this section cation exchange is explained briefly, after which the methods by which cation exchange is performed on superlattices is reviewed.

Contrary to bulk materials[41, 42], cation exchange reactions typically occur rapidly for NCs. This discrepancy is most likely due to the high surface-to-volume ration and the lower activation barrier for ion diffusion of NCs[42, 43]. During the cation exchange reaction, the anion lattice is preserved, so that the shape of the original NC is largely retained[43, 44]. Hence, cation exchange of nanomaterials is a versatile method for the preparation of nanostructures that cannot be synthesized directly[43, 45, 46].

For PbSe superlattices, both Pb-to-Cd and Pb-to-Cu cation exchange with retention of the superlattice geometry have been demonstrated[1, 7]. The cubic zincblende crystal structure was obtained after transformation of a PbSe superlattice into CdSe[1, 7, 26, 44]. The Pb-to-Cd cation exchange reaction of PbSe superlattices is therefore a suitable method to obtain honeycomb zincblende CdSe superlattices with the rich electronic structure outlined in Section 2.1. Schematic representations of the unit cells of the rock-salt PbSe and the zincblende CdSe crystal structures are shown in Figure 2.3. The driving force behind this exchange reaction are the lower lattice energy of CdSe[26], and the low lattice mismatch

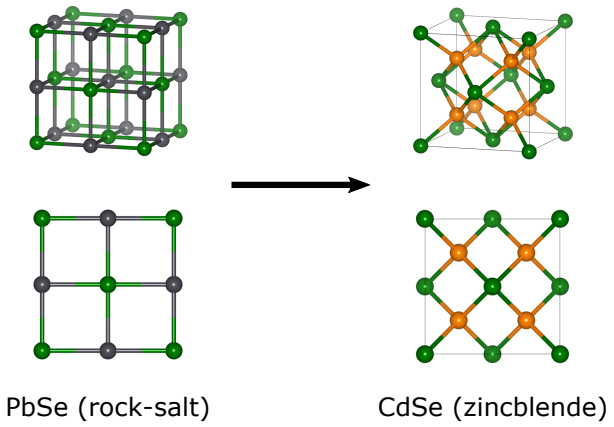

Figure 2.3: Unit cells of the initial rock-salt PbSe structure and the zincblende CdSe formed after cation exchange, with Se in green, Pb in black and Cd in orange. In this exchange reaction, the anion sublattice is preserved.

between rock-salt PbSe and zincblende CdSe of less than 2%[47, 48]. The CdSe superlattices are typically prepared by heating of the PbSe nanostructure to 100 - 175 °C in an excess of Cd(oleate)$_2$[1, 7, 44]. This temperature range is relatively high temperatures compared to other cation exchange reactions[7, 26, 43, 44].

Beside the typically obtained zincblende CdSe, a mixture of the zincblende and wurtzite CdSe crystal structure has also been observed after cation exchange of a honeycomb PbSe superlattice[18]. This wurtzite crystal structure is shown schematically in Figure 2.4. As can be inferred from this figure, the exchange reaction from the cubic rock-salt PbSe to the hexagonal wurtzite CdSe requires a slip of the anion lattice. As a result, the energy barrier for the formation of this crystal structure is higher than for the exchange into the zincblende structure[48]. Hence, the formation of both zincblende and wurtzite CdSe is surprising. Unfortunately, investigation of the different crystal structure domains was hindered by the buckled geometry of the honeycomb lattice[7]. As shown schematically in Figure 2.2, the NCs in the square superlattice only occupy one bonding plane. Investigation of the presence of the zincblende and wurtzite crystal structures in this superlattice would therefore prove less difficult. Consequently, this was one of the aims of the present work.

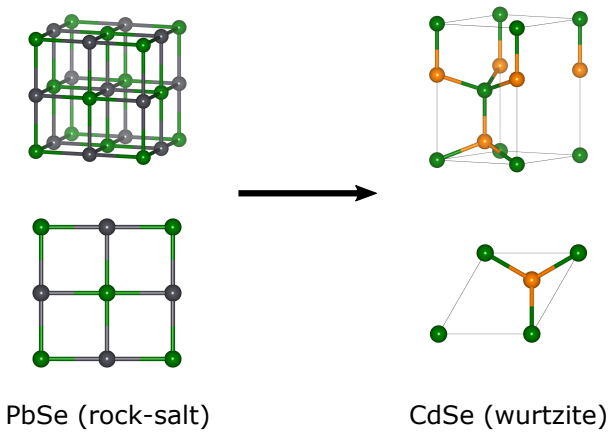

Figure 2.4: Unit cells of the initial rock-salt PbSe and the wurtzite CdSe which also forms during cation exchange[6], with Se in green, Pb in black and Cd in orange. In this exchange reaction, the anion sublattice is distorted.

3 Materials and Methods

3.1 Chemicals

Methanol, 1-butanol, toluene and ethylene glycol (EG) were purchased from Sigma-Aldrich (all anhydrous, 99.8%). Selenium (-200 mesh, 99.999% trace metals basis) was obtained from Alfa Aesar. Trioctylphosphine (TOP, 90%), diphenylphosphine (DPP, 98%), oleic acid (OA, 90%), 1-octadecene (ODE, 90%) and tetrachloroethylene (TCE, anhydrous $\geq$ 99%) were obtained from Sigma-Aldrich. Lead(II) acetate trihydrate ($Pb(Ac)_2 \cdot 3H_2O$, 99.999%) and cadmium acetate dihydrate ($Cd(Ac)_2 \cdot 2H_2O$, $\geq$ 98%) were both purchased from Sigma-Aldrich. All chemicals were used without further purification.

3.2 PbSe NCs

3.2.1 PbSe NC synthesis

PbSe nanocrystals were synthesized based on a methodology adapted from Steckel et al.[21]. First, a selenium precursor was prepared inside a glovebox. To this end, a mixture of 3.536 g selenium (44.9 mmol), 46.5 mL TOP (104 mmol) and 0.41 mL DPP(2.36 mmol) was stirred at a temperature of 72 °C for 75 minutes. The clear, colourless mixture with black specks was subsequently heated to 80 °C for 2 hours. Since black specks were still visible, the mixture was stirred overnight without heating to obtain a clear, colourless mixture.

To prepare the Pb precursor, a mixture of 4.777 g $Pb(Ac)_2 \cdot 3H_2O$ (12.59 mmol), 11.9 g OA and 50.5 mL ODE was stirred vigorously under vacuum ($2.9*10^{-2}$ bar) at 50 °C for 1 hour. The white, turbid mixture was then heated to 120 °C for 2 hours to obtain a clear, colorless liquid.

To prepare the PbSe NCs, a mixture of 10.25 mL Pb precursor and 0.5 mL OA was heated to 180 °C inside a glovebox, after which 7.5 mL of the Se precursor was rapidly injected. The temperature of the black mixture was kept at approximately 150 °C for 3 minutes. Subsequently, the reaction was quenched by the swift injection of 10 mL 1-butanol. An additional 10 mL methanol was injected after the reaction mixture reached a temperature of 55 °C. After centrifuging the mixture at 2750 rpm for 10 minutes, the black precipitate was redispersed in 10 mL toluene. The black mixture was washed twice by adding 10 mL 1-butanol and 5 mL methanol, centrifuging at 2750 rpm for 10 minutes and redispersion of the black precipitate in 10 mL toluene. After centrifugation in the second washing step, the reaction product did not fully precipitate and an extra 4 mL methanol was added to the dark liquid. Next, the centrifugation

step was repeated to fully precipitate the mixture. Finally the black precipitate was redispersed in 10 mL toluene.

3.2.2 Absorption measurements of PbSe NCs

UV-Vis absorption spectra of the NC dispersion were recorded on a Perkin-Elmer LAMBDA 950 UV/Vis/NIR spectrophotometer. Samples for the absorption measurements were prepared by drying 40 µL of the NC dispersion under vacuum, after which the black precipitate was redispersed in 3 mL TCE. The absorption measurements were performed between 800-2500 nm.

Fourier-transform infrared absorption measurements were performed on a Brucker Vertex 70 spectrometer. Samples for the absorption measurement were prepared by drying 400 µL of the NC dispersion under vacuum, after which the black precipitate was redispersed in 400 µL TCE. The black mixture was transferred to a liquid cell with two KBr windows for the measurements. The measurements were performed between 400-7500 cm^{-1} with a resolution of 1 cm^{-1}, averaging over 60 scans.

3.3 Preparation of square PbSe superlattices

3.3.1 Oriented attachment of PbSe nanocrystals

A batch of ∼200 mL EG was degassed under vacuum (10^{-2} bar) and vigorous stirring at a temperature of 75 °C for 4 hours.

Square PbSe superlattices were prepared inside a nitrogen-filled glovebox (< 0.1 ppm O_2) free of amines or alcohols. For the preparation of the lattices, typically 350 µL of a diluted PbSe nanocrystal dispersion ($4.4 * 10^{-7}$ M) was dropcast on a Petri dish (⌀ 27 mm) filled entirely with degassed EG (6.5 mL), while keeping the temperature constant at 23 °C. After 90 minutes, the light yellow film on top of the ethylene glycol was transferred to a solid substrate. The superlattice was transferred to a TEM grid by immersion of the grid perpendicular to the EG surface. The grid was then rotated and removed from the EG parallel to the surface to "scoop" the lattice on the TEM grid. Alternatively, the superlattice was transferred to quartz glass through "stamping", *i.e.* by gently touching the quartz glass to the yellow film on the EG. Subsequently, the TEM grid or quartz glass was dried overnight under vacuum.

3.3.2 Annealing of PbSe superlattices

Two methods were employed to anneal square PbSe superlattices. The first method was adapted from Walravens *et al.* and was performed on the superlattices after transfer to a TEM grid or quartz glass[35]. The TEM grid or quartz glass was placed in a preheated Petri dish on a heating stage inside a glovebox. Samples were annealed in this way for 1 hour at temperatures between 50 °C and 100 °C. For annealing

at temperatures between 125 °C and 150 °C for the same duration, a hotplate was used instead of the heating stage.

Alternatively, the superlattices were annealed on the EG substrate after preparation of the superlattices following the procedure outlined in Section 3.3.1. To this end the temperature of the EG substrate was increased to temperatures between 38 and 50 °C for 10 to 20 minutes. This annealing method is most commonly used in literature to anneal superlattices[1, 4, 7, 18].

3.3.3 Absorption measurements on square PbSe superlattices

Fourier-transform infrared (FTIR) absorption measurements were performed on a Brucker Vertex 70 spectrometer. Samples for the absorption measurement were prepared by placing quartz glass on which a superlattice was stamped in an air-tight holder. The measurements were performed between 4000 - 10 000 cm^{-1} with a resolution of 4 cm^{-1}, averaging over 300 scans.

3.4 Cation exchange of square PbSe to CdSe superlattices

Methods adapted from Evers *et al.* and Boneschanscher *et al.* were used for the cation exchange reactions[1, 7]. A 0.1 M $Cd(OA)_2$ precursor was prepared by vigorously stirring 1.105 g $Cd(Ac)_2 \cdot 2H_2O$, 10.842 g OA and 43.25 mL ODE under vacuum (10^{-2} bar) at 120 °C for 2 hours. Inside a glovebox, 3mL $Cd(OA)_2$ solution was heated to temperatures between 100 and 175 °C. Subsequently, a superlattice on a silicon nitride grid was brought into contact with the solution for 1 - 2 hours. The exact temperatures and reaction times that were used are specified in the next chapter.

Initially, cation exchange was performed by placing a superlattice on a silicon nitride TEM grid in a Petri dish with 3 mL preheated $Cd(OA)_2$ solution. At the end of the reaction the TEM grid was removed from the Petri dish with tweezers. However, this frequently resulted in breaking of the silicon nitride window. An improved method was developed, where the TEM grids were held with self-closing tweezers during the exchange reaction and glass vials were used instead of a Petri dish. With this novel method, the silicon nitride windows of nearly all TEM grids survived the exchange reaction. The success of this method was improved even further by using TEM grids with 9 small silicon nitride windows, rather than grids with one large window.

After completion of the cation exchange reaction, the TEM grids were washed by very gently stirring the grid sequentially in toluene, a 50/50 mixture by volume of butanol and methanol and finally in methanol. The grid was washed in each of the three liquids for 30 seconds. Afterwards, the grid was allowed to dry in the glovebox atmosphere for 10 minutes.

3.5 Electron microscopy

Bright field transmission electron microscopy (TEM) images were recorded on a FEI Tecnai T-20 at an acceleration voltage of 120 kV. High-angle annular dark-field scanning transmission electron microscopy (HAADF-STEM) images and energy-dispersive X-ray (EDX) spectra were recorded on a FEI Talos F200X at an acceleration voltage of 200 kV. The average neck thickness, amount of necks per NC and the NC diameter in the superlattices in the HAADF-STEM and TEM images were determined by performing 200 measurements by hand using ImageJ software.

4 Results and Discussion

4.1 Square PbSe superlattices

In this section the results of the PbSe NC synthesis and square PbSe superlattice preparation are discussed. First, the synthesized PbSe NCs are presented and the NC size is determined by absorption spectroscopy. Then, the square lattices that were produced with these NCs are shown, after which the effect of annealing of the superlattices is discussed. Next, it is demonstrated that square PbSe superlattices produced with aged NCs show reduced long range order. The cause of the reduction is investigated and an adapted method to increase long range order in square superlattices fabricated with aged NCs is presented.

4.1.1 PbSe nanocrystals

PbSe NCs were synthesized using the method outlined in Section 3.2.1. A TEM image of the NCs is shown in Figure 4.1a. The NCs in the TEM image show hexagonal ordering, while linear aggregates can be observed as well. As explained in Section 2.3, the NCs are expected to self-assemble in the observed hexagonal monolayer during evaporation of the solvent on account of entropic factors[17, 31]. On the other hand, it seems that the ligand density on the {100} facets of some of the NCs was not high enough to prevent aggregation[33], resulting in the observed linear structures.

The absorption spectrum of the PbSe NC dispersion is shown in Figure 4.1b. The size of the PbSe NCs was determined from the first exciton peak at 0.70 eV using the empirically derived relation[24]:

$$E_0 = 0.278 + \frac{1}{0.016d^2 + 0.209d + 0.45} \tag{4.1}$$

with E_0 the energy of the first exciton transition in eV and the d the average diameter of the NCs in nm. Using this relation, an average NC diameter of 6.1 nm was calculated. Additionally, the energy integrated molar extinction coefficient of the NCs was determined with a second empirically derived relation[24]:

$$\epsilon = 3.1 * d^{0.9} \tag{4.2}$$

with ϵ in cm^{-1} meV. A NC concentration of $5.9 * 10^{-5}$ mol/L was determined for the dispersion using Beer-Lambert's law and the molar extinction coefficient determined by equation 4.2. All further experiments were performed using this PbSe NC dispersion.

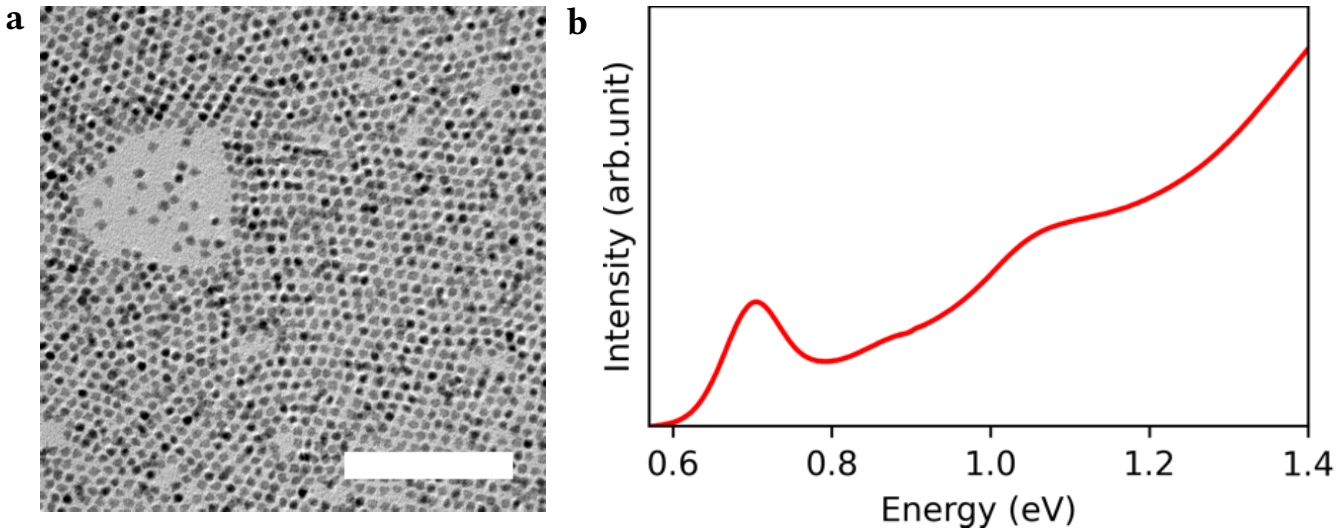

Figure 4.1: (a) TEM image of PbSe NCs from a dispersion with TCE as the solvent. Some aggregated particles can be observed in the image. Scale bar 100 nm. **(b)** Absorption spectrum of the PbSe NC dispersion in TCE. The first exciton peak of the NC dispersion is located at 0.70 eV.

4.1.2 As-formed square PbSe superlattices

Square PbSe superlattices were produced with the PbSe NCs from the previous section, using the experimental procedure outlined in Section 3.3.1. Scooping of the superlattice with a TEM grid resulted in large coverage of the grid, as shown in Figure 4.2a. The large light grey area in the image corresponds to superlattice monolayers, which typically covered $\sim$ 80% of the TEM grid. However, darker grey areas can be observed as well and are attributed to double and multi-layers. In addition, several cracks and dark black spots are visible in the film. In previous research on oriented attachment of PbSe NCs it was demonstrated that these black spots consist of selenium, although the origin of the spots is unknown[19].

A TEM image of the same sample at a higher magnification is shown in Figure 4.2b. As can be seen in this image, the superlattice shows square ordering. Apart from that, it is clear that the monolayer does not consist of a single crystalline film, but of multiple domains separated by high-angle grain boundaries. The sizes of these square domains were typically on the order of 0.1 - 0.5 μm^2 . The bond angles and center-to-center distances between the NCs in the square lattice domains were determined by Python scripts included in Appendices A and B, respectively. Average bond angles of 86°/94° were obtained for the $\sim$ 6500 NCs in the largest square lattice domain in the bottom left of Figure 4.2b. In addition, an average center-to-center distance of 6.4 nm was acquired for all $\sim$ 7000 NCs in Figure 4.2b. The bond angles of the NCs deviate by 4° from the 90° expected for perfect square ordering. Imperfect oriented attachment of NCs into square superlattices has also been described in literature, where bond

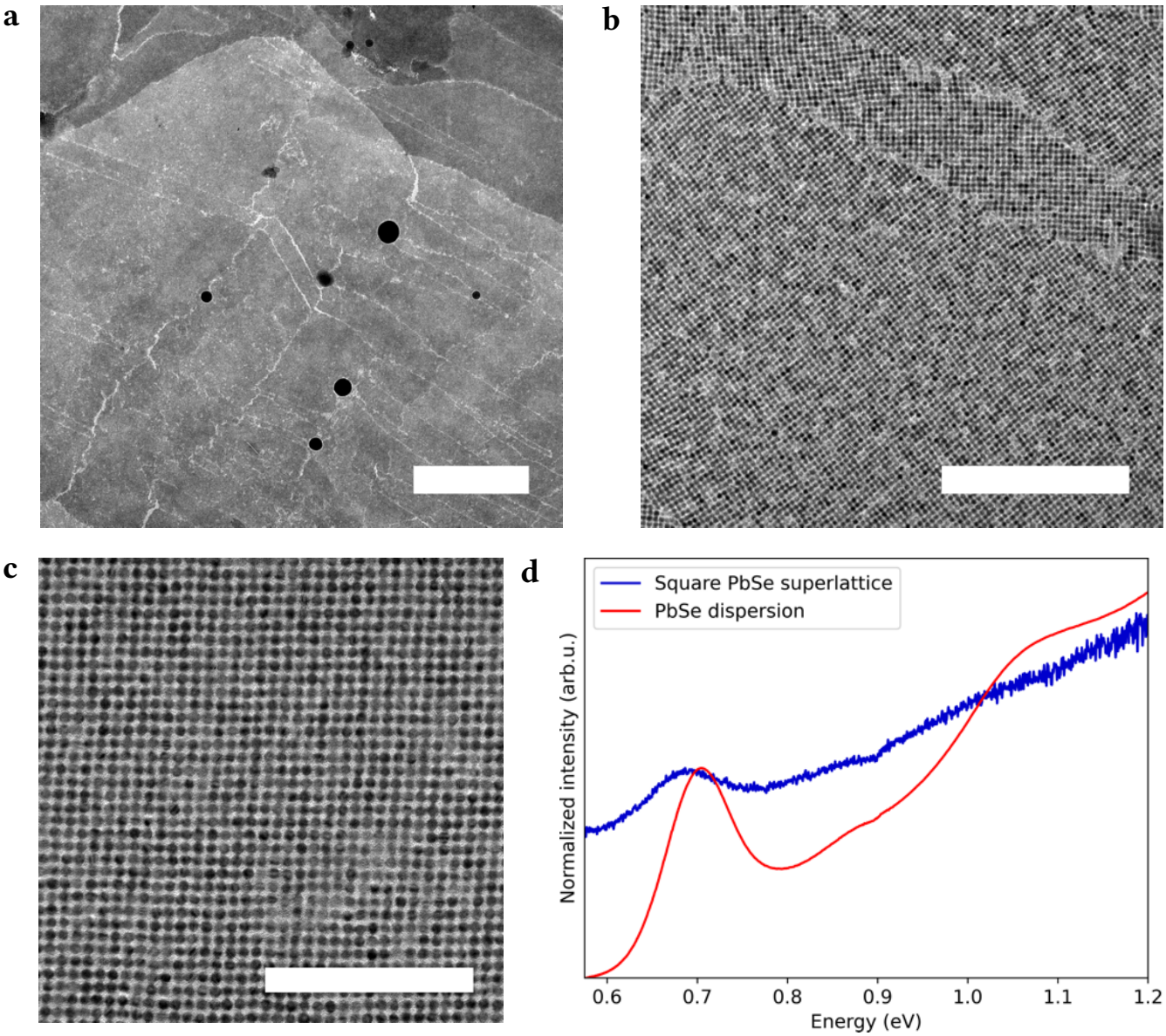

Figure 4.2: TEM images and the absorption spectrum of a square PbSe superlattice. **(a)** Overview of a square PbSe superlattice on a TEM grid, showing large coverage with several cracks and double and multi-layers in the darker areas. Dark black spots consisting of selenium are present at several regions of the lattice. Scale bar 1 µm. **(b)** A higher magnification TEM image of the same sample. Clear square ordering can be observed, present in several domains. Scale bar 200 nm. **(c)** A close up image of the same sample, showing the epitaxial connections between the NCs. Scale bar 100 nm. **(d)** The absorption spectrum of the superlattice and the NC dispersion, where both spectra have been normalized at the first exciton peak. A small red-shift of 17 meV and slight broadening of the first exciton peak can be observed for the superlattice.

angles of 83°/97° were reported. This deviation of 7° from perfect square ordering was attributed to a necessary lateral shift between the NCs to allow for Pb-Se binding between neighbouring NCs[17]. Nevertheless, we consider the superlattices presented in Figure 4.2b and in literature to be square, as the deviation from perfect square ordering of 4° or 7° is only minor.

To analyse the rotational angle between the square lattice domains in Figure 4.2b, the Python script outlined in Appendix A was used again. The details of this analysis are given in Appendix A.1. A rotational angle between the domains of 36°-39° was found. Interestingly, in all TEM images of the square superlattice the square lattice domains were separated by high-angle grain boundaries at comparable angles. This implies that low-angle grain boundaries are not formed during the square superlattice formation or that the low-angle grain boundaries can be healed during the formation of the square lattice, contrary to the observed high-angle grain boundaries. Further research is required to determine the exact cause of the formation of exclusively high-angle grain boundaries.

The epitaxial connections between the individual NCs are visible in a TEM image at an even higher magnification, shown in Figure 4.2c. The neck thickness, number of necks per NC and NC diameter in this TEM image were measured by hand. A neck thickness of 2.6 $\pm$ 0.3 nm with 2.9 $\pm$ 0.8 necks per NC and a NC diameter of 5.4 $\pm$ 0.4 nm were obtained by averaging over 200 measurements. The measured reduction of the NC diameter of approximately 0.7 nm for the NCs in the lattice can be explained by the diffusion of Pb and Se from the NCs to the necks[33, 34]. In the square superlattice not all of the four possible connections between the NCs are formed, which is also reported in literature[4]. In addition, the measured average neck thickness is in good agreement with the neck thickness of 3.0 nm reported by Wang *et al.* This neck thickness was reported for square superlattices prepared with NCs of equal size, but with domain sizes of only $\sim$0.005 μm^2[34].

Using the same Python scripts as before, average bond angles of 87°/93° and an average center-to-center distance of 6.3 nm were obtained for the $\sim$ 1250 NCs in the TEM image shown in Figure 4.2c. Hence, the bond angles and center-to-center distances between the NCs in the superlattices shown in Figure 4.2b and 4.2c are nearly identical. In all other TEM images of the square superlattice the center-to-center distances and bond angles were also in the range of 6.3 - 6.4 nm and 86°/94° - 87°/93°, respectively. Only one deviating average bond angle of 89°/91° was found. The TEM image of this area of the superlattice is shown in Figure A.4 in Appendix A.2. Nevertheless, this is only a minor deviation of 2° - 3°. Hence, it can be concluded that the superlattice geometry is uniform in nearly all of the different domains.

To investigate whether the NCs in the superlattice are electronically coupled, the absorption spectrum of the square superlattice was measured. The absorption spectra of the square superlattice and the NC dispersion are displayed in Figure 4.2d. A small red-shift of 17 meV and slight broadening of the first-exciton peak can be observed for the square superlattice, which provides further evidence that the NCs are connected by atomic bonds[4, 18, 35].

To summarize, square superlattices were produced by oriented attachment of the NCs synthesized in the previous section. Square superlattice domains with sizes around 0.1 - 0.5 μm^2 were obtained and

these domains were separated by high-angle grain boundaries. The center-to-center distance in these square lattice domains is 6.3 - 6.4 nm on average and in the majority of the domains the bond angles between the NCs are 86°/94° - 87°/93°. In addition, each NC in the square superlattice is connected by 2.9 ± 0.8 necks with a thickness of 2.6 ± 0.3 nm and shows a reduced diameter of 5.4 ± 0.4 nm. Furthermore, bond formation between the NCs could be deduced from a red-shift and peak broadening in the absorption spectrum of the as-formed superlattice. In further experiments, gentle annealing was performed on the square lattices with the aim of increasing the neck thickness. The results of these experiments are presented in the next section.

4.1.3 Annealing of square PbSe superlattices

In the work by Walravens *et al.*, square PbSe superlattices were annealed at temperatures between 75 and 150 °C. As a result, the defect density in the necks decreased while the relative neck thickness increased from 0.58 ± 0.04 up to 0.70 ± 0.02[35]. We hypothesized that the increased neck thickness and reduction of defects would increase the superlattice sturdiness, thereby increasing the likelyhood for the superlattice to survive the cation exchange process. Hence, the aim of the experiments discussed here was to reproduce the results of Walravens *et al.* with the adapted method described in Section 3.3.2. As outlined in Section 3.3.2, annealing experiments were also carried out by heating the ethylene glycol at the end of the superlattice preparation. In literature, annealing of superlattices is usually carried out in this way[1, 4, 7, 18]. However, this method resulted in the formation of significant amounts of molten structures, as shown in Appendix C.1. Consequently, this annealing procedure was abandoned and the results of all annealing experiments presented in this section were obtained by heating the square superlattice on a TEM grid. All TEM samples shown in this section were originally scooped from the same Petri dish. Therefore, we assume that all samples showed similar structures before the annealing experiments were performed.

TEM images of an as-prepared lattice and of lattices annealed at 75, 100 and 125 °C are displayed in Figures 4.3a, 4.3b, 4.3c and 4.3d, respectively. Annealing was also performed at 150 °C and a TEM image of a superlattice annealed at this temperature can be found in Appendix C.2. However, exclusively molten structures remained after annealing at 150 °C. Therefore, only lattices annealed at 75, 100 and 125 °C are considered in this section. No significant changes can be observed in the lattice annealed at 75 °C. However, vacancies can be observed in the lattices annealed at 100 and 125 °C. Moreover, several molten structures can be seen in the lattice annealed at 125 °C. To quantify any changes in the lattices, the neck thickness, number of necks per NC and NC diameter of the superlattices in Figure 4.3a, 4.3b, 4.3c and 4.3d were measured by hand. The obtained values are listed in Table 4.1. Each of these values is an average of 200 measurements. A negligible increase in the neck thickness from 2.6 ± 0.3 nm to 2.7 ± 0.4 nm was measured for the lattice annealed at 75 °C. On the other hand, a larger increase was obtained for the lattices annealed at 100 and 125 °C, for which neck thicknesses of respectively 3.0 ± 0.5 nm and 3.7 ± 0.5 nm were measured. For all superlattices an approximately constant number of necks

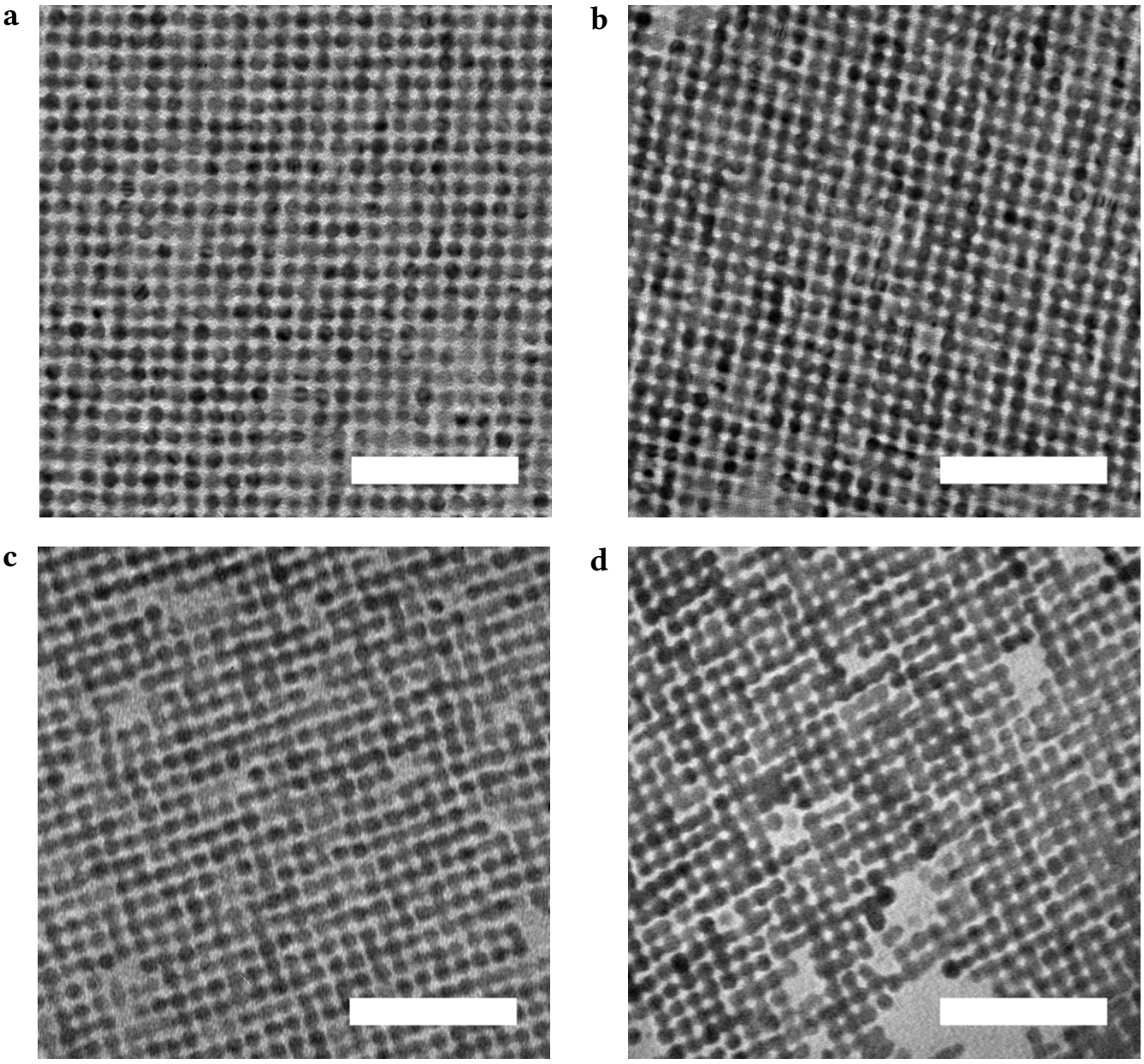

Figure 4.3: TEM images of square PbSe superlattice annealed at different temperatures. **(a)** TEM image of a superlattice that has not been annealed. **(b)** TEM image of a superlattice that has been annealed at 75 °C for 1 hour. **(c)** TEM image of a superlattice annealed at 100 °C for 1 hour. Broader necks compared to those found in **(a)** and **(b)** can be observed in this image. **(d)** TEM image of a superlattice annealed at 125 °C for 1 hour. Even thicker necks and molten structures can be observed in the lattice. All superlattice samples in these images were initially taken from the same Petri dish. Scale bars 50 nm.

Table 4.1: The average neck thickness, number of necks per NC, NC diameter and relative neck thickness (L/D) in the square superlattices after annealing at the listed temperatures. All averages were determined by performing 200 measurements by hand using ImageJ software. The measurements were performed on the TEM images of the superlattices shown in Figure 4.3.

Annealing temperature	Neck thickness (L)	Number of necks per NC	NC diameter (D)	Relative neck thickness (L/D)
No annealing	2.6 ± 0.3 nm	2.9 ± 0.8	5.4 ± 0.4 nm	0.48 ± 0.07
75 °C	2.7 ± 0.4 nm	3.1 ± 0.8	5.1 ± 0.4 nm	0.53 ± 0.09
100 °C	3.0 ± 0.5 nm	2.7 ± 0.8	5.3 ± 0.4 nm	0.57 ± 0.10
125 °C	3.7 ± 0.5 nm	3.0 ± 0.8	5.4 ± 0.5 nm	0.69 ± 0.11

per NC between 2.7 ± 0.8 and 3.1 ± 0.8 was determined. In addition, a small decrease in the NC diameter from 5.4 ± 0.4 nm to 5.1 ± 0.4 nm was measured for the superlattice annealed at 75 °C. However, the NC diameters in the lattices annealed at 100 and 125 °C of 5.3 ± 0.4 nm and 5.4 ± 0.5 nm, respectively, were nearly the same as in the as-formed lattice.

In the work by Walravens *et al.*, relative neck thicknesses were determined by normalizing the neck thickness (L) to the NC diameter (D). In their work, the obtained L/D value of the as-formed lattice was 0.58 ± 0.04 and this changed to 0.59 ± 0.03, 0.59 ± 0.02, 0.63 ± 0.03 or 0.70 ± 0.02 by annealing at 75, 100, 125 or 150 °C, respectively[35]. The L/D values of the superlattices in this work were also calculated, taking into account the propagation of uncertainty. An L/D value of 0.48 ± 0.07 is obtained for the lattice that was not annealed, while increased L/D values of 0.53 ± 0.09, 0.57 ± 0.10 and 0.69 ± 0.11 are obtained after annealing at 75, 100 and 125 °C, respectively.

From these results it follows that Walravens *et al.* obtained a larger relative neck thickness for the as-formed superlattice. Moreover, in the work by Walravens *et al.* the relative neck thickness remained approximately the same after annealing at temperatures up to 100 °C. A significant increase in the relative neck thickness was reported only for the lattices annealed at 125 or 150 °C[35]. This is in contrast with the relative neck thicknesses calculated in this work, which increased after annealing at only 75 °C. Another discrepancy is the fact that in this research exclusively molten structures were obtained after annealing at 150 °C. Moreover, the variance of the relative neck thickness increased after annealing, which is in contrast with the results obtained by Walravens *et al.* as well. In the work of Walravens *et al.* no explanation is given for the decrease in the variance of the relative neck thickness[35]. The increase in the variance measured in this work, on the other hand, could be indicative of an Ostwald ripening process during annealing. Nevertheless, the average neck thickness increases with higher annealing temperatures while the number of necks per NC remains constant. This means that the smaller necks in the lattice cannot be the only source of material. Because the material must come from somewhere, the source of this material must be the NC cores in the lattice. Even so, a slight decrease in the NC core diameter was measured only for the lattice annealed at 75 °C. An explanation

for this could be that the NCs deform during annealing, as was observed in *in-situ* measurements of the oriented attachment of PbSe NCs[33]. This would result in a reduction of the thickness of the NC cores, which would not change the diameter that is visible in the TEM images. Alternatively, it could be speculated that several NC cores in the lattice are consumed to provide the material. This could also explain the formation of vacancies in the lattices shown in Figure 4.3c and 4.3d. Further research is required to determine the exact mechanism by which both the neck thickness and the variance in the neck thickness increase during annealing. Experiments such as *in-situ* heating of the superlattices in an electron microscope could provide insight into this mechanism.

The discrepancy between the results obtained by Walravens *et al.* and those obtained in this research could be the result of the different methods that were used to produce and anneal the square superlattices. In the work by Walravens *et al.* the square superlattices were produced by adding aniline to a self-assembled monolayer of PbSe NCs on ethylene glycol[15, 35], as outlined briefly in Section 2.3. It may be possible that this causes a lower ligand density on the surface of the superlattices due to the more aggressive removal of the oleate ligands[15]. This could lead to different behaviour of the superlattice during annealing. Apart from that, in this work superlattices were annealed on a TEM grid in a preheated Petri dish on a heating stage. Walravens *et al.*, on the other hand, performed annealing by placing TEM grids containing the superlattices in a preheated nitrogen filled oven[35]. Further experiments are required to determine whether the differences in the methods affects the outcome of the annealing experiments.

Changes in the long-range order of the superlattices by annealing were investigated as well. Overview TEM images of square superlattices before annealing and after annealing at 75, 100 and 125 °C are shown in Figure 4.4a, 4.4b, 4.4c and 4.4d, respectively. As can be seen from these TEM images, annealing leads to the formation of vacancies in the lattice regardless of the annealing temperature. In addition, molten structures and unattached NCs can be seen in the TEM image of the lattice annealed at 125 °C. The observed vacancies and unattached NCs are most likely formed due to the thermal stress caused by annealing[49]. Further experiments such as *in-situ* heating of the square lattices in an electron microscope could confirm this hypothesis. Nevertheless, based on these results it can be concluded that annealing with the methods used in this work causes a decrease in the long-range order of the superlattice. The aim of this work was to maximize the long-range order in cation exchanged square lattices. Hence, this loss of long-range order by annealing is undesirable. Even so, the overall geometry is retained and therefore the lattices are still suitable to investigate the effect of annealing on the superlattice stability during cation exchange reactions.

To summarize, the neck thickness in the square superlattices could be increased by annealing at temperatures up to 125 °C. The neck thickness could be increased from 2.6 ± 0.3 nm up to 3.7 ± 0.5 nm in this way, which constitutes a change in the relative neck thickness (L/D) of 0.48 ± 0.07 up to 0.69 ± 0.11. The relative neck thickness was shown to increase after annealing at all investigated annealing temperatures. In addition, the variance in the relative and absolute neck thickness was shown to increase and it was shown that vacancies were present in the superlattice after annealing. Apart from the

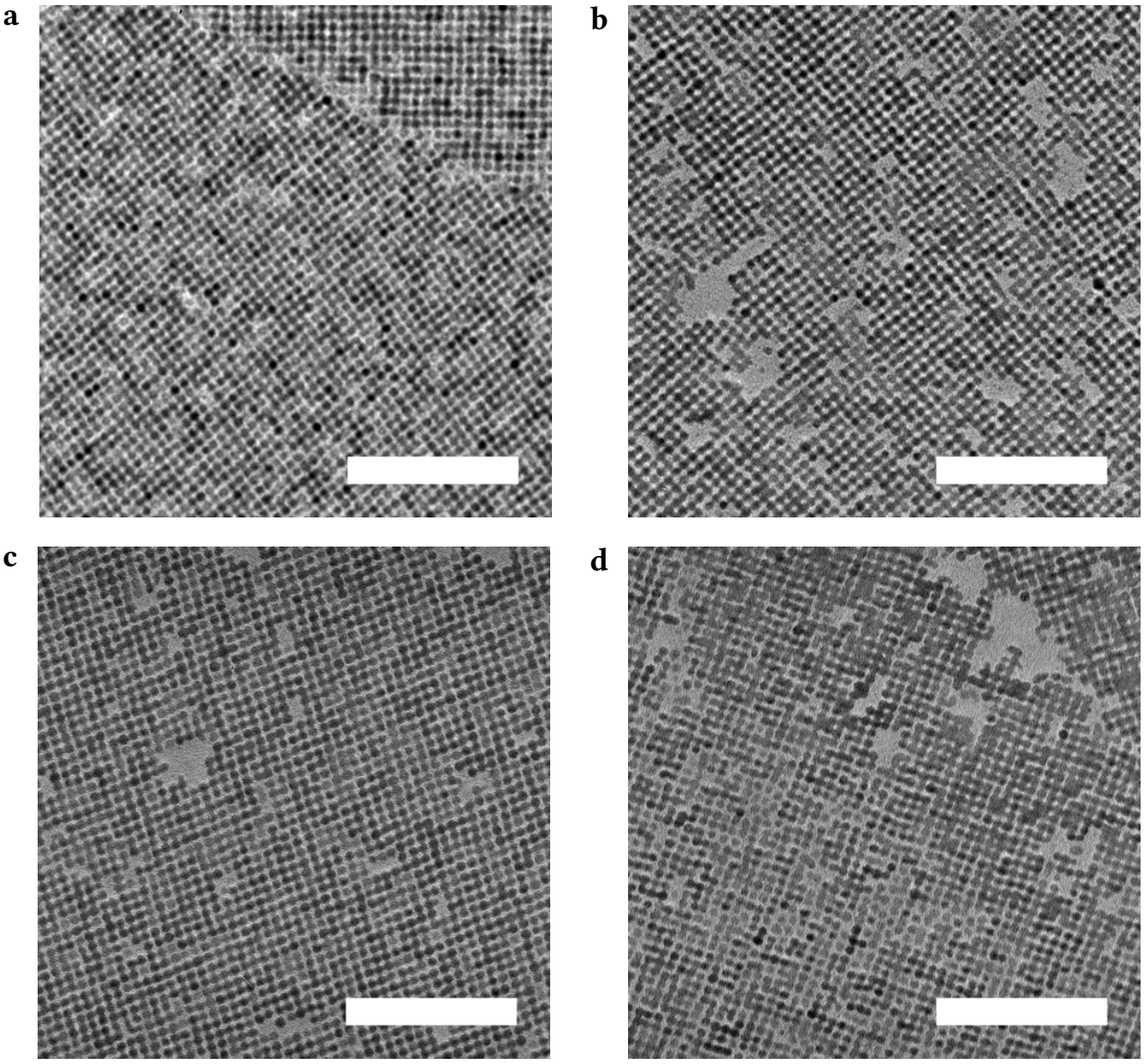

Figure 4.4: Overview TEM images of square PbSe superlattice annealed at different temperatures. In **(a)** no annealing is performed, while in **(b)** the superlattice has been annealed at 75 °C for 1 hour; in **(c)** the annealing was carried out at 100 °C for 1 hour and in **(d)** annealing was performed at 125 °C for 1 hour. As can be observed in these images, long range order and square lattice domains are largely retained, although vacancies are formed in the lattices after annealing. Moreover, in **(d)** molten structures and unattached material can be observed as well. All superlattice samples in these images were initially taken from the same Petri dish. Scale bars 100 nm.

vacancies, unattached NCs and molten structures were observed in the superlattice annealed at 125 °C as well. These results are in contrast with what was reported by Walravens *et al.* Further experiments are required to investigate the cause of the discrepancy. Nevertheless, the neck thickness could be increased while retaining the square geometry of the superlattice by annealing at a temperature up to 125 °C. Since the long-range order was lost to a greater extent for the superlattice annealed at 125 °C, the annealing temperature of 100 °C was chosen as the optimum.

4.1.4 Ageing of PbSe NCs and the effect on superlattice formation

Five months after the optimal annealing temperature of the superlattices was determined, reproducing the results obtained in Section 4.1.2 and 4.1.3 became difficult. In this section the superlattices produced at this later time are presented and a possible explanation for the loss of reproducibility is given.

A TEM image of an as-formed square superlattice prepared with the method outlined in Section 3.3.1 is shown in Figure 4.5a. Large vacancies and molten structures can be observed in the lattice, despite the fact that the superlattices in Section 4.1.2 were prepared with the same method. In Figure 4.5b these molten structures can be observed at the grain boundaries of the different lattice domains. In addition, only small square lattice domains with a size of $\sim$0.01 μm^2 are visible in this TEM image. The largest domains were typically $\sim$0.1 μm^2 in size, which is lower than the $\sim$0.1 - 0.5 μm^2 obtained for

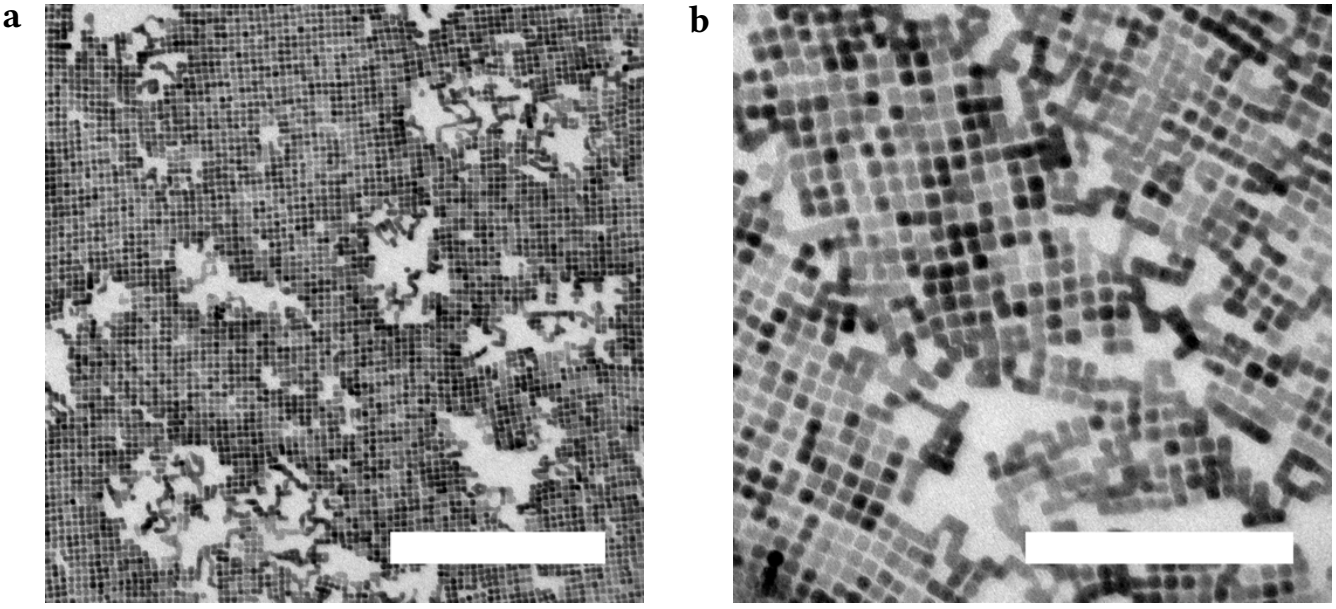

Figure 4.5: TEM images of square superlattices produced 5 months after initial experiments. **(a)** TEM image of a square superlattice containing molten structures. Scale bar 200 nm. **(b)** TEM image of a square superlattice sample showing the presence of multiple, smaller square domains. Scale bar 100 nm.

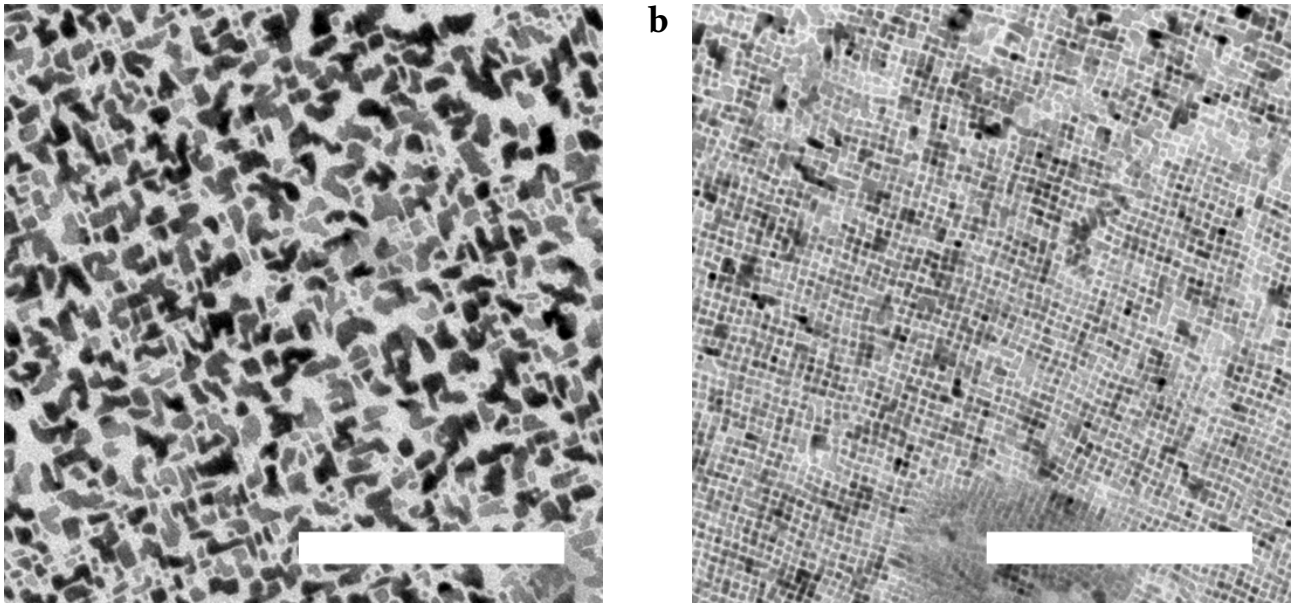

Figure 4.6: TEM images of square superlattices annealed at 75 °C, produced 5 months after initial experiments. **(a)** TEM image of the annealed superlattice where melting of the lattice led to a complete loss of the square superlattice structure. **(b)** TEM image of the same sample as in **(a)**, showing that some square superlattice domains remained. However, molten structures and unattached material can be observed here as well. Scale bars 200 nm.

the as-formed square lattices presented in Section 4.1.2. The large domains spanned ∼20% of the TEM grid, while the smaller domains were present on the other ∼80%. The observed molten structures have been reported in literature as well[5, 50]. The formation of these molten structures was attributed to stripping of the oleate ligands off the NC surface by oxygen[5], or by replacement of the ligands with methanol[50]. The molten structures then formed due to the rapid oriented attachment of the NCs. The reduced square lattice domain sizes could be explained by rapid oriented attachment as well. Possibly, irreversible oriented attachment occurs before self-assembly of the NCs in a monolayer with long-range order.

The results of the annealing experiments differed from the previously obtained results, presented in Section 4.1.3, as well. A TEM image of a superlattice annealed at 75 °C for 1 hour is displayed in Figure 4.6a. As can be seen in this image, only molten structures remained after annealing. This is in stark contrast to the superlattices shown in Figure 4.3b and 4.4b, where annealing using the same method only led to a small decrease in the average diameter of the NC cores. It should be noted that on ∼10% of the TEM grid superlattices with square order remained, as shown in Figure 4.6b. However, in these square lattices molten structures and unattached material were also present, leading to a disruption of the long range order.

In the glovebox where the NC dispersion was stored, oxygen and water levels usually fluctuated

between 0-5 ppm and 5-10 ppm, respectively. However, during the experiments the oxygen levels in the glovebox were always reduced to below 0.1 ppm. In addition, no ligand stripping compounds which could induce rapid oriented attachment, such as alcohols[50, 51] or amines[15], were present in the glovebox. Therefore, it is unlikely that rapid oriented attachment of the NCs was caused by oxidation or fast ligand stripping during the superlattice preparation. Instead, it seems more likely that ligand desorption or oxidation of the NCs has taken place in the NC dispersion over time. It is possible that the reduced ligand density of the NCs that would result from these processes causes fast oriented attachment, leading to the observed molten structures and smaller domain sizes.

To assess whether NCs have oxidized over time while stored in the glovebox, a new UV-Vis absorption spectrum was taken. Both the old and the new spectrum are shown in Figure 4.7. Previous research has shown that oxidation of PbSe NCs results in a significant blue-shift of approximately 90 meV for PbSe NCs with a diameter of 6.3 nm[52]. However, the spectra measured here are virtually the same, with a blue-shift of approximately 1 meV. Therefore, it can be concluded that oxidation of the NCs has not taken place.

FTIR spectra of the NC dispersion were taken as well to investigate possible changes in the ligand density of the NCs. The spectra, taken approximately 7 months apart, are displayed in Figure 4.8a. It should be noted that at the time that the initial spectrum was taken, no molten structures were obtained

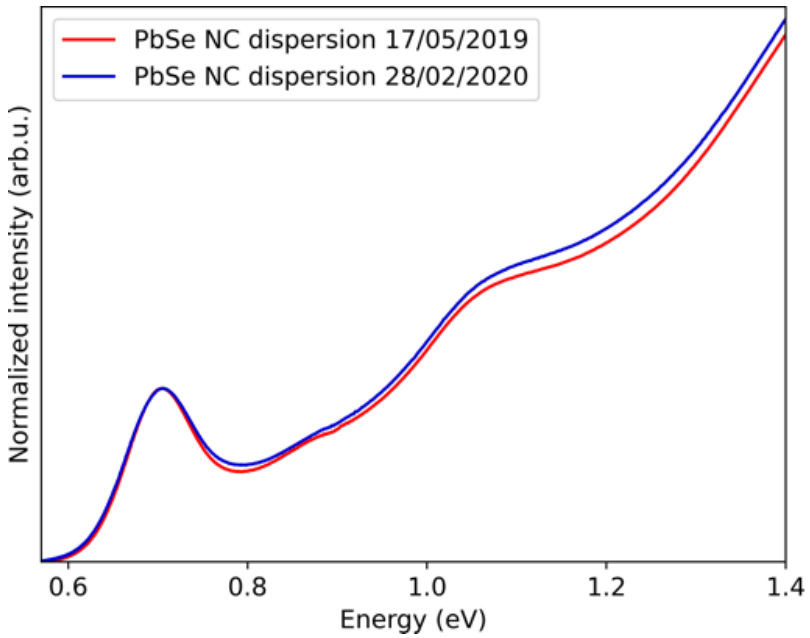

Figure 4.7: Comparison of UV-Vis absorption spectra of the NC dispersion taken 9 months apart. The spectra have been normalized at the first exciton peak of the NCs. No significant blueshift of the first exciton peak can be observed in the spectrum that was taken approximately 9 months later.

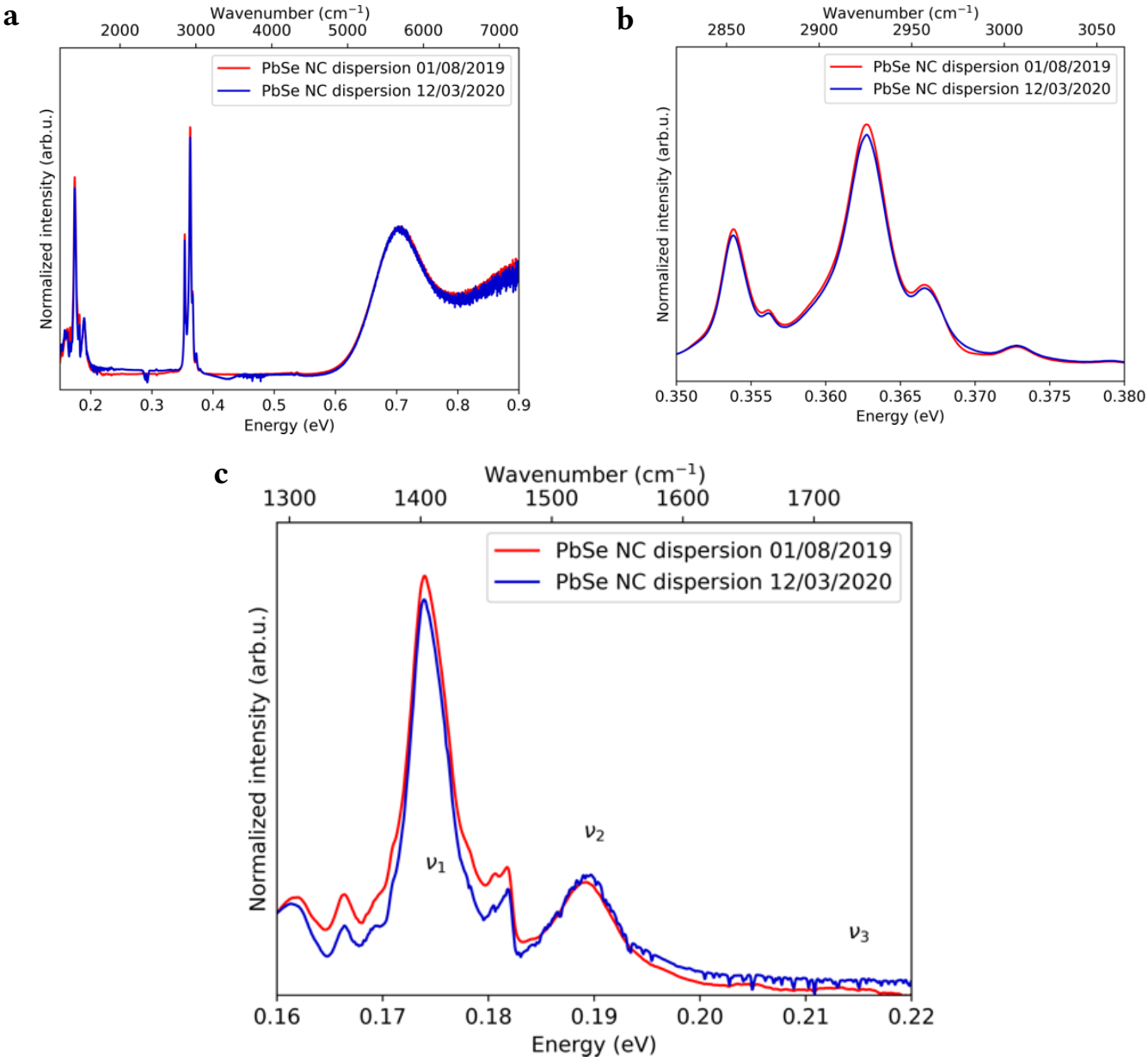

Figure 4.8: Comparison of FTIR absorption spectra of the NC dispersion taken 7 months apart. Both the energy and wavenumber of the incident radiation are plotted on the x-axes of the spectra. **(a)** FTIR spectrum of the NC dispersion. The spectra have been normalized at the intensity of the first exciton peak of the NCs. A slope, some dips and noise can be observed in the more recently obtained spectrum. **(b)** The same FTIR spectrum zoomed in on the region between 0.350 and 0.380 eV. The peaks in this area correspond to the CH-stretch vibrations of oleate ligands or oleic acid molecules. **(c)** The FTIR spectrum zoomed in on the region between 0.160 and 0.220 eV. Large peaks can be observed for the symmetric (ν_1) and the asymmetric (ν_2) carboxyl stretch vibrations. No peaks corresponding to oleic acid, which would appear at ν_3[25], can be observed.

after superlattice preparation. By contrast, these structures were obtained at the time that the later spectrum was measured. Unfortunately, the spectrum that was taken after 7 months contains a slope, several dips and noise, which makes comparison of the two spectra difficult. Nevertheless, an analysis of the spectra was still attempted.

In Figure 4.8b the FTIR spectrum between 0.350 and 0.380 eV is shown. In this region peaks corresponding to the different CH-stretch vibrations of the oleate ligands can be observed. The integrated area under these peaks can be used to determine the amount of oleate moieties present in the dispersion[25]. As only minor changes can be observed in this part of the spectrum, the amount of oleate moieties in the dispersion appears to have remained unchanged. This result is as expected, because desorbed ligands would remain in the dispersion as lead oleate, which is indistinguishable from oleate bound to the NC surface in this region of the spectrum[25].

Figure 4.8c displays the region in the FTIR spectrum between 0.160 and 0.220 eV, where the carboxyl stretch vibrations of the oleate ligands can be observed. Three regions of interest have been marked in the spectra as ν_1, ν_2 and ν_3. In both spectra peaks are visible at ν_1 and ν_2, while no peaks can be observed at ν_3. Compared to the spectrum that was taken initially, the spectrum taken at 12/03/2020 shows a reduced peak intensity at ν_1 and an increase of the peak intensity at ν_2. In addition, the distance between the peaks at ν_1 and ν_2 in the spectrum taken at 12/03/2020 has increased by approximately 4 cm^{-1}. The two peaks at ν_1 and ν_2 are attributed to symmetric and asymmetric carboxyl stretch vibrations, respectively. In a lead oleate solution the peaks at ν_1 and ν_2 show equal intensity. In addition, for a lead oleate solution the distance between the peaks at ν_1 and ν_2 is 10 cm^{-1} larger compared to a well-washed NC dispersion containing only surface bound oleate ligands[25]. Consequently, the lowering of the peak intensity at ν_1 and the increase of the peak intensity at ν_2 in the spectrum taken at 12/03/2020 indicate an increase in the lead oleate concentration in the dispersion over time. This conclusion is supported by the increase of the distance between the positions of the peaks at ν_1 and ν_2 for the spectrum taken at 12/03/2020. Finally, peaks at ν_3 would be attributed to monomer and dimer H-bonded C=O stretching vibrations of oleic acid molecules[25]. The absence of peaks at ν_3 therefore indicates that no oleic acid was present in the dispersion at either time. Consequently, an increase in the lead oleate concentration must be caused by the desorption of oleate ligands from the NC surfaces. The FTIR spectra in Figure 4.8c therefore indicate that ligands have indeed desorbed over time.

To summarize, superlattices with domain sizes between $\sim$0.01 - 0.1 μm^2 were obtained after the initial experiments presented Section 4.1.2 and 4.1.3. This is a reduction in domain size compared to the sizes of $\sim$0.1 - 0.5 μm^2 that were obtained initially. Moreover, large vacancies and molten structures were observed in the superlattices presented in this section. Oxidation of the NCs over time was ruled out as a cause due to the absence of a blue-shift of the first exciton peak of the NCs. On the other hand, based on the FTIR spectra presented in this section it seems plausible that desorption of ligands has occurred over time. The desorption of ligands could be the cause of the formation of the molten structures in the superlattices. However, care must be taken when drawing conclusions based on the FTIR spectra presented here. The observed differences in Figure 4.8c could also be caused or influenced

by the slope and the noise in the spectrum that was recorded after 7 months. Therefore, the FTIR absorption measurement should be repeated to obtain a spectrum without a slope and with less noise. This way more accurate conclusions regarding changes in the ligand density of the NCs could be drawn. In further experiments an attempt was made to re-optimize the method of superlattice preparation, so that square PbSe superlattices with long-range order could be obtained again. The results of these experiments are presented in the next section.

4.1.5 Re-optimization of the superlattice preparation

In the experiments discussed in this section, an attempt was made to re-optimize the superlattice preparation method. The goal was to reduce rapid oriented attachment of NCs, so that superlattices with enhanced long-range order and with a reduced amount of molten structures could be obtained. This was attempted by cooling the ethylene glycol substrate to 15 °C before dropcasting of the NC dispersion as described in Section 3.3.1.

Superlattice perparation at 15 °C for 90 minutes

In Figure 4.9a a TEM image is shown of an ordered superlattice prepared at a temperature of 15 °C for 90 minutes. No molten structures can be observed in this TEM image, although the square order in lattice appears to be distorted. A TEM image of the ordered superlattice at a higher magnification is given in Figure 4.9b. The order of this part of the lattice seems to be closer to square compared to the lattice shown in Figure 4.9a. A TEM image of a more disordered area of the superlattice is shown in Figure 4.9c. Double layers can be observed in the dark areas in this TEM image and the square ordering is distorted in several areas of the lattice. A higher magnification TEM image of a disordered area of the lattice is given in Figure 4.9d. A mixture of square and hexagonal ordering of the NCs can be observed in this TEM image. The ordered and disordered areas spanned respectively ∼60% and ∼40% of the TEM grid.

The Python scripts outlined in Appendix A and B were used to determine the bond angles and center-to-center distances between the NCs in these superlattices. Average bond angles of 80°/100° and 85°/95° were found for the NCs in the ordered superlattices in Figure 4.9a and 4.9b, respectively. For the disordered superlattices in Figure 4.9c and 4.9d, on the other hand, average bond angles of respectively 82°/98° and 77°/103° were obtained. Moreover, an average center-to-center distance of 6.1 nm was obtained for the lattice shown in Figure 4.9a, while a center-to-center distance of 6.8 nm was obtained for the lattices shown in Figure 4.9b and 4.9d. For the lattice shown in Figure 4.9c, a center-to-center distance of 7.0 nm was acquired. These bond-angles and center-to-center distances were determined for ∼11000, ∼1100, ∼6000 and ∼1000 NCs for the images in Figure 4.9a, 4.9b, 4.9c and 4.9d, respectively. The bond-angles and center-to-center distances found for other TEM images of this superlattice all fell in the same range of 77°/103° - 85°/95° and 6.1 nm - 7.0 nm, respectively.

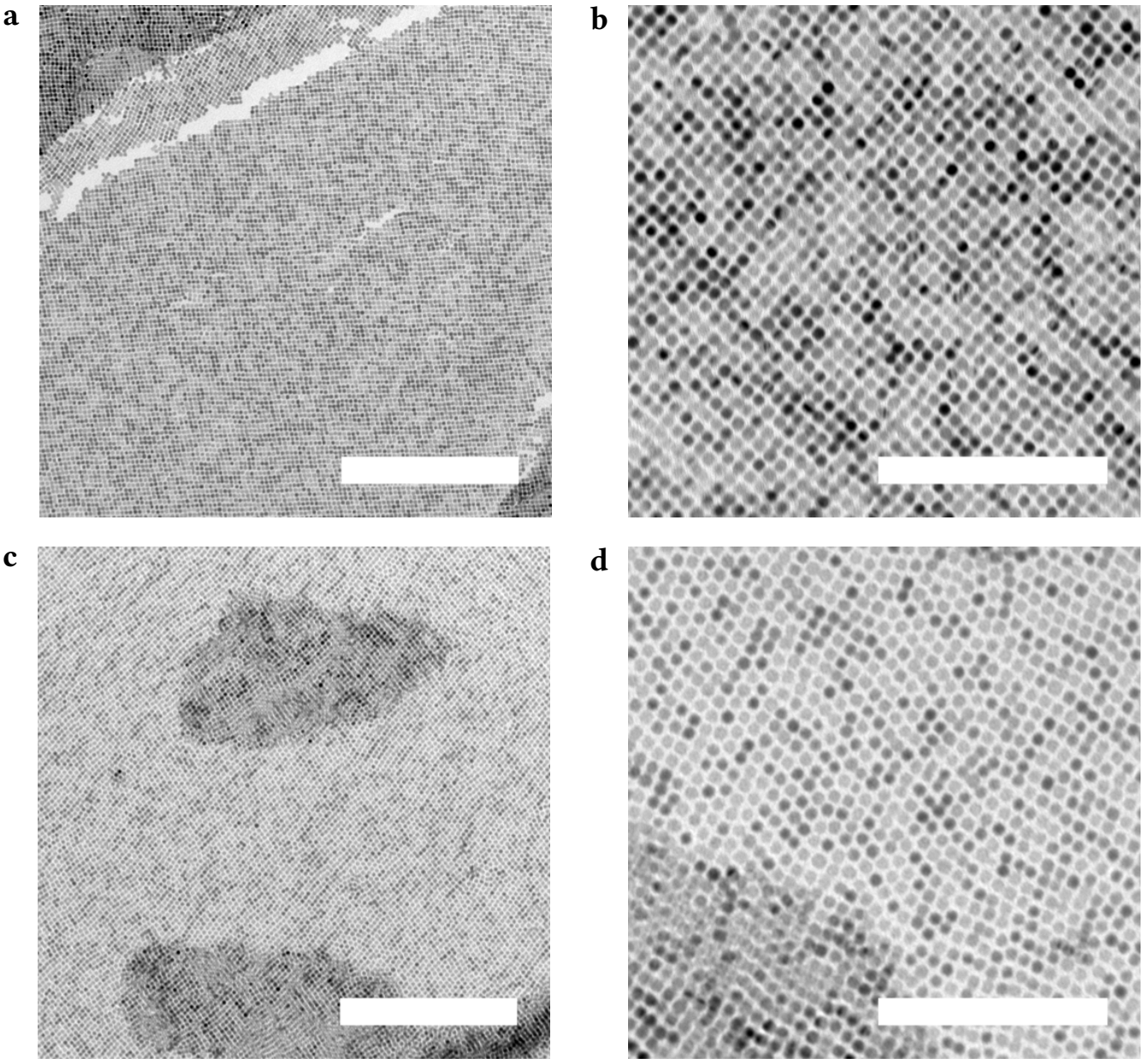

Figure 4.9: TEM images of superlattices prepared at 15 °C for 90 minutes. **(a)** TEM image of the superlattice showing slightly distorted square ordering of the NCs. No molten structures can be observed in this TEM image. **(b)** TEM image at a higher magnification, showing the square ordering of the superlattice. **(c)** TEM image of the same sample at a different area, showing a disordered lattice with both square and hexagonal ordering of the NCs. Double layers can be observed at the dark areas in the image. **(d)** Higher magnification TEM image of a disordered area of the superlattice, showing a mixture of hexagonal and square ordering, as well as a double layer at the bottom left corner of the image. Scale bars **(a)** and **(c)** 250 nm. Scale bars **(b)** and **(d)** 100 nm.

The bond angles of 77°/103° - 85°/95° deviate from the bond angles of 86°/94° - 87°/93° that were found for the square superlattices presented in Section 4.1.2. In addition, the center-to-center distances between 6.8 and 7.0 nm for the lattices shown in Figure 4.9b, 4.9c and 4.9d are larger than the center-to-center distance of 6.3 nm - 6.4 nm that was found for the superlattices presented in Section 4.1.2. As explained in Section 2.3, the formation of square superlattices proceeds through phase transitions of a self-assembled monolayer of NCs. In this process, a pseudo-hexagonal lattice with a bond angle of 55°/70° transforms into a square lattice with a bond angle of 90°. During this process, the center-to-center distance between the NCs decreases as well[17]. Hence, from the calculated bond angles in the superlattices shown in Figure 4.9 it follows that the NCs in these superlattices are ordered in a phase between pseudo-hexagonal and square. This indicates that the formation of the square superlattice was not completed after 90 minutes. This conclusion is also supported by the relatively large center-to-center distance that was obtained for the superlattices shown in Figure 4.9b, 4.9c and 4.9d.

A striking difference can be observed between the superlattices prepared at 23 °C, shown in Figure 4.5, and those prepared at 15 °C, shown in Figure 4.9. Especially considering that the only difference in the preparation method of these lattices is a temperature difference of 8 °C. The cause of the strong effect of the lowered temperature could not be determined in this work. However, in previous work an oleic acid crystal phase with a melting point below 16 °C was demonstrated[53, 54]. Therefore, it could be speculated that desorbed ligands or the oleate ligands on the NC surface also form some sort of crystal phase during superlattice preparation at 15 °C. This could explain the significant slowing of oriented attachment despite the minor difference in the reaction temperature of 8 °C. However, the experiments demonstrating the crystallization were performed with high purity oleic acid. Hence, it does not follow naturally that the oleate ligands or desorbed lead oleate also crystallize at these temperatures. Further experiments are required to determine whether crystallization of the ligands or of desorbed lead oleate is the cause of the significant reduction of rapid oriented attachment in the experiment described here.

Superlattice perparation at 15 °C for 4 hours

In further experiments, the superlattice preparation at 15 °C was performed with a longer reaction time in an attempt to obtain fully formed square superlattices. In Appendix D it is demonstrated that the superlattice formation was also not complete after preparation of the square superlattice at 15 °C for 3 hours. Hence, the reaction time was increased to 4 hours. A TEM image of a superlattice prepared with this method is shown in Figure 4.10a. Both molten structures and large vacancies can be seen in this TEM image. A TEM image at a higher magnification of the superlattice is shown in Figure 4.10b. In addition to a grain boundary and molten structures, the epitaxial connections between the NCs can clearly be seen in this image. The bond angles and center-to-center distances between the NCs in the lattices were determined using the Python scripts in Appendix A and B. An average bond angle of 90° and a center-to-center distance of 6.6 nm were obtained for the ∼9500 NCs in Figure 4.10a. For the ∼500 NCs in the bottom part of Figure 4.10b an average bond angle of 88°/92° was obtained. Furthermore,

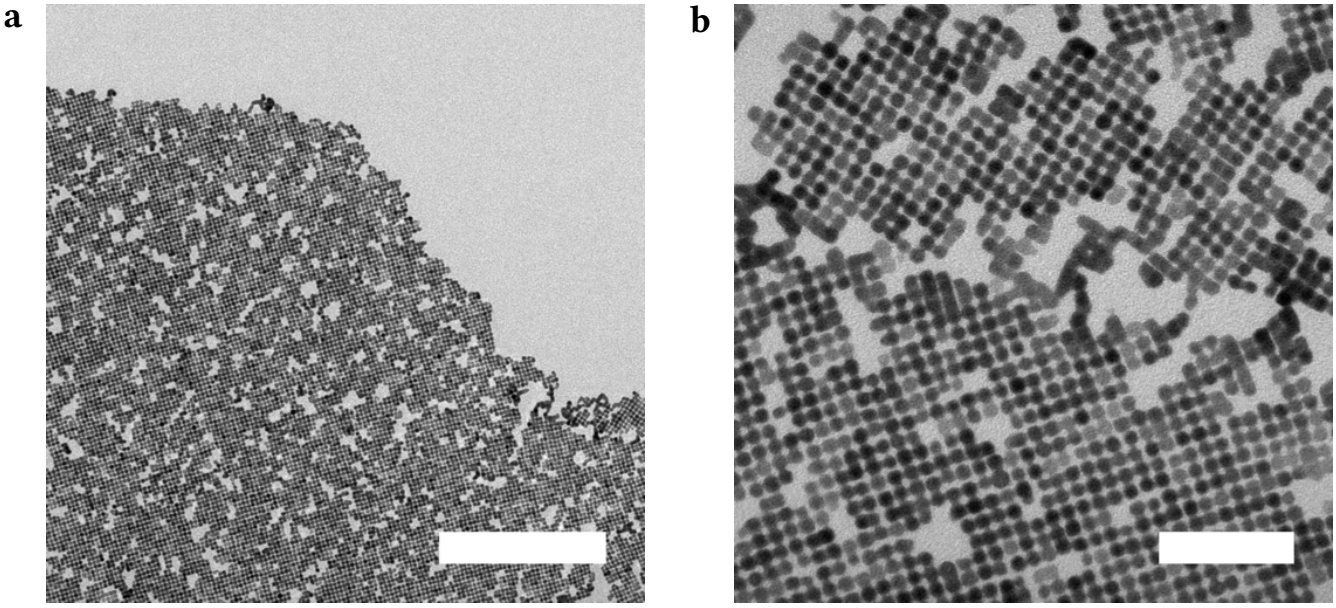

Figure 4.10: TEM images of a superlattice prepared at 15 °C for 4 hours. **(a)** TEM image of a superlattice in which a large number of vacancies can be observed. In addition, molten structures can be seen at several areas of the superlattice. Scale bar 250 nm. **(b)** Higher magnification TEM image of a grain boundary. The molten structures can clearly be observed in this image. Scale bar 50 nm.

an average center-to-center distance of 6.3 nm was determined over all ∼900 NCs in Figure 4.10b. The bond angles and center-to-center distances between NCs in all other TEM images of this superlattice were in the same range of 88°/92° - 90° and 6.3 - 6.6 nm, respectively.

The bond angles obtained for the lattice prepared at 15 °C for 4 hours correspond to perfect to nearly perfect square ordering of the NCs. In addition, the center-to-center distances between 6.3 - 6.6 nm are close to the distance of 6.3 - 6.4 nm of the lattices presented in Section 4.1.2. Hence, based on the average center-to-center distances and bond angles of the superlattice it can be concluded that the square superlattice formation has completed. This conclusion is also supported by the observation of epitaxial connections between NCs in Figure 4.10b. However, the superlattices contain large vacancies and some molten structures. Hence, this method is not suitable for obtaining square superlattices with enhanced long-range order.

Superlattice perparation at 15 °C for 1 hour and 23 °C for 90 minutes

In further experiments the reaction temperature was increased from 15 °C to 23 °C 1 hour after drop-casting of the NC dispersion on the ethylene glycol substrate. The superlattice was then scooped on a TEM grid after another 90 minutes at 23 °C, similar to the original procedure used in Section 4.1.2. The

idea behind this method was that the NCs could self-assemble in a monolayer at 15 °C by preventing rapid oriented attachment of the NCs. Subsequently, the formation of the square superlattice would be induced by increasing the temperature. Figure 4.11a shows a TEM image of a superlattice prepared by this method. The superlattice shows long-range, square order as is evident from the sharp dots in the FFT of the image. However, molten structures can be observed at several areas of this superlattice as well. The epitaxial connections between the NCs can be observed in a TEM image of the square lattice at a higher magnification, shown in Figure 4.11b. These square domains with sizes of ∼0.1 - 0.2 μm^2 covered ∼20% of the TEM grid. Nevertheless, areas with largely molten structures could be observed in this sample as well, as shown in the TEM image in Figure 4.11c. In addition, a double layer can be observed in the top right of the TEM image shown in Figure 4.11c. These areas with molten structures and double layers typically covered the other ∼80% of the TEM grid.

The Python scripts given in Appendix A and B were used to determine the bond angles and center-to-center distances between the NCs in the superlattices. For the lattices in Figure 4.11a, 4.11b and 4.11c, the average bond angles and center-to-center distances were determined over ∼5000, ∼1500 and ∼1000 NCs, respectively. Average bond angles of 89°/91° were obtained for the superlattices shown in Figure 4.11a and 4.11b. For the superlattice shown in Figure 4.11c an average bond angle of 90° was determined. These bond angles are representative for all other TEM images taken of this superlattice. In addition, an average center-to-center distance of 6.6 nm was determined for the lattice shown in Figure 4.11a, while an average center-to-center distance of 6.1 and 6.2 nm were obtained for the lattices presented in Figure 4.11b and 4.11c, respectively. The center-to-center distances in all other TEM images of this superlattice were between 6.1 and 6.6 nm. These center-to-center distances deviate from the 6.3 - 6.4 nm obtained for the lattices shown in Section 4.1.2. In addition, bond angles between 86°/94° and 87°/88° were determined for the lattices in Section 4.1.2. Hence, the bond angles in the lattices prepared at 15 °C for 1 hour and 23 °C for 90 minutes deviate as well.

Apart from the average center-to-center distances and bond angles, the neck thickness, number of necks per NC and NC diameter in the lattice in Figure 4.11b were determined as well. A neck thickness of 3.1 ± 0.4 nm, with an average of 2.7 ± 0.9 necks per NC and a NC diameter of 5.7 ± 0.4 nm were obtained by performing 200 measurements by hand. Based on these measurements, a relative neck thickness of 0.54 ± 0.08 is obtained for the lattice prepared at 15 °C for 1 hour and 23 °C for 90 minutes. The number of necks per NC measured here is approximately the same as the 2.9 ± 0.8 obtained for the lattices in Section 4.1.2. However, a neck thickness and NC diameter of respectively 2.6 ± 0.3 nm and 5.4 ± 0.4 nm were measured for the lattices in Section 4.1.2, which constituted a relative neck thickness of 0.48 ± 0.07. Hence, the neck thickness, NC diameter and relative neck thickness measured for the lattice prepared at 15 °C for 1 hour and 23 °C for 90 minutes are larger than those presented in Section 4.1.2. In fact, the relative neck thickness of 0.54 ± 0.08 is closer to the relative neck thickness of 0.53 ± 0.09 calculated for the lattice annealed at 75 °C. This discrepancy is most likely caused by the changes in the preparation method and the presumed decrease in the ligand density of the NCs, outlined in Section 4.1.4. Nevertheless, for the aged NCs the square superlattice domain sizes were increased from

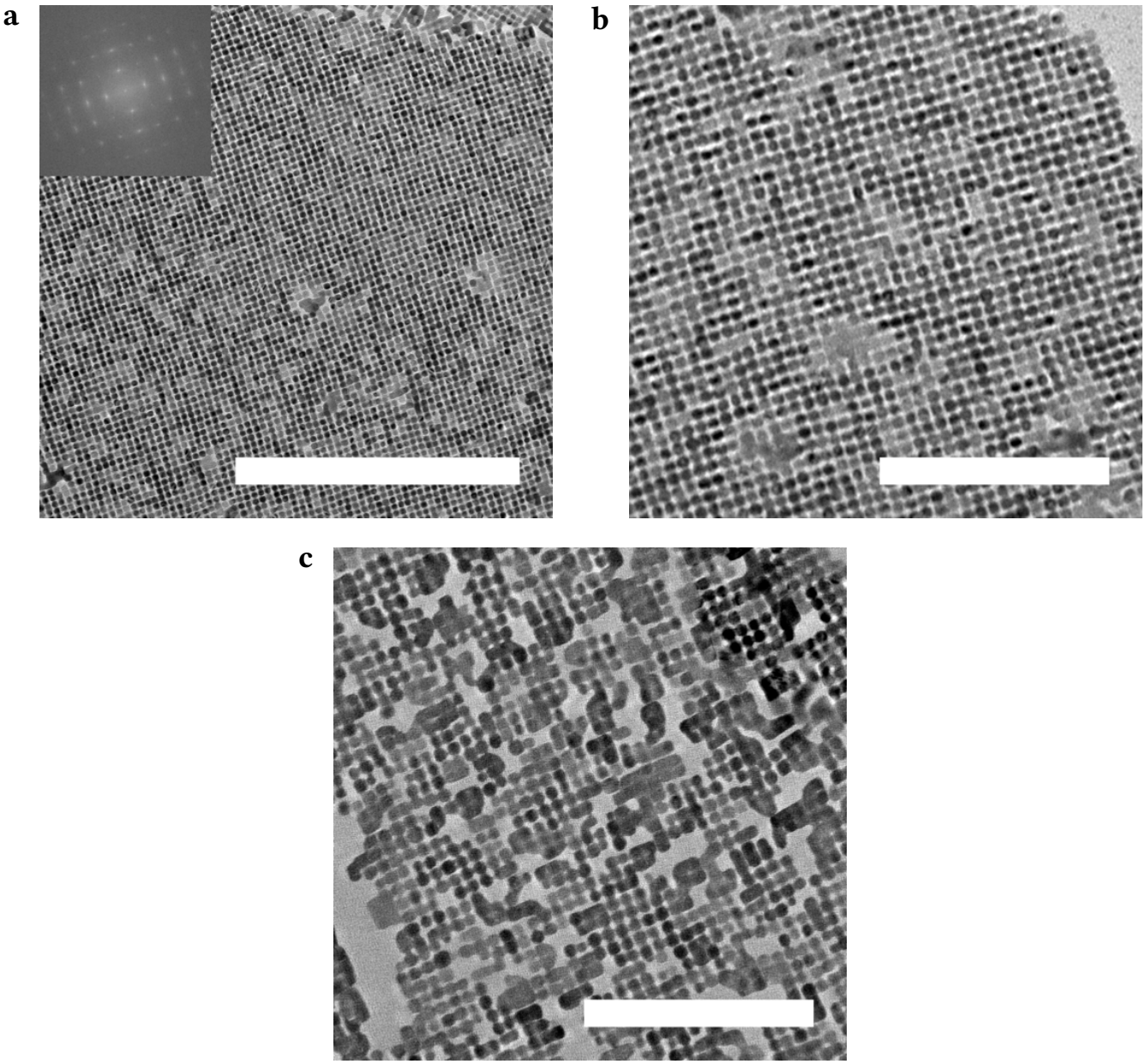

Figure 4.11: TEM images of superlattices prepared at 15 °C for 1 hour and 23 °C for 90 minutes. **(a)** TEM image of the superlattice with the FFT of the image in the top left corner. Long-range square ordering can be observed for the lattice. Scale bar 250 nm. **(b)** Higher magnification TEM image of the square lattice, showing clear epitaxial connections between the NCs. Some areas of molten structures can be observed in the lattice as well. Scale bar 100 nm. **(c)** TEM image of a different area of the same sample showing largely molten structures and a double layer in the top right of the image. Scale bar 100 nm.

$\sim$0.01 - 0.1 μm^2 to $\sim$0.1 - 0.2 μm^2 by preparing the superlattices at 15 °C for 1 hour and 23 °C for 90 minutes. Moreover, the number of vacancies in the large square lattice domains were reduced by this new method, as evident from the TEM images in Figure 4.5a and 4.11a. Therefore, for the aged NCs it can be concluded that fully-formed square superlattices with improved long-range order can be obtained by preparation at 15 ° for 1 hour and at 23 °C for 90 minutes. This method will hereafter be referred to as the "new method".

Annealing of square superlattices prepared with the new method

The annealing experiments discussed in Section 3.3.2 were repeated on the square lattices prepared with the new method. Figure 4.12a shows a TEM image of a superlattice produced with the new method that was annealed at 75 °C for 1 hour. In contrast with the results of the annealing experiments performed in Section 4.1.3, this annealing step resulted in a completely molten lattice. Hence, it appears that the thermal stability of the superlattice has reduced significantly. In view of this strongly reduced thermal stability, the experiment was repeated at a lower annealing temperature of 50 °C, also for the duration of 1 hour. A TEM image of this annealed lattice is shown in Figure 4.12b. In spite of the lower annealing temperature, significant melting of the lattice can still be observed in this image. The mix of molten structures and square superlattice shown in Figure 4.12b were observed in all other TEM images of the superlattice as well.

The neck thickness, number of necks per NC and NC diameter in the lattice annealed at 50 °C were measured by hand. A neck thickness of 3.8 ± 0.6 nm, with 3.0 ± 0.8 necks per NC and a NC diameter of 6.3 ± 0.6 nm were obtained as averages of 200 measurements. The increase in the neck thickness from 3.1 ± 0.4 to 3.8 ± 0.6 nm and the NC diameter from 5.7 ± 0.4 to 6.3 ± 0.6 nm indicates that material has migrated into the square lattice during the formation of the molten structures. With the measured neck thickness and NC diameter, a relative neck thickness of 0.60 ± 0.11 was calculated. As expected, this is an increase from the relative neck thickness of 0.54 ± 0.08 found for the as-formed superlattice. The relative neck thickness of 0.60 ± 0.11 is between the values of 0.57 ± 0.10 and 0.69 ± 0.11 calculated in Section 3.3.2 for the lattices annealed at 100 and 125 °C, respectively. This high relative neck thickness of the lattice annealed at 50 °C can be explained by the higher relative neck thickness and reduced thermal stability of the as-formed square superlattice produced with the new method. However, the increased relative neck thickness of the square PbSe superlattice after annealing at 50 °C also resulted in the formation of many molten structures, which disrupts the long-range order of the superlattice. Hence, preparation of square CdSe superlattices with long-range order from these annealed lattices is not possible. Nevertheless, cation exchange reactions could still be performed on this annealed lattice to study the effect of annealing on the superlattice stability during cation exchange. If larger areas of the annealed superlattice remain after cation exchange, this would be a good indication that annealing is beneficial for the retention of square domain sizes.

In summary, the rapid oriented attachment of NCs could be slowed down significantly by lowering

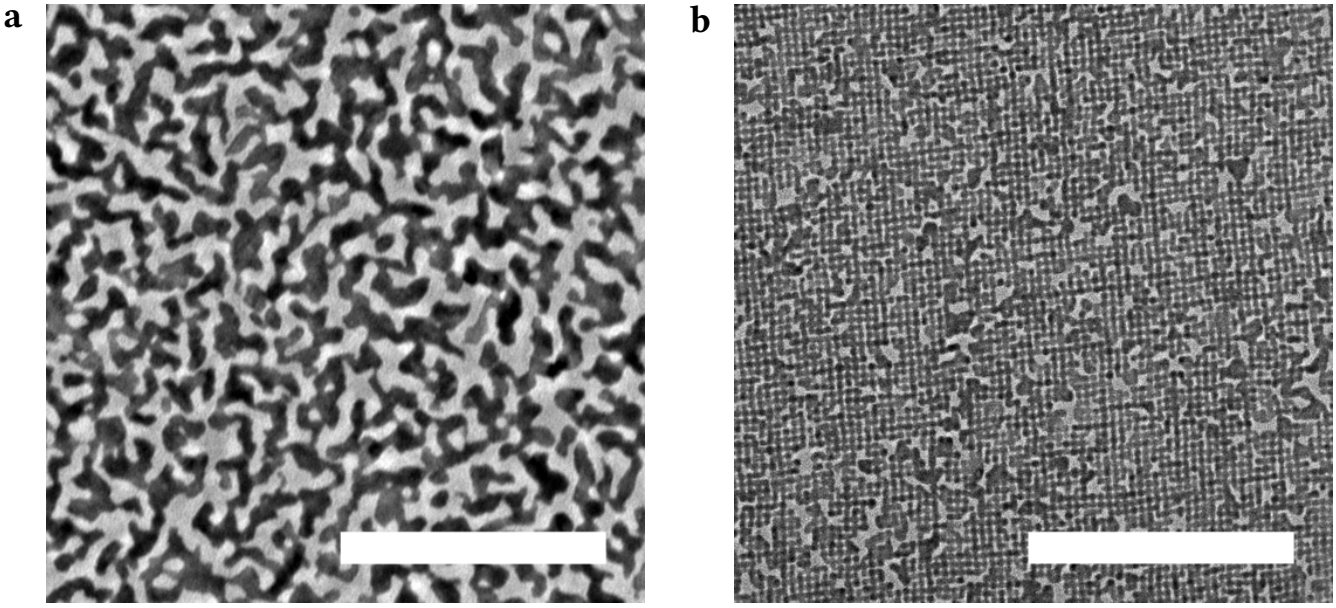

Figure 4.12: TEM images of annealed superlattices, prepared with the new procedure. **(a)** TEM image of a superlattice annealed at 75 °C for 1 hour. The lattice has melted completely and no square ordering can be observed anymore. **(b)** TEM image of a superlattice annealed at 50 °C for 1 hour. Significant melting of the lattice has occurred, although square order has largely been conserved. Scale bars 200 nm.

of the reaction temperature to 15 °C. However, fully-formed square superlattices could only be prepared at 15 °C by increasing the reaction time to 4 hours. Nevertheless, superlattices prepared in this way contained large vacancies and molten structures. A new method, in which the superlattice preparation was split into two phases, was investigated as well. With this method, the NC dispersion was dropcast on an ethylene glycol substrate that was cooled to 15 °C. Subsequently, the temperature was kept at 15 °C for 1 hour in the initial phase. In the second phase the temperature was increased to 23 °C for 90 minutes. Presumably, in the first phase the NCs self-assemble in a monolayer with long-range order after which the square lattice formation is induced in the second phase. Fully-formed square superlattices with a reduced amount of molten structures and domain sizes of $\sim$0.1 - 0.2 μm^2 could be obtained with this method. Hence, for the aged NCs this new preparation method is a significant improvement over the original method. The superlattices prepared with the new method showed a large relative neck thickness of 0.54 ± 0.08 compared to the superlattices presented in Section 4.1.3. This large relative neck thickness was attributed to the difference in the superlattice preparation method and the reduction of the ligand density of the NCs in the dispersion. Unfortunately, the superlattices produced with this new method showed reduced thermal stability compared to the lattices presented in Section 4.1.3. Only molten structures remained after annealing of the lattices at 75 °C, which was previously shown to result in only minor changes to the lattice. The retention of the square superlattice was

improved by annealing at a temperature of 50 °C, although a large amount of molten structures were obtained here as well. The relative neck thickness increased from 0.54 ± 0.08 to 0.60 ± 0.11 by annealing at 50 °C . This relative neck thickness is between the values obtained for the lattices annealed at 100 and 125 °C in Section 4.1.3. The large relative neck thickness after annealing at 50 °C was also attributed to the difference in the preparation of the square superlattice and the reduced ligand density of the NCs in the dispersion. As the superlattices prepared with the new method showed an increase in the square domain size and a reduced number of defects compared to the lattices presented in Section 4.1.4, square PbSe superlattices were prepared with the new method in all further experiments. For the annealing of the superlattice on the other hand, a temperature of 50 °C was used to prevent full melting of the superlattice. In the next sections, the results of cation exchange experiments on the superlattices prepared with the new method are presented.

4.2 Pb-to-Cd cation exchange of square PbSe superlattices

Pb-to-Cd cation exchange reactions were performed on superlattices produced with the new methods outlined in Section 4.1.5. Cation exchange reactions were performed as outlined in Section 3.4. As a starting point, different temperatures and reaction times that are reported in literature were repeated in this work[1, 7]. In these procedures superlattices with a square[1], or a honeycomb[7] geometry were cation exchanged into CdSe superlattices. In addition, cation exchange at a lower temperature was investigated as well. The aim of these experiments was to find a cation exchange procedure with which the square superlattice structure could be conserved as much as possible. A second goal was to find a procedure with which partial exchange could be achieved, as studying a partially exchanged lattice could reveal if exchange is initiated at the necks, the cores, or both simultaneously. Moreover, the study of a partially exchanged lattice could elucidate whether lead atoms that have remained in the lattice are concentrated at the cores or if they are distributed randomly over the lattice. The results of these experiments are discussed in the following sections. We assume that, before the exchange reaction, the cation exchanged samples showed similar structures compared to the PbSe superlattices prepared with the new method presented in Section 4.1.5.

4.2.1 Cation exchange at 150 °C and 175 °C

Initially, a procedure reported by Boneschanscher *et al.* for Pb-to-Cd ion exchange on honeycomb superlattices was repeated[7]. The aim was to investigate whether this method is also appropriate for square superlattices. The cation exchange reaction was performed by heating an excess of $Cd(OA)_2$ in ODE to 150 °C, after which the superlattice on a solid substrate was placed in the solution. After 1 hour, the temperature was increased to 175 °C for another 15 minutes.

A TEM image of a square superlattice exchanged with the method of Boneschanscher *et al.* is shown in Figure 4.13a. Although square ordering can still be observed in this image, the domain sizes reduced to a maximum of $\sim$0.01 μm^2. The cation exchange reaction was also performed on a square lattice that was annealed at 50°C before the exchange reaction. A HAADF-STEM image of this exchanged lattice is given in Figure 4.13b. In this lattice also only small square patches with a maximum size of $\sim$0.01 μm^2 remained and long-range order has been lost. Therefore, annealing of the lattice before cation exchange did not seem to have a beneficial effect on the retention of the long-range order in the lattice. The square lattice structures shown in Figure 4.13a and 4.13b both remained on $\sim$20% of the TEM grid.

As explained in Section 2.5, the lattice mismatch between the PbSe and the expected zincblende CdSe crystal structure is less than 2%[47, 48]. Hence, the cation exchange reaction is expected to have a minimal impact on the neck thickness and NC diameter in the superlattices. To determine whether this is the case, 200 measurements were performed by hand to assess the neck thickness, number of necks per NC and NC diameter of the lattices in Figure 4.13a and 4.13b. The results of these measurements are presented in Table 4.2. In the table, the cation exchanged superlattices are compared to the as-prepared

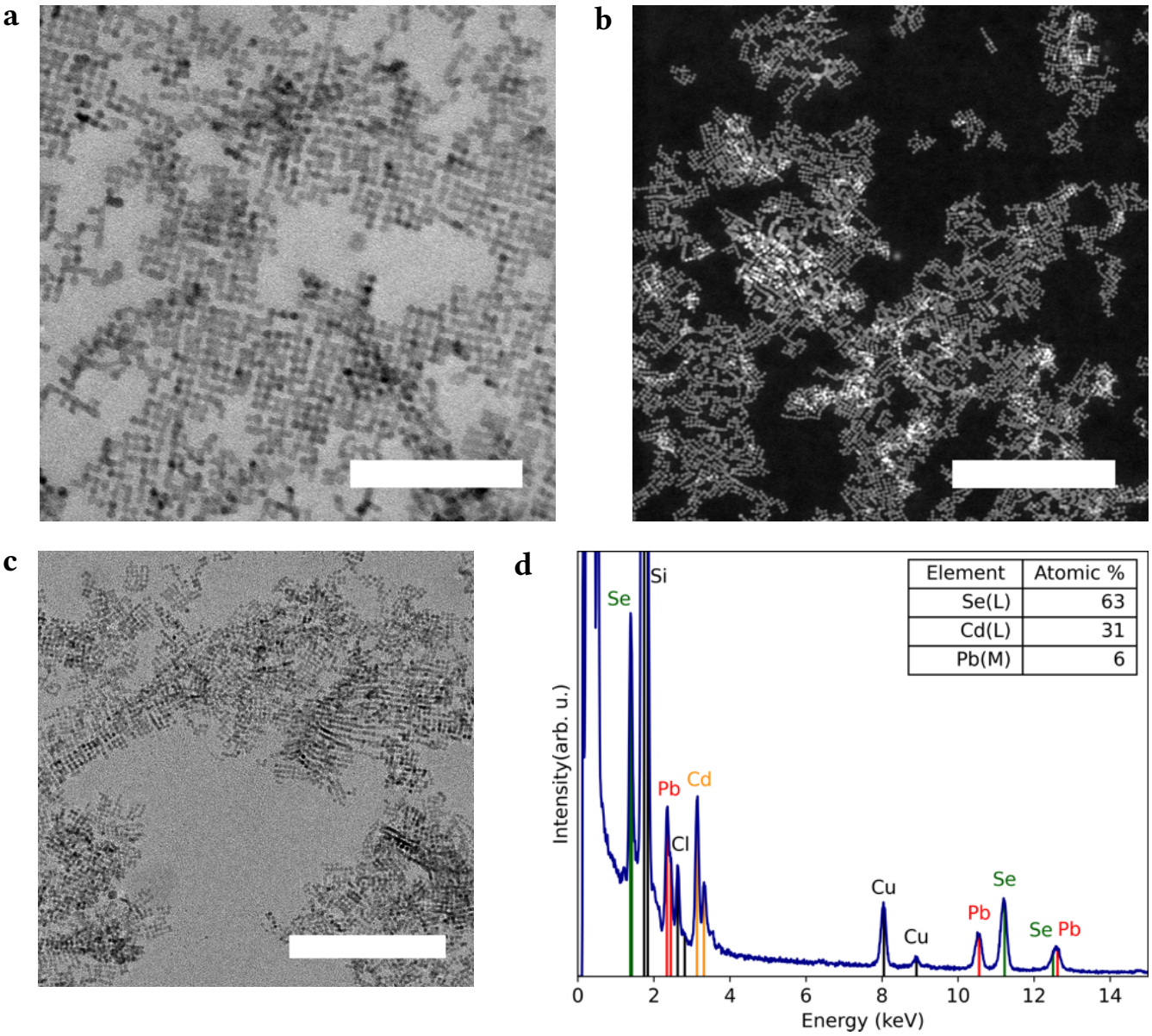

Figure 4.13: TEM and HAADF-STEM images and EDX spectrum of a square superlattice after cation exchange at 150 °C for 1 hour and 175 °C for 15 minutes. **(a)** TEM image of the lattice after the exchange reaction. No initial annealing was performed on the square PbSe lattice before the exchange reaction. Although square structure has remained in this lattice, only small square lattice domains can be observed. Scale bar 100 nm. **(b)** HAADF-STEM image of a lattice that was annealed at 50 °C for 1 hour before the cation exchange reaction was performed. In this sample only small square lattice domains are left as well. Scale bar 250 nm. **(c)** TEM image of a lattice after cation exchange of which an EDX spectrum was taken. No annealing was performed on the lattice before the exchange reaction. Most of the square lattice has been lost after the cation exchange reaction was performed on this sample. Scale bar 200 nm. **(d)** The EDX-spectrum of the TEM image shown in **(c)**. Nearly full exchange has been achieved, based on the quantification of this spectrum.

and annealed lattices prepared with the new method, presented in Section 4.1.5. For the lattice that was not annealed before the exchange reaction, the number of necks per NC and the NC diameter remained approximately the same after the exchange reaction at 2.5 ± 0.8 and 5.6 ± 0.6 nm, respectively. However, the neck thickness increased from 3.1 ± 0.4 to 3.6 ± 0.6 nm. Consequently, the relative neck thickness increased from 0.54 ± 0.08 to 0.64 ± 0.13 after exchange of this superlattice. This indicates that annealing of the superlattice occurred during the cation exchange reaction. For the lattice that was annealed at 50 °C before the cation exchange reaction, the neck thickness remained relatively unchanged at 3.7 ± 0.6 nm. However, for this lattice the number of necks per NC decreased from 3.0 ± 0.8 to 2.2 ± 0.8 and the NC diameter reduced from 6.3 ± 0.6 to 5.6 ± 0.5 nm. As a result, the relative neck thickness of this lattice was increased from 0.60 ± 0.11 to 0.66 ± 0.12. The reduction of the NC diameter and the number of necks per NC indicate that part of the lattice was destroyed and material was lost during the cation exchange reaction.

To determine the amount of exchange that was achieved using this procedure, an EDX spectrum was taken of an exchanged lattice. The area of the lattice on which the EDX measurement was performed is shown in Figure 4.13c. No initial annealing was performed on the lattice in this figure. Although some square ordering can still be observed in this image, no square lattice domains of significant size have remained after the exchange reaction. The EDX spectrum that was taken of this part of the lattice is displayed in Figure 4.13d. Approximately 6% Pb has remained in this area based on the quantification of the spectrum shown in the top right corner of this image. However, the sample shown here was contaminated with organic molecules, as evident from the large number of counts between 0 and 1 keV in the spectrum. Hence, it is possible that the Pb atoms that were left in this area are present as $Pb(OA)_2$ and not as PbSe in the lattice. To determine whether this is the case, the experiment should be repeated with a sample that has been washed for a longer amount of time to reduce the contamination.

Based on the results presented in this section, it can be concluded that performing cation exchange at 150 °C for 1 hour and 175 °C for 15 minutes results in a strong loss of the square domain sizes from $\sim$0.1 - 0.2 μm^2 to $\sim$0.01 μm^2. This loss of the square domain size was recorded for both the lattice that was annealed and the lattice that was not annealed before the exchange reaction. Moreover, after the exchange reaction an increase in the relative neck thickness was calculated for both the annealed and the as-formed lattice. For the lattice that was not annealed before the exchange reaction, this was attributed to annealing of the lattice during cation exchange. On the other hand, the increased relative neck thickness in the lattice that was annealed before the exchange reaction was attributed to the loss of material during the exchange reaction. Hence, although the honeycomb lattices that were cation exchanged with this method retained their long-range order[7], this was not the case for the square superlattices in this work. Nevertheless, based on the EDX spectrum nearly full exchange was achieved with this cation exchange procedure, which is in line with previous research[7]. In view of these results, further exchange reactions were performed at a lower temperature in an effort to improve the retention of long-range order in the square lattices after cation exchange.

4.2.2 Cation exchange at 130 °C

After the initial cation exchange experiments discussed above, exchange reactions were also performed at a lower temperature of 130 °C for 2 hours. In previous work, full Pb-to-Cd cation exchange of a square PbSe superlattice with retention of the overall geometry was achieved under these reaction conditions[1]. Nevertheless, the square ordering in the superlattice had been distorted after the exchange reaction, as more diffuse spots were visible in the electron diffraction pattern of the exchanged lattice. In addition, more vacancies and molten structures could be observed in the lattice[1]. In this work, an attempt was made to reproduce these results and to investigate whether annealing of the superlattices could potentially increase the retention of long-range order. The results of these experiments are presented here.

Cation exchange of as-prepared superlattices

In Figure 4.14a a HAADF-STEM image is shown of a Pb-to-Cd cation exchanged square lattice on which no initial annealing was performed. Square domains with sizes up to $\sim$0.1 μm^2 were observed in this lattice and the square ordering in the lattice has largely been retained. However, the lattice is slightly more disordered compared to the as-prepared lattice shown in Figure 4.11a, as can be deduced from the slightly more diffuse spots in the FFT in Figure 4.14a. The square lattices shown in Figure 4.14a remained on $\sim$20% of the TEM grid. In Figure 4.14b a higher magnification HAADF-STEM image of the same sample is shown. In this image the epitaxial connections between the NCs, as well as molten structures and several unattached NCs can be observed. Unfortunately, the resolution of the electron microscope in HAADF-STEM mode is not sufficient to examine the crystal structure of the cation exchanged lattice. This was also not possible in TEM mode, as is demonstrated in Appendix E.

The neck thickness, average number of necks per NC and the NC diameter in the lattice shown in Figure 4.14a were measured by hand and the average was taken over 200 measurements. The measured values are listed in Table 4.2. In this lattice the neck thickness and NC diameter increased slightly from 3.1 ± 0.4 to 3.6 ± 0.5 nm and from 5.7 ± 0.4 to 5.9 ± 0.7 nm, respectively. Consequently, the relative neck thickness increased as well, from 0.54 ± 0.08 to 0.61 ± 0.11. Moreover, the number of necks per NC decreased slightly from 2.7 ± 0.9 to 2.3 ± 0.8. It can therefore be concluded that although the overall geometry has been retained, several necks were lost and the lattice was annealed slightly during the cation exchange reaction. Nevertheless, the retention of the square lattice has been improved significantly compared to the lattices cation exchanged at 150 °C for 1 hour and 175 °C for 15 minutes, shown in Figure 4.13.

An EDX spectrum was taken of this sample to investigate how much Pb-to-Cd exchange had occurred. The area of the lattice on which the measurement was performed is shown in Figure 4.14c. In this image the square ordering has also largely been retained. The EDX spectrum that was recorded is shown in Figure 4.14d. From the EDX spectrum it follows that 6% Pb has remained in the area of the lattice shown in Figure 4.14c. Hence, similar to the lattice that was exchanged at 150 °C for 1 hour

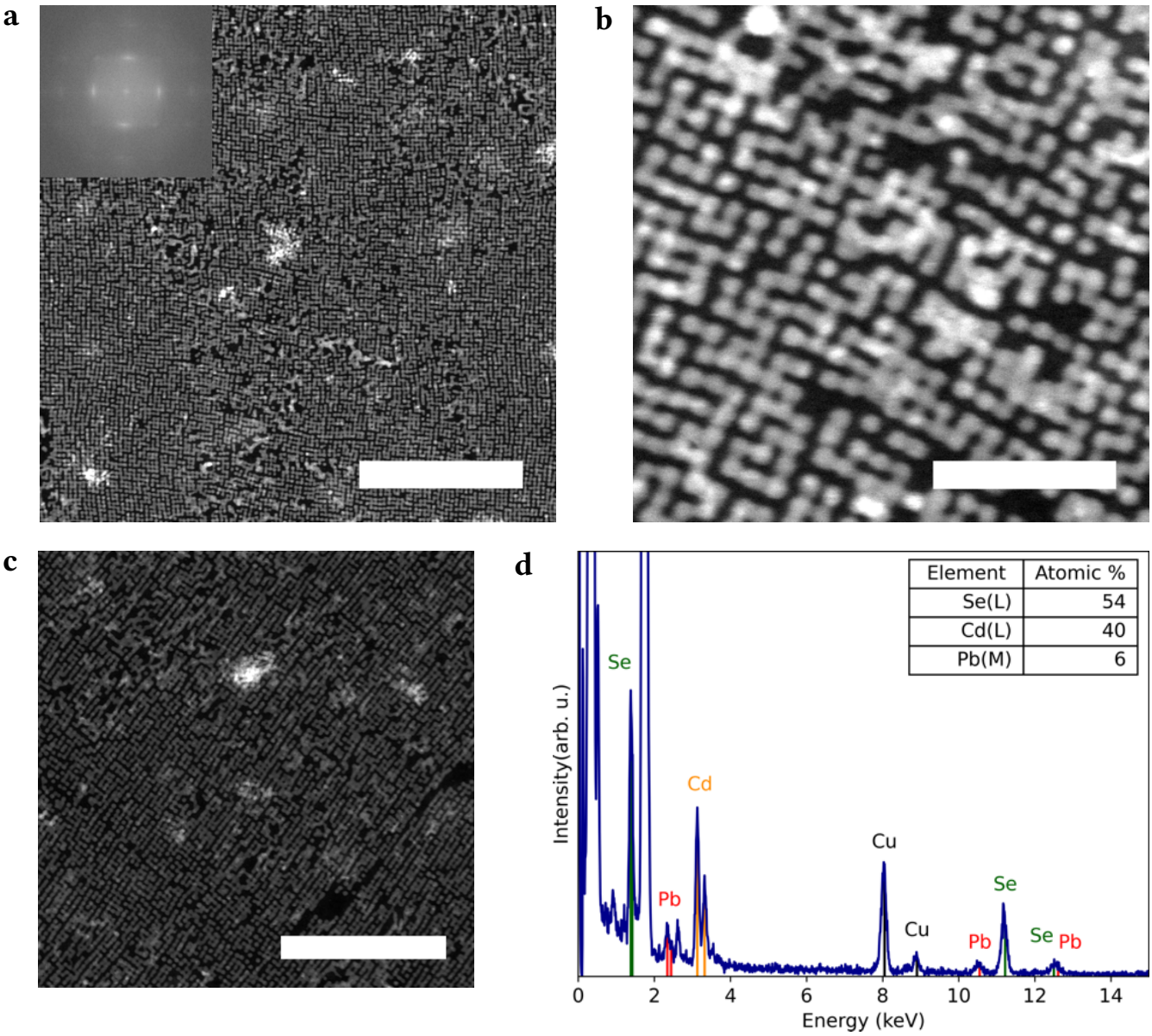

Figure 4.14: HAADF-STEM images and EDX spectrum of a square superlattice after cation exchange at 130 °C for 2 hours. No initial annealing was performed on the lattice. **(a)** HAADF-STEM image showing that the square ordering in the lattice has largely been retained. This is also evident from the FFT of the image, shown in the top left corner. Scale bar 250 nm. **(b)** Higher magnification HAADF-STEM image showing the epitaxial connections between the NCs have remained intact after the exchange reaction. **(c)** HAADF-STEM image of the area on which the EDX measurement was performed. Scale bar 200 nm. **(d)** EDX spectrum of the area of the superlattice shown in **(c)**. Nearly full exchange has been achieved under these reaction conditions as well.

and 175 °C for 15 minutes, nearly full exchange was achieved with this procedure as well. Some contamination with organic molecules was also present in this sample. Therefore, for this sample it is also possible that Pb has remained in the sample as $Pb(OA)_2$ and not as PbSe in the lattice.

Cation exchange of annealed superlattices

The cation exchange reaction was also performed on square lattices that were annealed at 50 °C for 1 hour before the exchange reaction. A HAADF-STEM image of such a lattice after cation exchange is shown in Figure 4.15a. A large number of unattached NCs can be observed in this HAADF-STEM image and no significantly large square domains appear to have remained after exchange. In Figure 4.15b a HAADF-STEM image at a higher magnification is shown. Square ordering of the NCs as well as many unattached NCs can be observed in this image. The sizes of these square domains were $\sim$0.01 μm^2.

The neck thickness, number of necks per NC and NC diameter of the lattice in Figure 4.15b were determined by performing 200 measurements by hand. The averages of these measurements are displayed in Table 4.2. The neck thickness in this lattice decreased from 3.8 ± 0.6 to 2.9 ± 0.6, while the

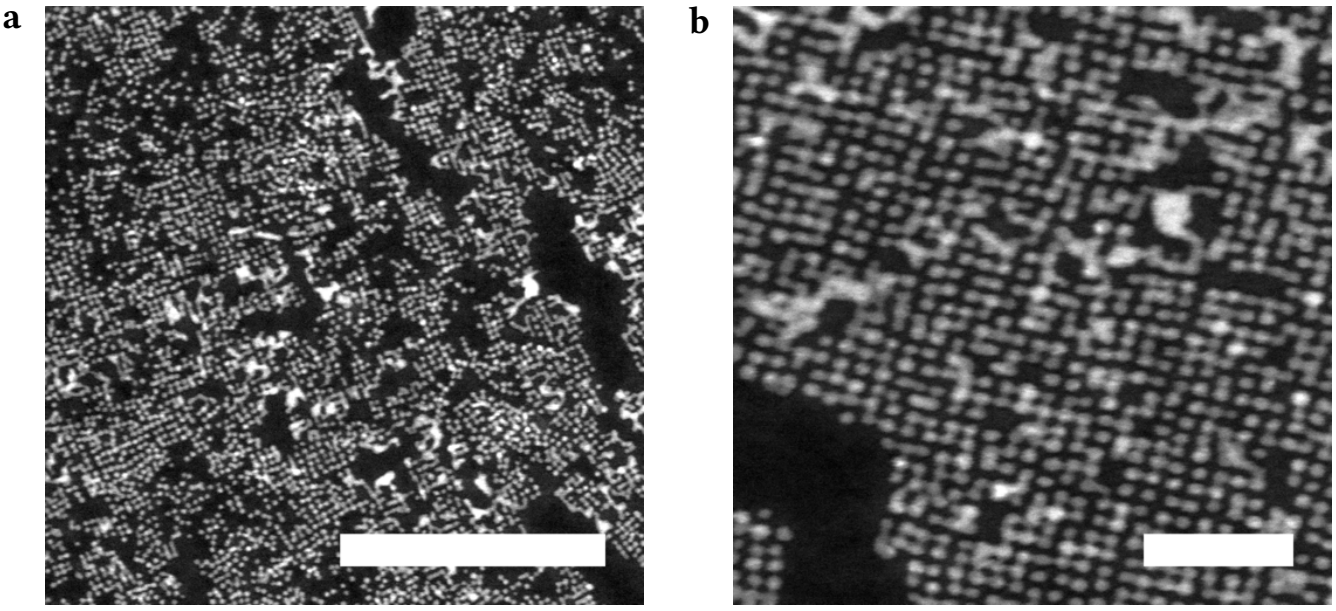

Figure 4.15: HAADF-STEM images of a square lattice after cation exchange at 130 °C for 2 hours. The lattices were annealed at 50 °C for 1 hour before the exchange reaction. **(a)** HAADF-STEM image showing less remaining square lattice after the exchange reaction compared to the lattice that was not annealed before exchange. Many epitaxial connections appear to have been lost and unattached NCs can be observed at several places in the image. Scale bar 250 nm. **(b)** Higher magnification HAADF-STEM image of the same sample. Many epitaxial connections in the lattice appear to have been lost after the cation exchange reaction. Scale bar 50 nm.

number of necks per NC decreased strongly from 3.0 ± 0.8 to 1.8 ± 0.9. In addition, the NC diameter decreased from 6.3 ± 0.6 to 5.0 ± 0.7 nm. Based on these measurements, the relative neck thickness of this lattice decreased slightly from 0.60 ± 0.11 to 0.58 ± 0.14 after exchange of the annealed lattice. These results imply that a large amount of material was lost during the exchange reaction. Hence, contrary to what was expected, lattices that had been annealed before the cation exchange reaction showed less long-range order compared to the lattices that were not annealed before exchange. As demonstrated in Section 4.1.5, square PbSe lattices already showed reduced long-range order after the annealing step was performed. It is possible that this reduction in long-range order caused by annealing of the PbSe superlattice influences the retention of the long-range order during cation exchange reaction. Further experiments with lattices that do not show molten structures in the lattice after annealing are required to determine whether this is the case.

In conclusion, after performing the cation exchange reaction at 130 °C for 2 hours on as-prepared PbSe superlattices, nearly full exchange with retention of the overall lattice geometry was achieved. At the same time, a slight increase in disorder was observed in the exchanged lattices. Hence, the results of Evers *et al.* could be reproduced for the lattices that were not annealed before the exchange reaction[1]. Unfortunately, it was not possible to determine the crystal structure from high magnification HAADF-STEM or TEM images of the exchanged superlattice. The crystal structure should therefore be determined on higher resolution electron microscopes which were not available in this work. It is evident from the results presented here that performing the cation exchange reaction at 130 °C for 2 hours results in exchanged lattices with significantly improved long-range order compared to the lattices that were exchanged at 150 °C for 1 hour and 175 °C for 15 minutes. Furthermore, it can be concluded that annealing does not necessarily increase the robustness of the necks in the square superlattices for subsequent cation exchange reactions. In additional experiments cation exchange was performed at a lower reaction temperature to investigate if the retention of the square superlattice structure could be enhanced further. The results of these experiments are discussed in the next section.

4.2.3 Cation exchange at 100 °C

In the previous section it was shown that lowering the reaction temperature during cation exchange has a favourable effect on retention of the square superlattice structure. Therefore, the cation exchange reaction was performed at a lower temperature of 100 °C for 2 hours in further experiments. The goal was to increase the retention of the long-range order in the superlattices even more. In addition, the amount of Pb-to-Cd exchange in these lattices is investigated. The results of these experiments are presented in this section.

Cation exchange of as-prepared superlattices

Figure 4.16a shows a HAADF-STEM image of a lattice on which cation exchange was performed at 100 °C for 2 hours. No initial annealing was performed on this superlattice before the exchange reaction. As

can be seen in this HAADF-STEM image, the long-range order is largely retained, while molten structures can be observed at the grain boundaries of the superlattice as well. Several differently oriented square domains are present in this image, which makes analysis of the disorder by the FFT of the image difficult. Consequently, the FFT was not added to this image. The square superlattices with domain sizes of ∼0.1 - 0.2 μm^2 remained on ∼20% of the TEM grid. A higher magnification HAADF-STEM image of the lattice is shown in Figure 4.16b. As can be seen from this image, many epitaxial connections between the NCs have been retained and no unattached NCs can be observed. Moreover, no molten structures are present in the square domain that is visible here.

The neck thickness, number of necks per NC and NC diameter in the lattice displayed in Figure 4.16b were measured by hand and averaged over 200 measurements. The results of these measurements are listed in Table 4.2. The neck thickness, number of necks per NC and NC diameter of 3.2 ± 0.5 nm, 2.8 ± 0.8 and 5.7 ± 0.5 nm in this lattice all remained approximately the same compared to the lattice before cation exchange. These results suggest that cation exchange at 100 °C for 2 hours results in only minor changes to the square superlattice structure.

An EDX spectrum was taken of the sample to determine the amount of exchange that had occurred. A HAADF-STEM image of the area of the lattice on which the measurement was performed is shown in Figure 4.16c. The lattice that is visible in this image also shows good retention of the long-range order. The EDX spectrum that was taken of this area is shown in Figure 4.16d. From the quantification of this EDX spectrum it follows that 11% Pb remained in this area of the sample. Similar as before, it is possible that Pb has remained as contamination as $Pb(OA)_2$ and not as PbSe in the lattice. Nevertheless, assuming that Pb has indeed remained in the lattice as PbSe, 76% Pb-to-Cd exchange has taken place based on the quantification of the EDX spectrum. This indicates that partial Pb-to-Cd cation exchange was achieved.

In previous work reported in literature, Pb-to-Cd cation exchange of PbSe NCs at a reaction temperature of 100 °C was investigated as well. However, in this work, a maximum of 44% exchange was reported for nanorods with a diameter of 6 ± 0.6 nm[44]. Despite increasing the reaction time up to 12 hours in the work reported in literature, further exchange was not possible for these NCs[44]. Hence, the 76% Pb-to-Cd exchange obtained for the superlattices shown in Figure 4.16 is in contrast with this previously reported work. As the NCs in the superlattice have a diameter of 5.7 ± 0.4 nm, the difference in the diameter between the nanorods reported in literature and the NCs in the superlattice is only small. Therefore the difference in the reaction conditions is more likely to be the cause of the discrepancy. The exchange reaction in this work is performed with a Pb:Cd ratio on the order of $1 : 10^8$, based on 2 mL of a 0.1 mol$*$$L^{-1}$ $Cd(OA)_2$ solution and a SiN grid of 1.0 mm x 1.0 mm fully covered by a monolayer of the PbSe superlattice. On the other hand, in the work reported in literature a Pb:Cd ratio between 1:20 and 1:50 was used[44]. Hence, it is possible that the larger amount of exchange in the superlattices is caused by the fact that the excess in this work was 7 orders of magnitude higher.

An attempt was made to construct an elemental map of the partially exchanged lattice. Unfortunately, the lattice melted during the mapping procedure before the elemental mapping was completed,

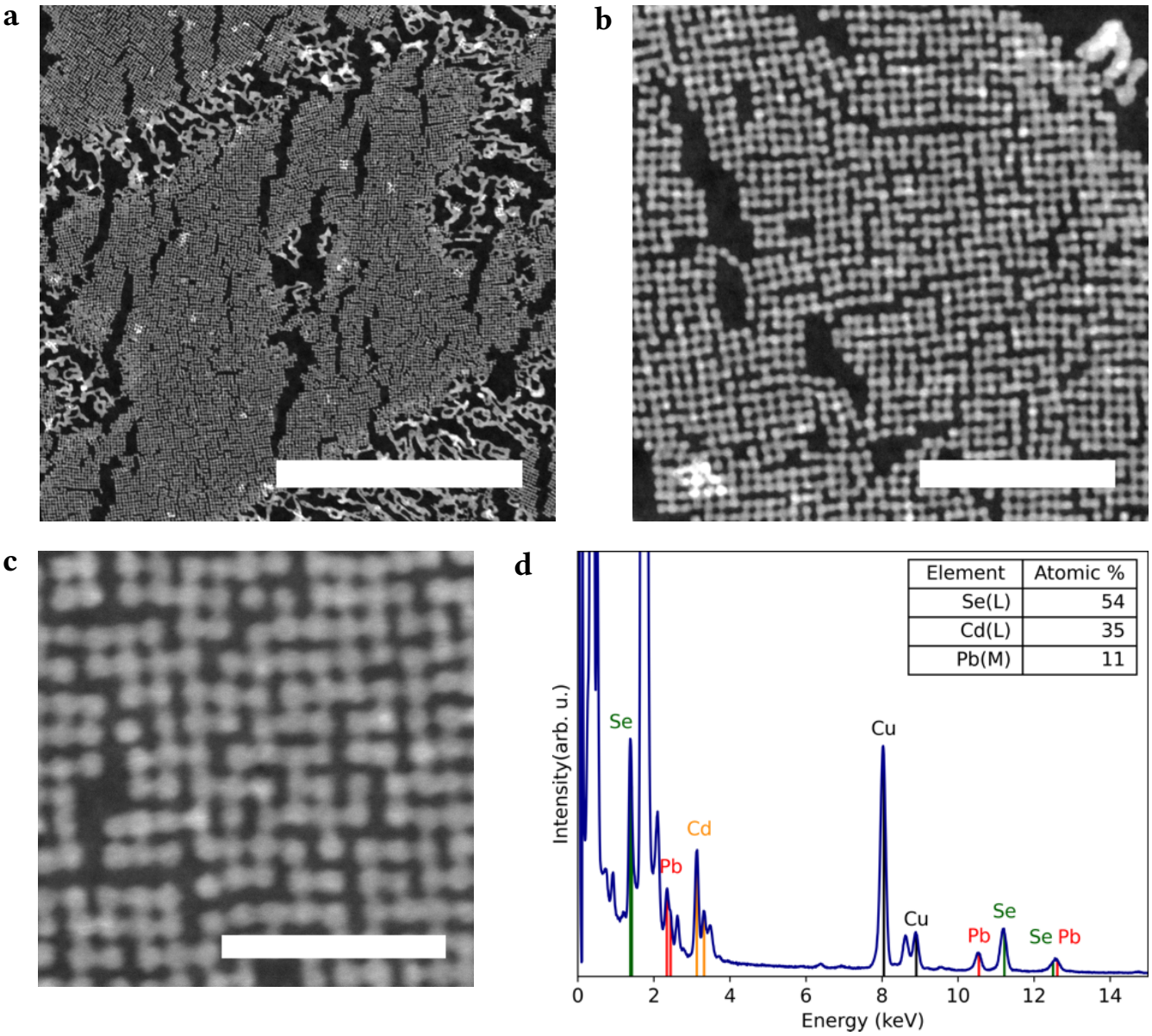

Figure 4.16: HAADF-STEM images and EDX spectrum of a square superlattice after cation exchange at 100 °C for 2 hours. No initial annealing was performed on the lattice. **(a)** HAADF-STEM image showing that large square superlattice domains have remained after the exchange reaction. Molten structures can be observed at the edge of these domains. Scale bar 500 nm. **(b)** Higher magnification HAADF-STEM image of the exchanged lattice. Many of the epitaxial connections between the NCs have remained after the exchange reaction. Scale bar 100 nm. **(c)** HAADF-STEM image of the area of the lattice on which the EDX measurements was performed. In this area, the square lattice structure has been largely retained. Scale bar 50 nm. **(d)** EDX spectrum of the area of the lattice shown in **(c)**. Based on the quantification of the EDX spectrum, partial exchange has been achieved.

as shown in Appendix F. Hence, no accurate conclusions regarding the position of the Pb atoms in the lattice can be drawn based on the obtained elemental map. As shown in Section 4.1.5, the superlattices made from the aged NCs showed reduced thermal stability compared to the superlattices prepared with pristine NCs. Therefore, it can be assumed that these lattices also show reduced stability during elemental mapping. Possibly, elemental mapping could be performed successfully on partially exchanged superlattices if the original square PbSe superlattice is prepared with PbSe NCs from a fresh batch.

Cation exchange of annealed superlattices

The cation exchange reaction was also performed on lattices that were annealed at 50 °C for 1 hour before the exchange reaction. A HAADF-STEM image of a square lattice that was produced in this way is shown in Figure 4.17a. Square ordering can be observed in the lattice shown in this HAADF-STEM image. Molten structures can also be observed at the borders of the square domains, but not in the square domains themselves, similar to the lattices that were not annealed before cation exchange shown in Figure 4.16. The square lattice domains remained on ∼20% of the TEM grid and were typically ∼0.1 μm^2 in size. In addition, no unattached NCs can be observed inside of the square domains in the higher magnification HAADF-STEM image of the sample shown in Figure 4.17b.

The neck thickness, number of necks per NC and NC diameter in the lattice shown in Figure 4.17a were measured by hand. The averages of 200 measurements are presented in Table 4.2. The neck thickness remained approximately the same after exchange, at 3.7 ± 0.6 nm. However, the number of necks per NC and NC diameter decreased slightly from 3.0 ± 0.8 to 2.6 ± 0.8 and from 6.3 ± 0.6 to 5.9 ± 0.6 nm, respectively. Consequently, the relative neck thickness increased slightly from 0.60 ± 0.11 to 0.63 ± 0.12 after cation exchange of the annealed lattice at 100 °C for 2 hours. From these results it can be concluded that the square superlattice structure was largely retained, although some material was lost during the exchange reaction. Hence, performing the exchange reaction at 100 °C for 2 hours was also beneficial for retention of long-range order for the lattice that was annealed before the exchange reaction. In addition, no unattached NCs can be observed inside of the square domains in the higher magnification HAADF-STEM image of the sample shown in Figure 4.17b. This is in contrast with the results that were obtained for the annealed lattice that was cation exchanged at 130 °C for 2 hours, where many unattached NCs could be observed.

In summary, the lattices obtained after cation exchange at 100 °C for 2 hours showed larger square domain sizes of ∼0.1 - 0.2 μm^2 compared to the lattices that were obtained after exchange at 150 and 175 °C and the lattices exchanged at 130 °C. In addition, the neck thickness, number of necks per NC and the NC diameter in the lattices that were cation exchanged at 100 °C were nearly identical to those of a lattice that was not cation exchanged. Partial cation exchange was achieved after exchange under these reaction conditions, with an estimated Pb-to-Cd exchange of 76%. In light of these results, the cation exchange reaction should be performed at this temperature for a longer duration to investigate whether full exchange with the enhanced retention of the square lattice could be achieved as well.

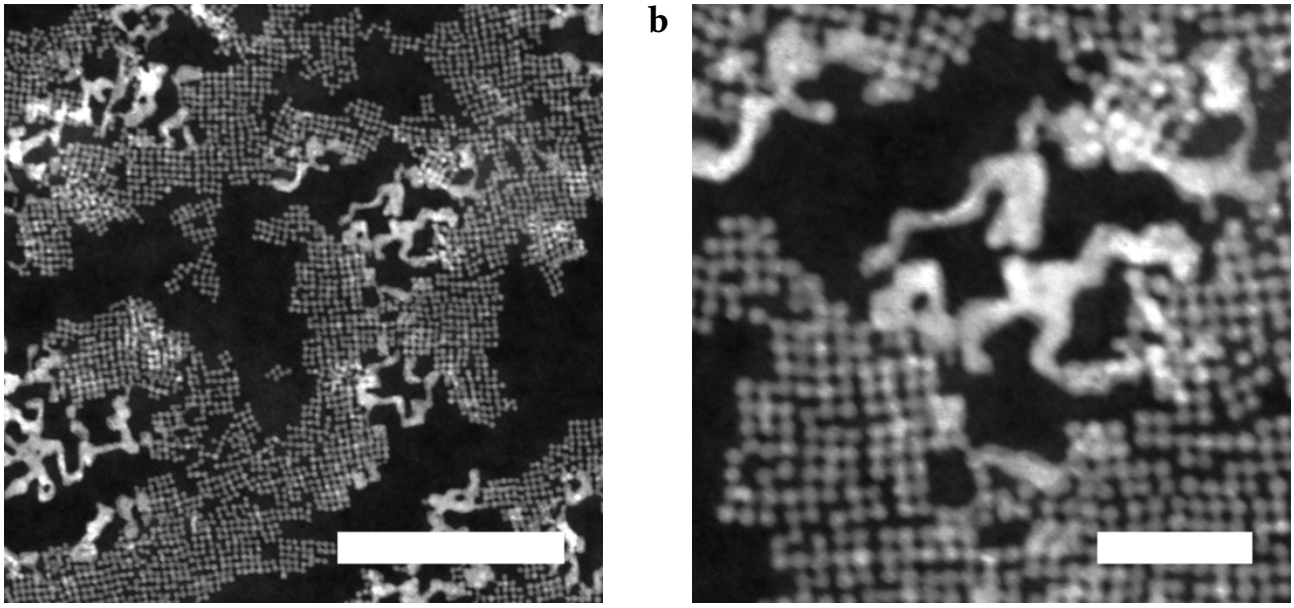

Figure 4.17: HAADF-STEM images of a square lattice after cation exchange at 100 °C for 2 hours. The lattices were annealed at 50 °C for 1 hour before the exchange reaction. **(a)** HAADF-STEM image showing that the square lattice has largely been retained, although square domain sizes have decreased compared to the lattice that was not annealed. Scale bar 250 nm. **(b)** Higher magnification HAADF-STEM image of the same sample, where the epitaxial connections between the NCs remain visible. Scale bar 50 nm.

In an attempt to determine where the Pb atoms remained in the lattice, an elemental map was made. However, the lattice melted before an elemental map could be obtained succesfully. It is conceivable that the lattice melted more easily due to the reduction of the thermal stability of the superlattices prepared with aged NCs. These experiments should therefore be repeated on superlattices made of a fresh batch of PbSe NCs with greater thermal stability. For lattices that were annealed before the cation exchange reaction, smaller domains of $\sim$0.1 μm^2 were obtained. Moreover, a reduction of the number of necks per NC and the NC diameter were measured for the lattices that were annealed before cation exchange was performed. Hence, similar to the lattices that were exchanged at 130 °C, annealing of the superlattices before cation exchange at 100 °C has an adverse effect on the retention of the square superlattice structure. The cause of the reduced retention of the square superlattice structure could not be determined in this work and warrants further research.

Table 4.2: The average neck thickness, number of necks per NC, NC diameter, relative neck thickness and domain size of the square superlattices after cation exchange of the superlattice. For all annealed samples, annealing was performed at 50 °C for 1 hour. All averages were determined by performing 200 measurements by hand using ImageJ software.

Cation exchange reaction conditions	Neck thickness (L)	Number of necks per NC	NC diameter (D)	Relative neck thickness (L/D)	Domain size
No exchange, not annealed	3.1 ± 0.4 nm	2.7 ± 0.9	5.7 ± 0.4 nm	0.54 ± 0.08	∼0.1 - 0.2 μm^2
No exchange, annealed	3.8 ± 0.6 nm	3.0 ± 0.8	6.3 ± 0.6 nm	0.60 ± 0.11	∼0.1 - 0.2 μm^2
150 °C 1h, 175 °C 15 min, not annealed	3.6 ± 0.6 nm	2.5 ± 0.8	5.6 ± 0.6 nm	0.64 ± 0.13	∼0.01 μm^2
150 °C 1h, 175 °C 15 min, annealed	3.7 ± 0.6 nm	2.2 ± 0.8	5.6 ± 0.5 nm	0.66 ± 0.12	∼0.01 μm^2
130 °C 2h, not annealed	3.6 ± 0.5 nm	2.3 ± 0.8	5.9 ± 0.7 nm	0.61 ± 0.11	∼0.1 μm^2
130 °C 2h, annealed	2.9 ± 0.6 nm	1.8 ± 0.9	5.0 ± 0.7 nm	0.58 ± 0.14	∼0.01 μm^2
100 °C 2h, not annealed	3.2 ± 0.5 nm	2.8 ± 0.8	5.7 ± 0.5 nm	0.56 ± 0.10	∼0.1 - 0.2 μm^2
100 °C 2h, annealed	3.7 ± 0.6 nm	2.6 ± 0.8	5.9 ± 0.6 nm	0.63 ± 0.12	∼0.1 μm^2

5 Conclusion and Outlook

Square superlattices showing long-range order were produced by the oriented attachment of PbSe NCs. The neck thickness in these superlattices was increased from 2.6 ± 0.3 up to 3.7 ± 0.5 nm by gentle annealing of the superlattice at temperatures of 75 - 125 °C for 1 hour. This constitutes an increase in the relative neck thickness from 0.48 ± 0.07 up to 0.69 ± 0.11. These results are in contrast with previous research, where the relative neck thickness only increased after annealing at temperatures of 125 - 150 °C for 1 hour. Moreover, in this previous research the variance in the relative neck thickness decreased after annealing, while the variance increased after annealing in this work[35]. This discrepancy was attributed to differences in the superlattice preparation and annealing methods.

It was shown that over time the reproducibility of the superlattice preparation and annealing decreased drastically. From FTIR spectra it was inferred that ligands had desorbed from the surface of the NCs in the dispersion over time. This could be the cause of more rapid oriented attachment, leading to the formation of the observed molten structures and smaller superlattice domains. However, the FTIR spectrum that was taken at a later time contained some noise and a slope. The measurement should therefore be repeated to obtain a cleaner spectrum, so that this conclusion can be drawn with more certainty.

It was demonstrated that oriented attachment can be slowed significantly by producing superlattices at 15 °C. Superlattices prepared at this temperature for 90 or 180 minutes showed domains with bond angles corresponding to a mix between the pseudo-hexagonal and square phase. In a previous study, it was shown that square lattices form through phase transitions of a self-assembled monolayer of PbSe NCs[17]. Hence, the obtained single crystalline domains with pseudo-hexagonal to square ordering lend further credence to the mechanism demonstrated in this study.

Superlattices with long-range order were produced with the aged NCs in two steps. First, oriented attachment was slowed down by keeping the temperature at 15 °C for 1 hour. In the second step the temperature was increased to 23 °C for 90 minutes to induce oriented attachment of the self-assembled NCs. For the aged NCs, domains with significantly increased long-range order were obtained with this method. Nevertheless, the lattices showed reduced thermal stability and annealing at a lower temperature of 50 °C was required to prevent full melting of the lattice.

Cation exchange reactions were performed on superlattices prepared with the new preparation method. Significantly improved retention of long-range order was demonstrated for superlattices cation exchanged at 100 °C for 2 hours. (Nearly) full and partial transformation to CdSe were achieved by performing the exchange reaction at 130 and 100 °C, respectively, both for the duration of 2 hours. Annealing of the PbSe superlattices at 50 °C for 1 hour before transformation into CdSe resulted in a greater loss of long-range order with all cation exchange reactions investigated in this work. Hence,

annealing of the superlattices did not improve the stability of the superlattice during cation exchange. It is possible that the partial melting of the PbSe superlattice during annealing influenced the retention of long-range order after transformation into CdSe. Square PbSe superlattices prepared with pristine NCs did not show these molten structures. In further studies, the effect of annealing on the retention of the square superlattice structure should therefore be studied in PbSe lattices prepared with newly synthesised NCs.

The methods presented in this work allow the Pb-to-Cd exchange of square PbSe lattices with greater retention of the long-range order. The as-prepared lattices cation exchanged at 130 °C for 2 hours are suitable for the investigation of the CdSe crystal structure. This was not possible with the electron microscopes available in this work and should be done using electron microscopes with which higher resolutions can be achieved. Moreover, the as-prepared lattices cation exchanged at 100 °C for 2 hours were only partially transformed into CdSe. These superlattices are therefore well-suited for the investigation of the location of onset of the cation exchange reaction. To study this, we attempted to perform elemental mapping on these partially exchanged lattices, but this resulted in rapid melting of the lattice. This is in contrast with previous work, where CdSe superlattices suffered less from beam damage[7]. Possibly, the CdSe superlattice presented in this work showed the same reduced thermal stability as the as-formed square PbSe lattice. This could have resulted in the more rapid melting observed here. Greater thermal stability was demonstrated for the lattices prepared with pristine PbSe NCs. In future work square superlattices prepared with newly synthesised NCs should therefore be cation exchanged at 100 °C for 2 hours. It is possible that square CdSe lattices with greater stability under an electron beam can be obtained in this way, which would allow the elemental mapping of the partially cation exchanged lattice.

A greater retention of the square superlattice structure, but only partial transformation into CdSe were achieved after cation exchange at 100 °C for 2 hours. In future work, full Pb-to-Cd exchange should therefore be attempted at 100 °C by increasing the reaction time. Moreover, cation exchange at lower temperatures should be investigated. If exchange is still possible at lower temperatures, possibly the square superlattice structure is retained to an even greater extent. Hence, these efforts could improve the retention of the square superlattice structure in fully and partially Pb-to-Cd cation exchanged square superlattices even further.

Acknowledgements

First of all, I would like to thank my supervisor Daniel Vanmaekelbergh for allowing me to do my master thesis in his group. Furthermore, our discussion of my results was a great help to determine the most interesting outcomes of my research project. A big thanks to my daily supervisor Maaike as well for all your guidance, kindness and insights into various Netflix series during my research project! I would like to thank Bas for taking the HAADF-STEM images and EDX spectra and for helping me analyse these images and spectra. Also many thanks to Serena for sending me the EDX data that I needed one day before the university closed due to coronavirus countermeasures!

Next, I would like to thank my fellow master students for providing such a nice atmosphere during my research project. I would like to thank Katerina, Nicolette, Konstantina, Huygen, Jelmer, Philipp and Rian in particular. I had a great time declaring our own country, learning Greek and drinking fancy double espressos. Finally, I would like to thank my girlfriend Danielle, who had to deal with me writing my thesis during the coronavirus lockdown and still managed to cheer me up when I was stressed.

Despite the unconventional ending of my research project due to the coronavirus pandemic, it has been a great year!

References

1. Evers, W. H. *et al.* Low-dimensional semiconductor superlattices formed by geometric control over nanocrystal attachment. *Nano letters* **13,** 2317–2323 (2013).
2. Kalesaki, E., Evers, W., Allan, G., Vanmaekelbergh, D. & Delerue, C. Electronic structure of atomically coherent square semiconductor superlattices with dimensionality below two. *Physical Review B* **88,** 115431 (2013).
3. Kalesaki, E. *et al.* Dirac cones, topological edge states, and nontrivial flat bands in two-dimensional semiconductors with a honeycomb nanogeometry. *Physical review x* **4,** 011010 (2014).
4. Evers, W. H. *et al.* High charge mobility in two-dimensional percolative networks of PbSe quantum dots connected by atomic bonds. *Nature communications* **6,** 1–8 (2015).
5. Van Overbeek, C. *et al.* Interfacial self-assembly and oriented attachment in the family of PbX (X= S, Se, Te) nanocrystals. *The Journal of Physical Chemistry C* **122,** 12464–12473 (2018).
6. Alimoradi Jazi, M. *Superlattices in charge Band occupation and electron transport in 2D PbSe and CdSe superlattices* PhD thesis (Utrecht University, 2019), 90–92.
7. Boneschanscher, M. P. *et al.* Long-range orientation and atomic attachment of nanocrystals in 2D honeycomb superlattices. *Science* **344,** 1377–1380 (2014).
8. Koole, R., Groeneveld, E., Vanmaekelbergh, D., Meijerink, A. & de Mello Donegá, C. *Size Effects on Semiconductor Nanoparticles* in *Nanoparticles: workhorses of nanoscience* (ed de Mello Donegá, C.) 15–23 (Springer, 2014).
9. Hook, J. R. & Hall, H. E. *Waves in crystals* in *Solid state physics* Second, 330 (John Wiley & Sons, 2013).
10. Griffiths, D. J. & Schroeter, D. F. *Identical particles* in *Introduction to quantum mechanics* Second, 224–229 (Cambridge University Press, 2018).
11. Griffiths, D. J. & Schroeter, D. F. *Quantum mechanics in three dimensions* in *Introduction to quantum mechanics* Second, 131–157 (Cambridge University Press, 2018).
12. Banin, U., Cao, Y., Katz, D. & Millo, O. Identification of atomic-like electronic states in indium arsenide nanocrystal quantum dots. *Nature* **400,** 542–544 (1999).
13. Cui, J. *et al.* Colloidal quantum dot molecules manifesting quantum coupling at room temperature. *Nature Communications* **10,** 1–10 (2019).

14. Panfil, Y. E., Shamalia, D., Cui, J., Koley, S. & Banin, U. Electronic coupling in colloidal quantum dot molecules; the case of CdSe/CdS core/shell homodimers. *The Journal of Chemical Physics* **151,** 224501 (2019).

15. Walravens, W. *et al.* Chemically triggered formation of two-dimensional epitaxial quantum dot superlattices. *ACS nano* **10,** 6861–6870 (2016).

16. Tadjine, A. & Delerue, C. Colloidal nanocrystals as LEGO® bricks for building electronic band structure models. *Physical Chemistry Chemical Physics* **20,** 8177–8184 (2018).

17. Geuchies, J. J. *et al.* In situ study of the formation mechanism of two-dimensional superlattices from PbSe nanocrystals. *Nature materials* **15,** 1248–1254 (2016).

18. Alimoradi Jazi, M. *et al.* Transport properties of a two-dimensional PbSe square superstructure in an electrolyte-gated transistor. *Nano letters* **17,** 5238–5243 (2017).

19. Peters, J. L. *et al.* Mono-and multilayer silicene-type honeycomb lattices by oriented attachment of PbSe nanocrystals: synthesis, structural characterization, and analysis of the disorder. *Chemistry of materials* **30,** 4831–4837 (2018).

20. Murray, C. B. *et al.* Colloidal synthesis of nanocrystals and nanocrystal superlattices. *IBM Journal of Research and Development* **45,** 47–56 (2001).

21. Steckel, J. S., Yen, B. K., Oertel, D. C. & Bawendi, M. G. On the mechanism of lead chalcogenide nanocrystal formation. *Journal of the American Chemical Society* **128,** 13032–13033 (2006).

22. Campos, M. P. *et al.* A library of selenourea precursors to PbSe nanocrystals with size distributions near the homogeneous limit. *Journal of the American Chemical Society* **139,** 2296–2305 (2017).

23. Sowers, K. L., Swartz, B. & Krauss, T. D. Chemical mechanisms of semiconductor nanocrystal synthesis. *Chemistry of Materials* **25,** 1351–1362 (2013).

24. Moreels, I. *et al.* Composition and size-dependent extinction coefficient of colloidal PbSe quantum dots. *Chemistry of Materials* **19,** 6101–6106 (2007).

25. Peters, J. L. *et al.* Ligand-Induced Shape Transformation of PbSe Nanocrystals. *Chemistry of Materials* **29,** 4122–4128 (2017).

26. Fang, C., van Huis, M. A., Vanmaekelbergh, D. & Zandbergen, H. W. Energetics of polar and nonpolar facets of PbSe nanocrystals from theory and experiment. *ACS nano* **4,** 211–218 (2010).

27. Boles, M. A., Engel, M. & Talapin, D. V. Self-assembly of colloidal nanocrystals: From intricate structures to functional materials. *Chemical reviews* **116,** 11220–11289 (2016).

28. Vincent, B., Edwards, J., Emmett, S. & Jones, A. Depletion flocculation in dispersions of sterically-stabilised particles ("soft spheres"). *Colloids and Surfaces* **18,** 261–281 (1986).

29. Evers, W. H. *et al.* Entropy-driven formation of binary semiconductor-nanocrystal superlattices. *Nano letters* **10,** 4235–4241 (2010).

30. Eldridge, M., Madden, P. & Frenkel, D. Entropy-driven formation of a superlattice in a hard-sphere binary mixture. *Nature* **365,** 35–37 (1993).

31. Bolhuis, P. G., Frenkel, D., Mau, S.-C. & Huse, D. A. Entropy difference between crystal phases. *Nature* **388,** 235–236 (1997).

32. Frenkel, D. Entropy-driven phase transitions. *Physica A: statistical mechanics and its applications* **263,** 26–38 (1999).

33. Wang, Y. *et al.* Dynamic deformability of individual PbSe nanocrystals during superlattice phase transitions. *Science advances* **5,** eaaw5623 (2019).

34. Wang, Y. *et al.* In situ TEM observation of neck formation during oriented attachment of PbSe nanocrystals. *Nano Research* **12,** 2549–2553 (2019).

35. Walravens, W. *et al.* Setting carriers free: healing faulty interfaces promotes delocalization and transport in nanocrystal solids. *ACS nano* **13,** 12774–12786 (2019).

36. Wolcott, A. *et al.* Anomalously large polarization effect responsible for excitonic red shifts in PbSe quantum dot solids. *The journal of physical chemistry letters* **2,** 795–800 (2011).

37. Döllefeld, H., Weller, H. & Eychmüller, A. Particle- Particle Interactions in Semiconductor Nanocrystal Assemblies. *Nano letters* **1,** 267–269 (2001).

38. Ondry, J. C., Philbin, J. P., Lostica, M., Rabani, E. & Alivisatos, A. P. Resilient Pathways to Atomic Attachment of Quantum Dot Dimers and Artificial Solids from Faceted CdSe Quantum Dot Building Blocks. *ACS nano* **13,** 12322–12344 (2019).

39. Pradhan, N., Xu, H. & Peng, X. Colloidal CdSe quantum wires by oriented attachment. *Nano letters* **6,** 720–724 (2006).

40. Yu, J. H. *et al.* Synthesis of quantum-sized cubic ZnS nanorods by the oriented attachment mechanism. *Journal of the American Chemical Society* **127,** 5662–5670 (2005).

41. Jenny, H. Studies on the mechanism of ionic exchange in colloidal aluminum silicates. *The journal of physical chemistry* **36,** 2217–2258 (1932).

42. Rivest, J. B. & Jain, P. K. Cation exchange on the nanoscale: an emerging technique for new material synthesis, device fabrication, and chemical sensing. *Chemical Society Reviews* **42,** 89–96 (2013).

43. Son, D. H., Hughes, S. M., Yin, Y. & Alivisatos, A. P. Cation exchange reactions in ionic nanocrystals. *science* **306,** 1009–1012 (2004).

44. Casavola, M. *et al.* Anisotropic cation exchange in PbSe/CdSe core/shell nanocrystals of different geometry. *Chemistry of Materials* **24,** 294–302 (2012).

45. Luther, J. M., Zheng, H., Sadtler, B. & Alivisatos, A. P. Synthesis of PbS nanorods and other ionic nanocrystals of complex morphology by sequential cation exchange reactions. *Journal of the American Chemical Society* **131,** 16851–16857 (2009).

46. Sadtler, B. *et al.* Selective facet reactivity during cation exchange in cadmium sulfide nanorods. *Journal of the American Chemical Society* **131,** 5285–5293 (2009).

47. Pietryga, J. M. *et al.* Utilizing the lability of lead selenide to produce heterostructured nanocrystals with bright, stable infrared emission. *Journal of the American Chemical Society* **130,** 4879–4885 (2008).

48. Fan, Z., Lin, L.-C., Buijs, W., Vlugt, T. J. & Van Huis, M. A. Atomistic understanding of cation exchange in PbS nanocrystals using simulations with pseudoligands. *Nature communications* **7,** 1–8 (2016).

49. Campbell, F. C. *Fatigue* in *Elements of metallurgy and engineering alloys* 260 (ASM International, 2008).

50. Sliem, M. A., Chemseddine, A., Bloeck, U. & Fischer, R. A. PbSe nanocrystal shape development: oriented attachment at mild conditions and microwave assisted growth of nanocubes. *CrystEngComm* **13,** 483–488 (2011).

51. Hassinen, A. *et al.* Short-chain alcohols strip X-type ligands and quench the luminescence of PbSe and CdSe quantum dots, acetonitrile does not. *Journal of the American Chemical Society* **134,** 20705–20712 (2012).

52. Peters, J. L., van der Bok, J., Hofmann, J. P. & Vanmaekelbergh, D. Hybrid Oleate–Iodide Ligand Shell for Air-Stable PbSe Nanocrystals and Superstructures. *Chemistry of Materials* **31,** 5808–5815 (2019).

53. Kaneko, F. *et al.* Structure and crystallization behavior of the β phase of oleic acid. *The Journal of Physical Chemistry B* **101,** 1803–1809 (1997).

54. Suzuki, M., Ogaki, T. & Sato, K. Crystallization and transformation mechanisms of α, β-and γ-polymorphs of ultra-pure oleic acid. *Journal of the American Oil Chemists' Society* **62,** 1600–1604 (1985).

55. Rico, B. *Most efficient way to calculate radial profile* `https://stackoverflow.com/questions/21242011/most-efficient-way-to-calculate-radial-profile`. Accessed: 30-01-2020. 2014.

56. Hashemi, R. H., Bradley, W. G. & Lisanti, C. J. *k-Space: The Final Frontier!* in *MRI: The Basics* 181–185 (Wolters Kluwer Health, 2018).

Appendix

A Calculation of NC-NC bond angles in square superlattices

A Python script was used to determine the angles between the NCs in the square superlattices. The core part of this code, which makes use of the NumPy, SciPy and Matplotib packages, is displayed in the box below. Additional code for saving the obtained data and looping over multiple files at once has been omitted for clarity.

```
import numpy as np
import matplotlib.pyplot as plt
import scipy
from scipy.spatial import Delaunay
import scipy.ndimage as ndimage
import scipy.ndimage.filters as filters
from math import acos, degrees, sqrt
import imageio
import os

def load_image(image):
  im = imageio.imread(image)
  im = im[0:im.shape[1],:]

  return im

def fft(image):
  im = 255 - image

  FFT_im = np.fft.fft2(image)
  FFT_im = np.fft.fftshift(FFT_im)
  FFT_im = np.abs(FFT_im)

  center = [FFT_im.shape[0]/2, FFT_im.shape[1]/2]

  fig, ax = plt.subplots(1,2)
  ax[0].imshow(image, cmap = 'gray')
  ax[1].imshow(np.log(FFT_im), cmap = 'gray')
  ax[1].set_xlim(center[0]-300,center[0]+300)
  ax[1].set_ylim(center[1]+300,center[1]-300)
  plt.show()

```

```
33    return FFT_im
34
35  def label_FFT(FFT_im):
36    thresh = 16
37
38    FFT_im_filtered = ndimage.gaussian_filter(FFT_im, sigma=2)
39    FFT_im_thresh = np.where(np.log(FFT_im_filtered) > thresh, 1, 0)
40
41    labeled, nr_obj = ndimage.label(FFT_im_thresh)
42    coords = np.array(ndimage.center_of_mass(FFT_im_thresh, labeled, range(1, nr_obj
        +1)))
43
44    center = [FFT_im.shape[0]/2, FFT_im.shape[1]/2]
45
46    fig, ax = plt.subplots()
47    plt.imshow(np.log(FFT_im),cmap='gray')
48    plt.scatter(coords[:,1],coords[:,0])
49    ax.set_xlim(center[0]-300,center[0]+300)
50    ax.set_ylim(center[1]+300,center[1]-300)
51    plt.show()
52    return coords
53
54  def get_angle(data, FFT_im):
55    tri = Delaunay(data)
56
57    center = [FFT_im.shape[0]/2, FFT_im.shape[1]/2]
58
59    fig, ax = plt.subplots()
60    plt.imshow(np.log(FFT_im), cmap = 'gray')
61    plt.triplot(data[:,1],data[:,0],tri.simplices)
62    plt.scatter(data[:,1],data[:,0])
63    ax.set_xlim(center[0]-300,center[0]+300)
64    ax.set_ylim(center[1]+300,center[1]-300)
65    plt.show()
66
67    angle_list = []
68    for i in data[tri.simplices]:
69      center_index = (np.argwhere(np.all((i-center)==0, axis=1))).item()
70      j = i[center_index]
71      k = i[center_index-1]
72      l = i[center_index-2]
73
74      d_jk = sqrt((j[0]-k[0])**2+(j[1]-k[1])**2)
75      d_jl = sqrt((j[0]-l[0])**2+(j[1]-l[1])**2)
76      d_kl = sqrt((k[0]-l[0])**2+(k[1]-l[1])**2)
77
```

```
78      angle = round(degrees(acos((d_jk**2+d_jl**2-d_kl**2)/(2*d_jk*d_jl))),1)
79
80      angle_list.append(angle)
81
82    print('The measured angles in degrees are:', angle_list)
83
84    return angle_list
85
86 file_name =
87 im = load_image(file_name)
88 FFT = fft(im)
89 labels = label_FFT(FFT)
90 angles = get_angle(labels, FFT)
```

In lines 1-9 the different packages that will be used in the code are imported. Next, the "load_image" function is defined in lines 11-15. It takes the name of the image file as its argument and subsequently imports and returns the image as a NumPy array for further analysis. For the code outlined above, it is essential that the images that are to be imported are saved in the same folder as the code. An example image is provided in Figure A.1a.

In lines 17-33 the "fft" function is defined. It takes a NumPy array, the imported image, as its argument. In line 18 the grayscale image values are inverted so that the dark NCs in the bright field TEM images become light and the originally light background becomes dark. In line 20 the Fourier transform of the image is taken, after which the zero-frequency component of the FFT image is shifted to the center of the image in line 21. Since only the positions of the extrema in the FFT image are of interest for determining the angles in the superlattice in the original image, the absolute of the FFT image is taken in line 22. This rids the FFT image of negative and complex values to make further processing of the FFT image easier. After the FFT has been taken, the indices of the center of the FFT are determined in line 24. In lines 26-31 the original image as well as the FFT image are shown side by side for inspection by the user. Here, the natural logarithm is taken of the grayscale values of the FFT image, which is necesarry for plotting of the FFT image. In addition, the FFT image is cropped and only the part of the FFT image 300 pixels in the positive and negative x and y direction from the center is shown. For all images examined in this work, this area was the only region of interest. Cropping the image here therefore made inspection of the FFT easier. Finally, the FFT image is returned in line 33. The FFT of the example image from Figure A.1a determined by this code is given in Figure A.1b.

The "label_FFT" function, which takes the Fourier transformed image as its argument, is defined next in lines 35-52. In line 36 a threshold value is defined which can be changed by hand if required. Subsequently, the FFT image is filtered with a Gaussian filter with $\sigma = 2$ pixels and then thresholded in lines 38 and 39, respectively. For the thresholding of the image, the value defined in line 36 is used as the threshold value. In line 41 the different separate areas in the thresholded image are labeled using the

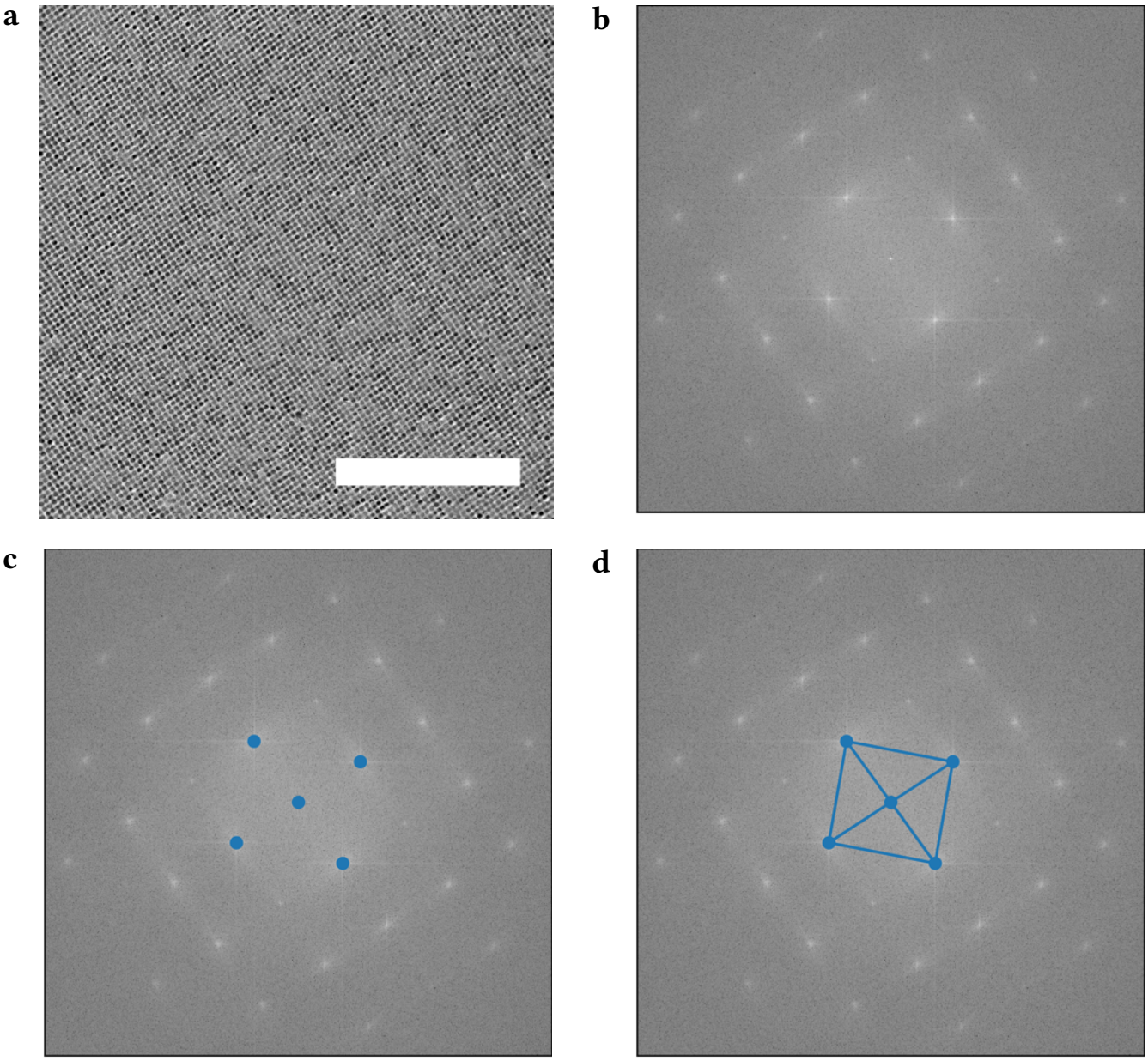

Figure A.1: Example of a TEM image processed with the Python script. **(a)** An example TEM image of a square PbSe superlattice. This TEM image, without the scale bar, is loaded by the "load_image" function in lines 11-15. Scale bar 200 nm. **(b)** FFT taken of the image in **(a)** using the "fft" function in lines 17-33 in the Python script. **(c)** FFT image from **(c)** with the maxima labeled by the "label_FFT" function in lines 35-52. **(d)** The same labeled FFT image as in **(c)** after Delaunay triangulation by the "get_angle" function in lines 54-84. The angles between the center and the other two points of each triangle is calculated by the Python script using the law of cosines.

label function of the SciPy package. In line 42 the center of mass of each labeled area is determined, as shown in Figure A.1c. In lines 44-51 the resulting centers of mass are plotted on the Fourier transformed image for inspection by the user. In line 52 the coordinates of the centers of mass are returned.

The "get_angle" function is defined in lines 54-84, taking the coordinates of the centers of mass and the Fourier transformed image as its arguments. Delaunay triangulation is performed with the centers of mass and the center of the Fourier transformed image in line 55. Since the center is always included in the smallest possible triangles in the FFT image, Delaunay triangulation results in triangles made with the center point and two adjacent extrema in the FFT image, as shown in Figure A.1d. In lines 59-65, the triangulated data is plotted as an overlay on the FFT image. In lines 67-80 the angles of the extrema in the FFT image are determined using a for-loop. The for-loop loops over all values in the list of triangulated coordinates. In line 69 the index of the coordinate corresponding to the center of the FFT image is determined. In line 70 this coordinate is assigned to the variable j. The other coordinates are asigned to the variables k and l in lines 71 and 72. The distances between the points j, k and l are determined using the Pythagorean theorem in lines 74-76. Subsequently, the angle between the center and the two extrema is determined in line 78 using the law of cosines, which states that in any triangle an angle γ can be expressed as:

$$\gamma = \arccos(\frac{a^2 + b^2 - c^2}{2ab}) \tag{5.1}$$

where a and b are the length of the sides containing the angle and where c is the length of the side opposite of the angle. An example triangle is given in Figure A.2. After the angle has been determined it is added to a list. After the loop has finished, the list containing all of the calulated angles is printed in line 82 and then returned in line 84. In the case of the example image in Figure A.1, angles of 87°/93° are measured.

In lines 86-90 the different functions outlined above are called in sequence.

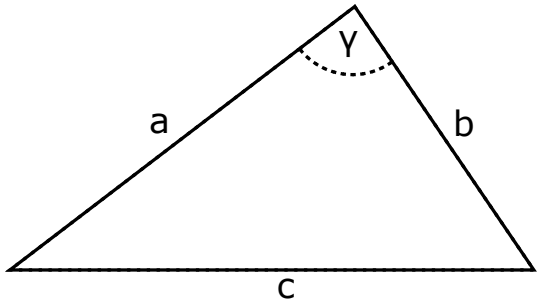

Figure A.2: An example triangle with sides a, b and c and with angle γ.

A.1 Calculation of the relative orientation of different domains

The Python code presented above was used to determine the relative orientation of the different domains in Figure 4.2b. The same TEM image is displayed here again in Figure A.3a. First, the Fourier transform was taken of the region of interest, marked with a red square. In this region of interest, $\sim$1000 and $\sim$300 NCs are present in the bottom left and top right square lattice domains, respectively. A zoomed in image of the FFT is shown in Figure A.3b. A square lattice is expected to show up in the FFT as four extrema at an angle of 90° with respect to eachother. Since there are two different square superlattice domains in the TEM image, eight intense extrema can be observed in the FFT image. These eight extrema can be grouped in two sets of four that are at an angle of approximately 90° with respect to eachother. Therefore these extrema correspond to the two different superlattice domains in the original TEM image. The angles between these two groups of four extrema then correspond to the angles between the different domains in the TEM image. To determine these angles, the FFT image is processed using the Python script outlined above. A Gaussian filter is applied and unwanted frequencies are filtered out, after which the eight extrema attributed to the square lattice domains in the TEM image are determined. The positions of the eight extrema that were found by the script are shown in Figure A.3c. After Delaunay triangulation of the eight extrema with the center, the angles between the extrema were determined. One of these triangulated sets of extrema with the center is shown in Figure A.3d. This angle was calculated to be 36°. Analysis of the other angles resulted in a rotational offset between the two superlattice domains of 36°-39°. The range in the offset is most likely due to imperfect square ordering of NCs in the superlattice domains, resulting in a deviation in the bond angles of the expected 90°.

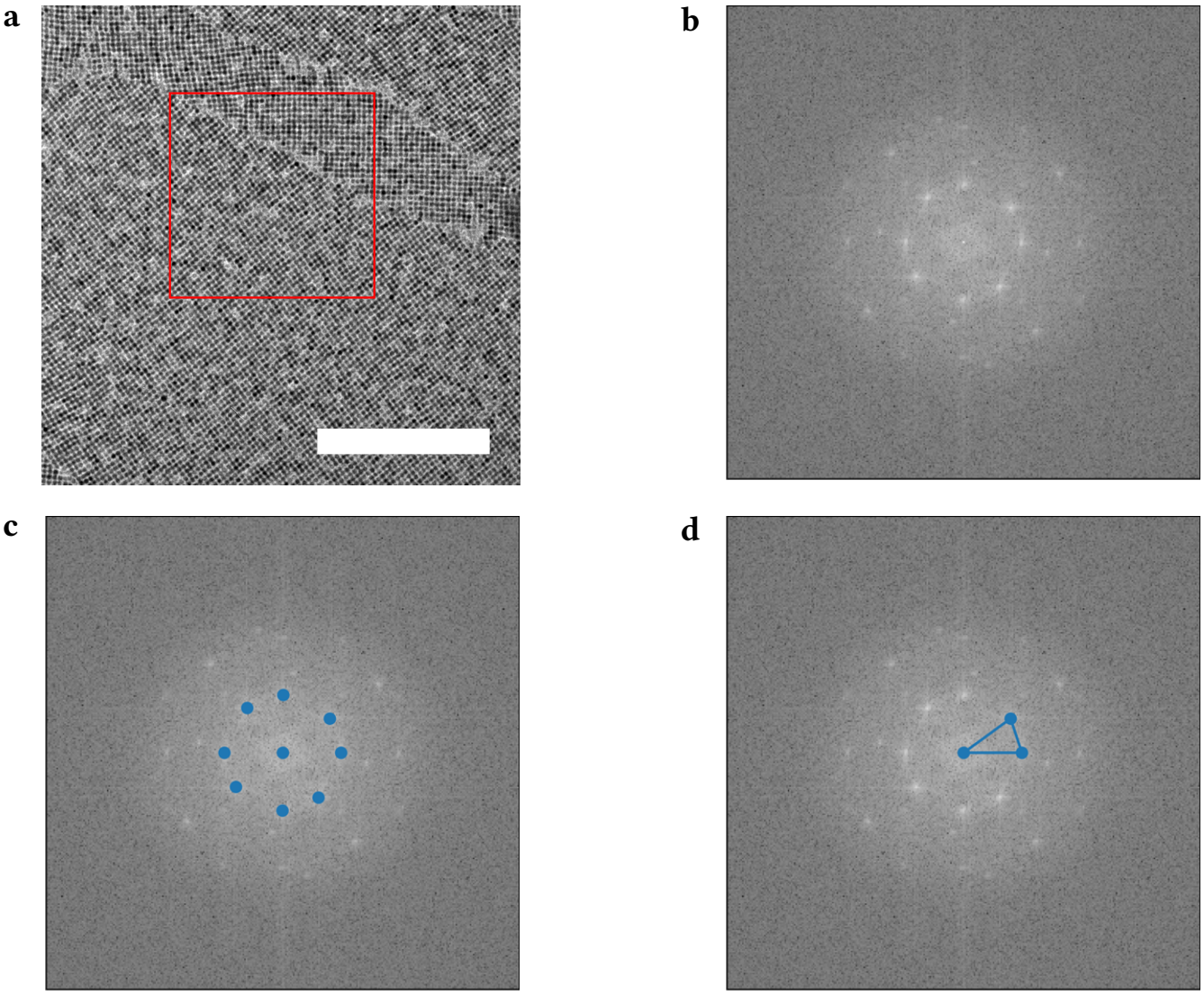

Figure A.3: FFT analysis of the angles in the square superlattices from Figure 4.2b. **(a)** The original TEM image showing different domains of square PbSe superlattice. The rotational angle of the grain boundary in the red square is analysed. Scale bar 200 nm. **(b)** The Fourier transform of the TEM image. Eight intense extrema can be observed, which correspond to the two square lattice domains. **(c)** The positions of the eight extrema attributed to the two square superlattice domains in the FFT image as well as the center of the FFT image are shown as blue dots. **(d)** One of the triangulated sets of extrema with the center. The angle of the center with the two extrema is determined by the Python script.

A.2 Deviating bond angles between NCs in a square superlattice

In Figure A.4 a superlattice is shown that was prepared at the same time as the lattices shown in Figure 4.2. The bond-angles in the superlattices in Figure 4.2 were between 86°/94° - 87°/93°. However, the average bond-angle in the lattice in Figure A.4 was determined to be 89°/91°. The bond-angles in all other TEM image of the as-formed superlattices prepared at this time were between the 86°/94° and 89°/91° determined in this section and in Section 4.1.2.

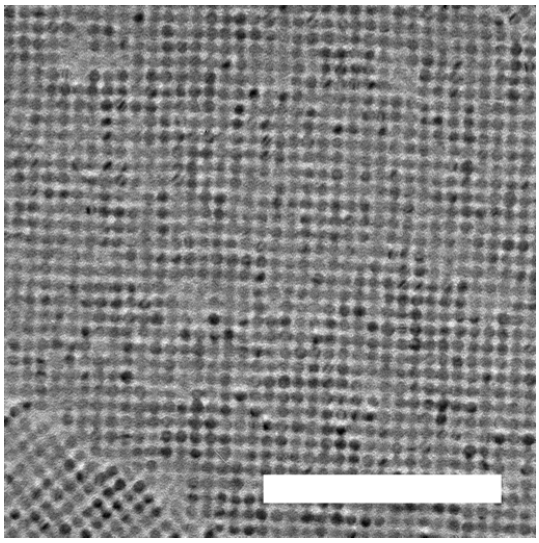

Figure A.4: TEM image of an as-formed square PbSe superlattice. This superlattice was prepared at the same time as those presented in Figure 4.2. For this superlattice, a deviating average bond angle of 89°/91° was determined by the Python script outlined in this section.

B Calculation of center-to-center distances of NCs in square superlattices

A Python script was used to determine the center-to-center distances between the NCs in the square superlattices. The core part of this code, which makes use of the NumPy, Matplotib, imageio, SciPy, os, eagletecnai and sistecnai packages, is displayed in the box below. Additional code for saving the obtained data and looping over multiple files at once has been omitted for clarity.

```
import numpy as np
import matplotlib.pyplot as plt
import imageio
from scipy.signal import find_peaks
from scipy import ndimage
import os
import eagletecnai, sistecnai

def get_scale():

  eagle_data = eagletecnai.Eagle_Tecnai_Data()
  sis_data = sistecnai.SIS_Tecnai_Data()

  folder = os.getcwd()
  files = os.listdir(folder)

  dpnm = {}
  for f in files:

    if os.fsdecode(f).endswith(('.tif', '.tiff')):
      eagle_data.open(os.path.join(folder, f))
      if 'dpi' in eagle_data.metadata:

        if 'real-XResolution' in eagle_data.metadata:
          res = eagle_data.metadata['real-XResolution'][0]

          dpnm[f] = 1e-9 * res

        else:
          dpnm[f] = 1e-7 * eagle_data.metadata['dpi'][0] / 2.54

    else:
      sis_data.open(os.path.join(folder, f))
      if 'px size' in sis_data.metadata:

        dpnm[f] = 1e-9 / sis_data.metadata['px size'][0]
```

```
37    return dpnm
38
39  def load_image(image):
40    im = imageio.imread(image)
41    im = im[0:im.shape[1],:]
42
43    return im
44
45  def fft(image):
46    im = 255 - image
47
48    FFT_im = np.fft.fft2(image)
49    FFT_im = np.fft.fftshift(FFT_im)
50    FFT_im = np.abs(FFT_im)
51
52    return FFT_im
53
54  def filter_image(image):
55    lowpass = ndimage.gaussian_filter(image, 3)
56
57    return lowpass
58
59  def radial_profile(image, scale):
60    y,x = np.indices((image.shape))
61    center = [image.shape[0]/2,image.shape[1]/2]
62    radius = np.sqrt((x-center[0])**2+(y-center[1])**2).astype(np.int32)
63    binned = np.bincount(radius.ravel(), image.ravel())
64    nr_per_bin = np.bincount(radius.ravel())
65    radial_profile = binned/nr_per_bin
66
67    peaks,_ = find_peaks(radial_profile[:int(radial_profile.shape[0]/6)])
68    peaks_nm = np.shape(image)[0]/(peaks*scale)
69    filtered_peaks = peaks[peaks_nm < 12]
70
71    max_cycles = filtered_peaks[np.argmax(radial_profile[filtered_peaks])]
72    max_nm = np.shape(image)[0]/(max_cycles*scale)
73
74    print('Highest peak radial distance from the center: ', max_cycles, 'cycles')
75    print('Highest peak radial distance from the center: ', max_nm, 'nm')
76
77    return radial_profile, max_nm
78
79  def plot_data(rad_prof, fft_image):
80    fig,(ax1,ax2) = plt.subplots(1,2)
81    ax1.plot(rad_prof[:int(rad_prof.shape[0]/6),0],rad_prof[:int(rad_prof.shape[0]/6)
        ,1])
```

```
82    ax2.imshow(np.log(fft_image[int(fft_image.shape[0]/3):-int(fft_image.shape[0]/3),
        int(fft_image.shape[0]/3):-int(fft_image.shape[0]/3)]), cmap='gray')
83    plt.show()
84
85  scale = get_scale()
86  file_name =
87  im_scale = scale.get(file_name)
88  im = load_image(file_name)
89
90  if im_scale < 12:
91    filtered = filter_image(im)
92    FFT = fft(filtered)
93  else:
94    FFT = fft(im)
95
96  r_profile, c_to_c_distance = radial_profile(FFT, im_scale)
97  plot = plot_data(r_profile, FFT)
```

In lines 1-7 the different packages that are used in the script are imported. Next, the "get_scale" function is defined in lines 9-37. This function determines the scales of all the TIF files in the folder in which the script is saved in pixels per nm. The code in this function is adapted from a Python script written by Stephan Zevenhuizen. In lines 22-36 the function attempts to find several keywords in the metadata of the TIF file to determine the scale of the images. The scale found by the code is then converted into units of pixels per nanometer and are added to the "dpnm" dictionary defined in line 18. Finally, the "dpnm" dictionary is returned in line 37.

The "load_image" function is defined in lines 39-41. This function is identical to the "load_image" function that was used for the Python script in Appendix A. The function takes the name of a TEM image as its argument and loads the file with this name as a NumPy array in line 40. The TEM images used in this thesis included a scale bar at the bottom of the image. This scale bar is removed by slicing of the NumPy array in line 41 to prevent artefacts during later analysis of the image. Afterwards, the image is returned in line 43. An example TEM image is displayed in Figure B.1a.

The subsequent "fft" function is defined in lines 45-50. Again, this function is identical to a function used in the Python script in Appendix A. This function takes a NumPy array as its argument and inverts the grayscale values of the image in line 46. Subsequently, the FFT of the image is taken in line 48 and the zero-frequency component is shifted to the center of the image in line 49. Next, the absolute of the FFT image is taken in line 50, which rids the FFT image of negative and complex values to allow for easier analysis of the image. Finally, the Fourier transformed image is returned as a NumPy array in line 52. The FFT of the example image in Figure B.1a, determined by the "fft" function, is presented in Figure B.1b.

In lines 54-57 the "filter_image" function is defined, taking a NumPy array as its argument. In line

55 a Gaussian blur with a standard deviation of 3 is applied on this array to reduce noise in the image. Subsequently, the blurred image is returned in line 57.

The "radial_profile" function is defined in lines 59-77. The code in lines 60-65 are adapted from previously published code[55]. This function takes a NumPy array of a (Fourier transformed) image and a scale as its arguments. Two grids and the coordinates of the center of the image are defined in line 60 and 61, respectively. The distance of every pixel from the center is calculated in line 62, using the previously defined grids and the coordinates of the center. The obtained distances are then returned to "radius" and converted to integer numbers. Next, the radial distances in "radius" are binned and the greyscale values of all pixels in each bin are added together in line 63, after which the number of pixels in each bin is determined in line 64. For each bin, the sum of the greyscale values is divided by the number of pixels in line 65 to determine the average greyscale value. The resulting array is stored as "radial_profile". The positions of the peaks in the first one sixth of "radial_profile" are determined and stored in "peaks" in line 67. The later five sixth of the radial profile is not analysed, as here many peaks are typically present which are caused by noise. Next, the radial distances in "peaks", which are in units of pixels, are converted to nanometers in line 68. This is accomplished by dividing the length of the image in pixels by the radial distance in "peaks" and the scale of the real space image in pixels per nanometers[56]. For the TEM images analysed in this thesis, all distances larger than 12 nm were caused by noise. Therefore, all peaks with a distance larger than 12 nm are discarded in line 69 and the remaining peaks are stored in "filtered_peaks". The radial distance in "filtered_peaks" with the largest peak value is determined in line 71 and this peak position, which is in units of pixels, is converted to nanometers in line 72. In line 74 the radial distance with the highest average greyscale value in the FFT are printed in units of pixels. On the other hand, the corresponding real space distance in nanometers is printed in line 75. Finally, the radial profile and the distance of the highest average greyscale value in the FFT in nanometers are returned in line 77. The radial profile of the FFT shown in Figure B.1b determined by this function is presented in Figure B.1c.

In lines 79-83, the "plot_data" function is defined. This function takes a radial profile and the image of which the radial profile was taken as its arguments. A figure with two subplots is created in line 80. The first one sixth of the radial profile is plotted in one of the subplots in line 81, while the central two third of the image is shown in the second subplot in line 82. The resulting figure is shown by the function in line 83. Plotting the radial profile and the FFT image allows the user to varify the distance calculated by the "radial_profile" function.

Finally, the different functions are called in order in lines 85-97. The "filter_image" function is only called when analysing low magnification TEM images to reduce noise and make analysis by the "radial_profile" function easier.

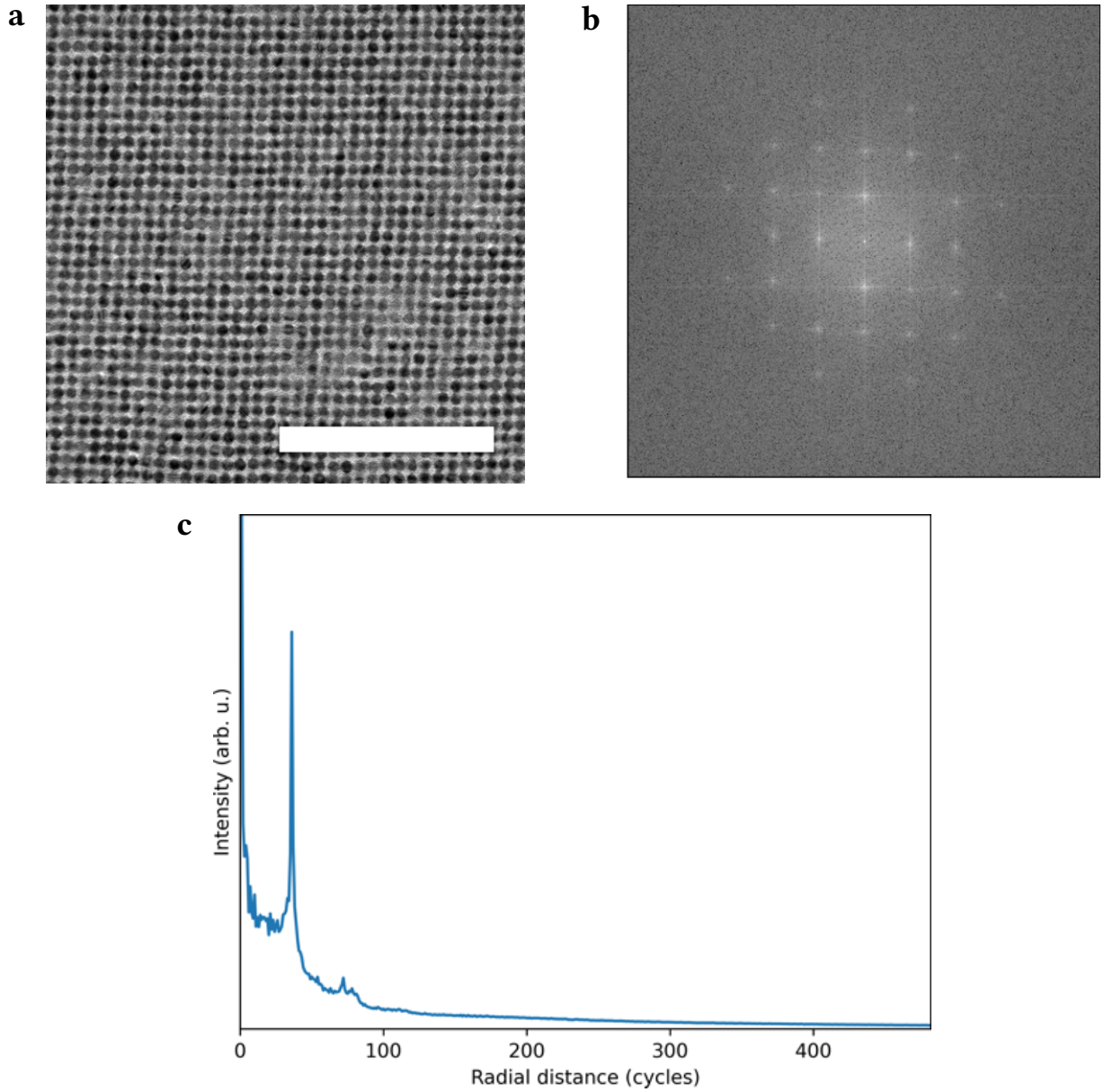

Figure B.1: Example FFT analysis of the center-to-center distance in a square superlattice. **(a)** The TEM image from Figure 4.2c, which is taken as the example TEM image. Scale bar 100 nm. **(b)** The FFT of the image, as determined by the "fft" function defined in lines 45-52. **(c)** The radial profile of the image, calculated by the "radial_profile" function in lines 59-77.

C Additional annealing experiments on square PbSe superlattices

C.1 Annealing of square PbSe superlattices on ethylene glycol

A superlattice annealed on ethylene glycol is compared to a superlattice annealed on a TEM grid in Figure C.1. Even though annealing on ethylene glycol was performed at a temperature of 38 °C for only 10 minutes, significant amounts of molten structures were observed in this sample, as shown in Figure C.1a. Contrary to the results obtained for superlattices annealed on ethylene glycol, molten structures were absent in the superlattice annealed on a TEM grid at a temperature of 100 °C for 1 hour. However, some vacancies can be observed in these lattices, as can be seen in Figure C.1b. In spite of these vacancies, the superlattices annealed on the TEM grid at a significantly higher temperature for a longer duration retained more long range order compared to the superlattices annealed on ethylene glycol.

This discrepancy can be understood with the proposed mechanism of oriented attachment by ligand desorption from the NCs in the ethylene glycol[5, 17]. It would seem that the increase in temperature of the ethylene glycol during oriented attachment increased the rate of ligand desorption significantly. As a result, the molten structures formed that are visible in the TEM image. Hence, based on the results presented here, it was concluded that annealing of superlattices on TEM grids was preferable over annealing on ethylene glycol for obtaining superlattices with long range order. Nevertheless, much higher temperatures of up to 80 °C have been reported in literature for annealing of square PbSe superlattices on ethylene glycol[4]. Therefore, it is likely that the results of annealing on ethylene glycol strongly depend on the NC batch.

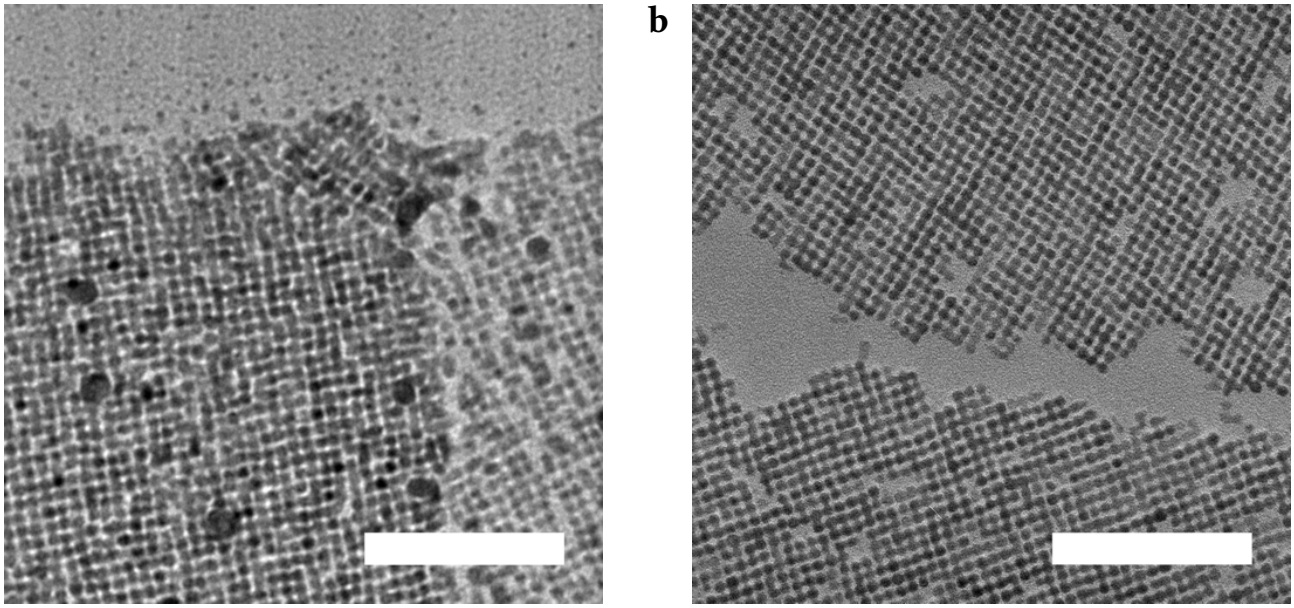

Figure C.1: Comparison of a square PbSe superlattice annealed on ethylene glycol and a lattice annealed on a TEM grid. **(a)** TEM image of a square PbSe superlattice annealed on ethylene glycol at 38 °C for 10 minutes. Molten structures can be observed in the lattice, while unattached material is visible at the top of the image.**(b)** TEM image of a square PbSe superlattice annealed on a TEM grid at 100 °C for 1 hour. Some vacancies can be observed, but no molten structures are present in this annealed lattice. Scale bars 100 nm.

C.2 Annealing at 150 °C for 1 hour

In the work of Walravens *et al.*, annealing at 150 °C led to only a modest increase in the neck thickness[35]. Contrary to these results, the lattices obtained after annealing at 150 °C for 1 hour in this work resulted in completely molten structures, as evident from Figure C.2. Further experiments are required to elucidate the cause of the difference in the results presented here and those reported in literature. Possible causes of the discrepancy between the results presented here and those reported in literature are discussed in the main text.

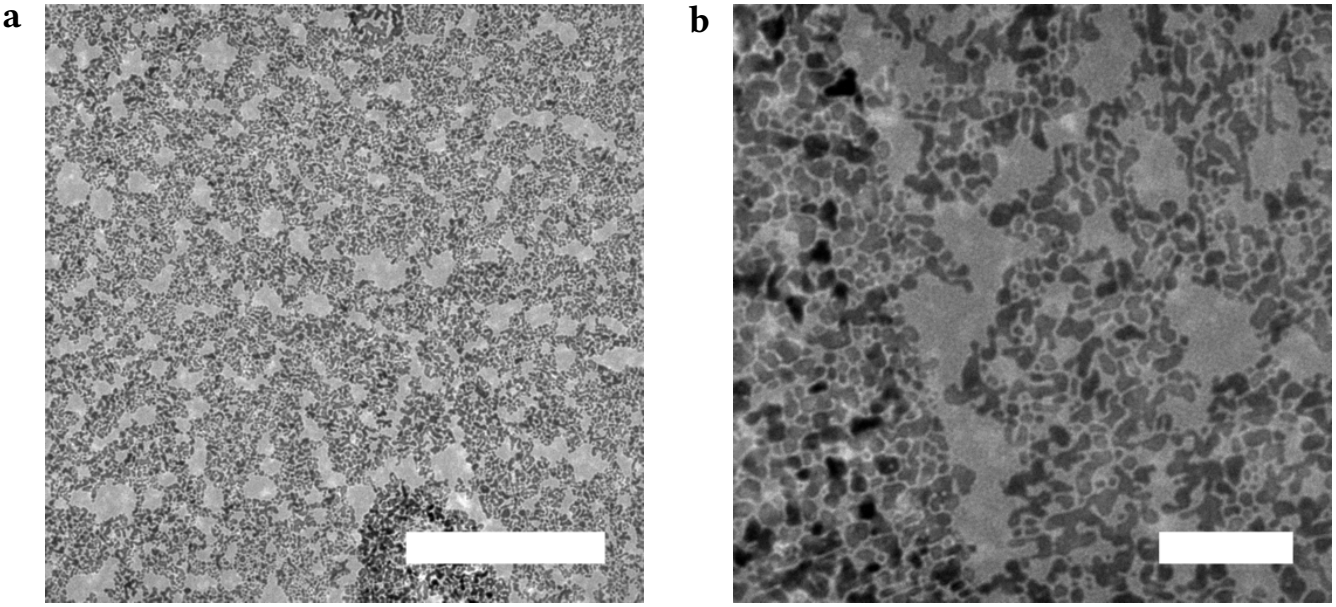

Figure C.2: TEM images of square PbSe superlattices annealed at 150 °C for 1 hour. **(a)** TEM image of the annealed lattice, revealing that no square lattice domains remain. Scale bar 500 nm. **(b)** A higher magnification TEM image of the annealed lattice. After annealing at 150 °C for 1 hour only molten structures remained. Scale bar 100 nm.

D Superlattices prepared at 15 °C for 3 hours

The results of the superlattice preparation at 15 °C for 180 minutes are presented here. No molten structures formed under these reaction conditions, as shown in Figure D.1a. However, the square ordering in this superlattice appears to be distorted, similar to the lattice prepared at 15 °C for 90 minutes. In a TEM image of this superlattice at a higher magnification, given in Figure D.1b, unattached NCs can also still be observed. In addition, a double layer can be seen in the left part of this image. This superlattice also showed areas where more square ordering is observed, as shown in Figure D.1c. In addition, an edge dislocation can be observed in the top part of the superlattice in Figure D.1c.

The average bond angles and the center-to-center distances of the superlattices shown in Figure D.1 were calculated using the Python scripts given in Appendix A and B. An average bond angle of 81°/99° and center-to-center distance of 6.7 nm were obtained for the ∼12500 NCs in the superlattice in Figure D.1a. For the ∼1000 NCs in the superlattice in Figure D.1b an average bond angle of 83°/97° and center-to-center distance of 6.1 nm were determined. An average bond angle of 89°/91° was determined for the ∼1000 NCs below the edge dislocation in the top of the image. The average center-to-center distance of all ∼1200 NCs visible in Figure D.1c was determined to be 6.4 nm.

The NCs in all other TEM image of this superlattice showed bond angles between 81°/99° and 89°/91° as well. Bond angles closer to 81°/99° were obtained in approximately 60% of the superlattice, while in the other ∼40% the average bond angle was closer to 90°. In addition, the center-to-center distances were between 6.4 and 6.7 nm for ∼90% of the superlattices. For the other ∼10%, average center-to-center distances between 6.1 and 6.4 nm were obtained, which is closer to the 6.3 - 6.4 nm for the lattices presented in Section 4.1.2. Hence, the superlattices prepared at 15 °C for 180 minutes were largely ordered in a phase between pseudo-hexagonal and square. Moreover, relatively large center-to-center distances were obtained for the majority of these lattices. These results indicate that the formation of the square superlattice was not completed after 180 minutes at 15 °C, similar to the lattices prepared at 15 °C for 90 minutes presented in Section 4.1.5. As outlined in Section 4.1.5, the bond angles and center-to-center distance in superlattices prepared at 15 °C for 4 hours are 88°/92° - 90° and 6.3 - 6.6 nm. From the change in the bond angles and center-to-center distances between the superlattices prepared at 15 °C for 3 and 4 hours it follows that the NCs were still mobile in the lattice after 3 hours. This provides further evidence that the formation of the square superlattice was not completed after 3 hours at 15 °C.

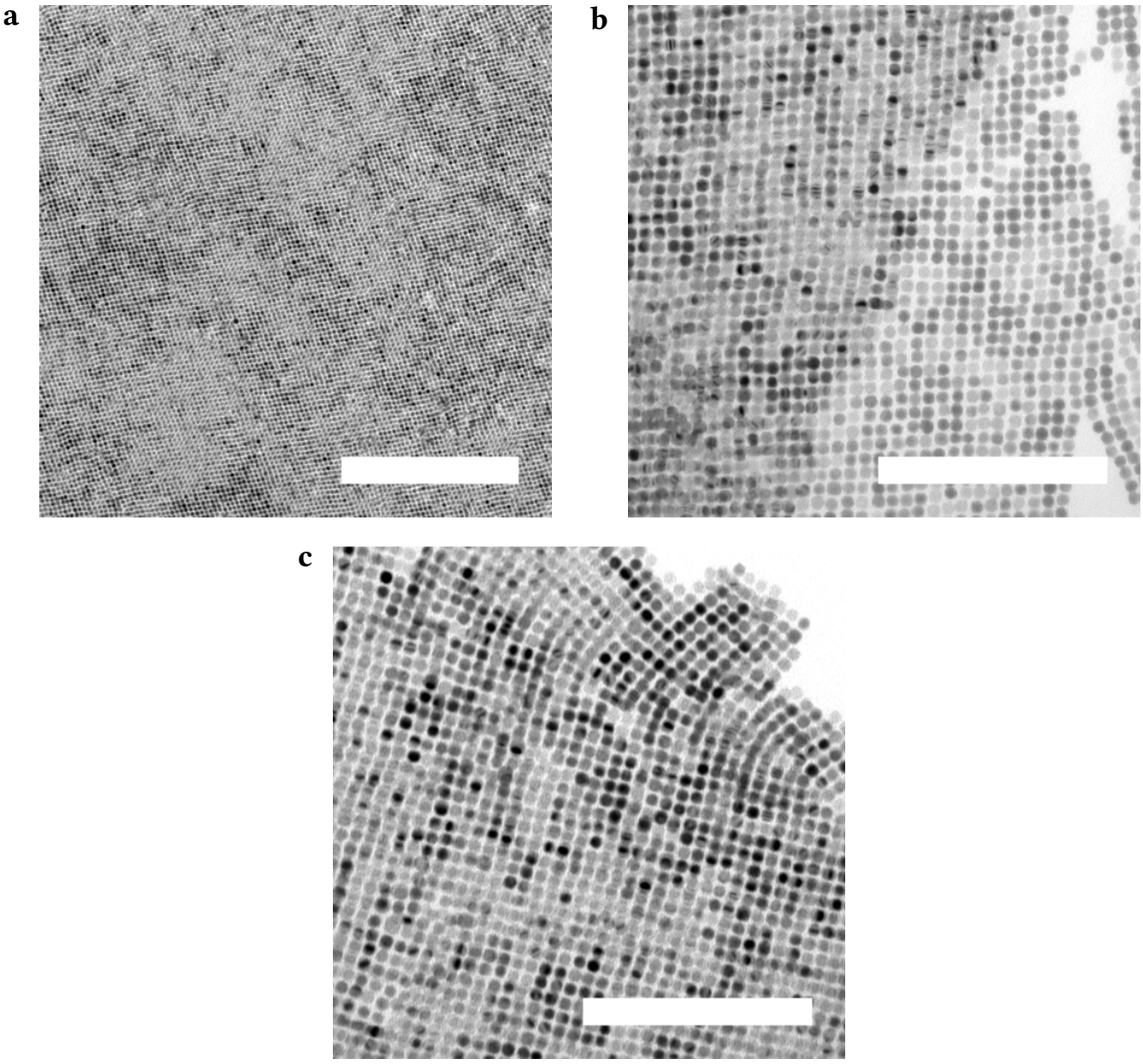

Figure D.1: TEM images of superlattices prepared at 15 °C for 180 minutes. **(a)** TEM image of the superlattice with the FFT in the top left corner, showing an absence of molten structures. The FFT shows bond angles of the NCs between those of a pseudo-hexagonal and square lattice. Scale bar 250 nm. **(b)** TEM image at a higher magnification of the same sample. Despite the longer reaction time, unattached NCs can be observed in this lattice as well. Scale bar 100 nm. **(c)** A different area of the same superlattice as in **(a)** and **(b)**, where square ordering can be observed in the superlattice area below the grain boundary. Scale bar 100 nm.

E High magnification TEM image of a superlattice cation exchanged at 130 °C for 2 hours

In Figure E.1 a high magnification TEM image is shown of the superlattice cation exchanged at 130 °C for 2 hours. Unfortunately the resolution in the TEM image is not high enough to infer the crystal structure of the exchanged lattice. This was also not possible in HAADF-STEM mode, as demonstrated in Figure 4.14 in Section 4.2.2. Hence, the crystal structure of the exchanged lattices should be determined on higher resolution electron microscopes which were not available in this work.

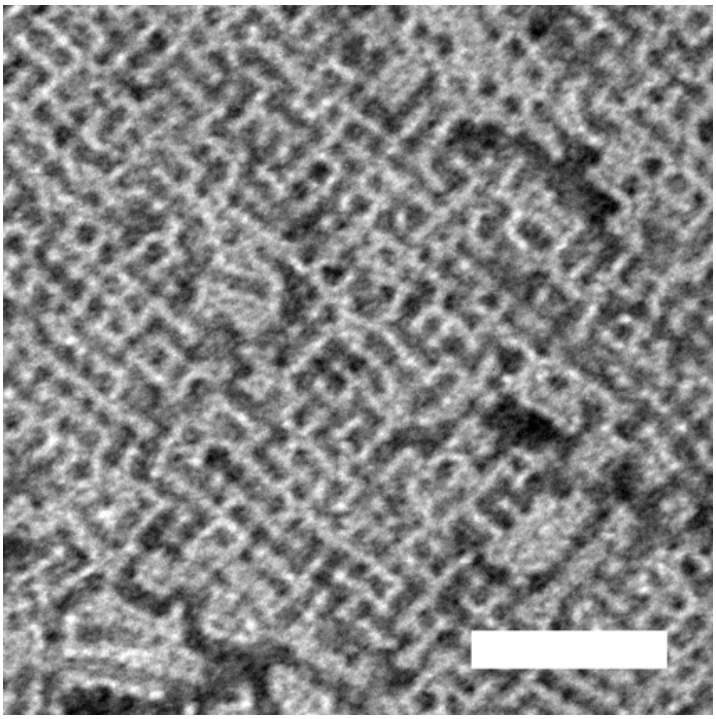

Figure E.1: High magnification TEM image of the superlattice cation exchanged at 130 °C for 2 hours. No initial annealing was performed on this superlattice before cation exchange. No columns of atoms are visible in the image.

F Elemental mapping of the partially exchange lattice

As explained in the main text, an attempt was made to make an elemental map of the lattice that was cation exchanged at 100 °C for 2 hours. The elemental map could shed light on where the Pb atoms remained in the lattice that showed partial exchange of approximately 76%. The area of the lattice of which the elemental map was made is shown in the TEM image in Figure F.1a. In Figure F.1b a TEM image is shown of the same area of the lattice after 7 minutes of elemental mapping. As can be seen in this image, the lattice melted during elemental mapping of this area of the lattice. The reduced thermal stability of the superlattice most likely also reduced the stability of the lattice during the elemental mapping. Nevertheless, the map that was obtained after approximately 7 minutes is shown in Figure F.1c. Unfortunately, not enough counts had been obtained after the lattice melted to determine accurately where the Pb atoms remained in the lattice.

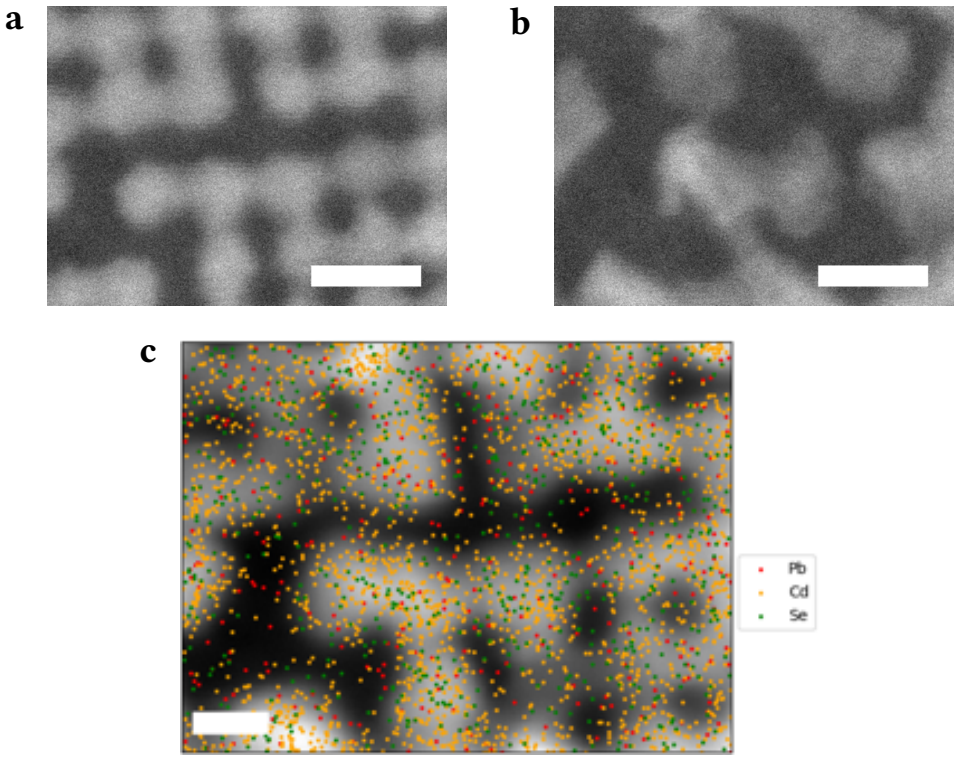

Figure F.1: TEM images and elemental map that were taken of the partially exchanged superlattice. **(a)** TEM image taken of the area of the lattice of which the elemental map was made. **(b)** TEM image taken of the same area of the lattice after elemental mapping was performed for approximately 7 minutes. The lattice has largely melted so that the mapping procedure had to be aborted early. **(c)** The elemental map that was obtained after measuring for 7 minutes.